Dynamics of Structures

Seismic Response of Liquid Storage Tanks

A Mode-Matching Approach Considering both Fluid-Structure and Soil-Structure Interaction

D. P. Kroon - 4273842
prof. dr. A. V. Metrikine
dr. ir. A. Tsouvalas
ir. T. Molenkamp
ir. M. Versluis

October 23, 2019

Witteveen + Bos

TU Delft

Preface

The thesis that lies before you is the final product of my master's degree in civil engineering with a specialization in structural mechanics and dynamics. It was completed as a cooperation between the Delft University of Technology and Witteveen+Bos.
My gratitude goes out to the members of my thesis committee for the time and effort they have spent on guiding me through the process. Specifically, I would like to express my thanks to Marco Versluis for keeping me motivated, helping me with my presentations and maintaining a constructive practical perspective. I would like to thank Timo Molenkamp for always wanting to get to the crux in our discussions, forcing me to get to the bottom of the material. Also thanks to Apostolos Tsouvalas and Andrei Metrikine for showing me new ways to consider mathematics and its physical meaning in dynamics.

I would also like to thank all my friends and family for their support over the years, of which a few I want to mention in particular. Carrie I would like to thank not just for correcting my English at any hour of the day, but more so for our conversations and for being a friend I can count on. I am also happy to have found a friend in Cas who has made all aspects of studying in Delft more fun and whose ability to see the positive side of things is inspiring.
I would like to express my appreciation for my brother Adriaan, who has motivated me to study civil engineering in the first place and continues to challenge me to consider all possibilites the world has to offer. Regarding my parents, Jos & Christa, I do not think I could have wished for better ones and I would like to thank them for everything they have done for me. Finally, I would like to thank Trudy for her patient listening and good advice, for offering the sometimes necessary distractions and for being there for me.

David Kroon
Rotterdam, October 2019

Abstract

Liquid storage tanks are used worldwide to contain liquids such as drinking water, fuel and chemicals. Loss of containment during a seismic event can add to an earthquake's destructiveness by posing a fire hazard, spilling toxic substances or reducing the supply of drinking water. It is therefore important that they remain operational at a pre-defined level of functionality during and after an earthquake event.
Two effects that are recognized to play a role in the seismic behavior of liquid storage tanks are fluid-structure interaction and soil-structure interaction. Numerical models have the ability to describe the dynamic behavior of each domain accurately, but they tend to be time consuming compared to many of the available simplified analytical models. While the latter can be useful for design purposes, they do not necessarily yield accurate solutions to the complex system at hand.
In this thesis, a semi-analytical model is put forward based on previous work by Canny (2018) and Molenkamp (2018) that combines both fluid-structure and soil-structure interaction with a dynamic substructuring approach. The model offers a computational efficiency and ease of use comparable to the aforementioned analytical models, but the only sacrifices to accuracy are the limitations imposed by the underlying assumptions and a number of discretizations. The tank, soil and fluid domains are treated separately. The tank is considered with Love's thin shell theory and the soil as a visco-elastic continuum. The fluid is assumed to be incompressible, irrotational and inviscid, allowing the application of linear potential theory. The solutions to the homogeneous equations of Love's shell theory, describing the behavior of the tank's bottom plate and wall segments, are found as eigenfunction expansions. By satisfying the boundary and interface conditions of the different tank parts, an eigenvalue problem is formulated that leads to the eigenfrequencies and mode shapes of the tank.
The fluid velocity potential is rewritten as the superposition of three fluid velocity potentials that each satisfy a set of conditions regarding the velocity continuity at the wall and at the plate, and the free surface condition at the fluid surface. The velocity potential in addition needs to satisfy Laplace's equation and solutions are found again as an expansion of eigenfunctions that represent the fluid's modes.
For the soil, Green's influence functions for uniform horizontal and vertical loads on a circular area at the soil surface have been used to assemble a dynamic soil stiffness matrix. The influence functions are again in the form of an eigenfunction expansion that is the solution to the homogeneous wave equation describing the soil's motions.
Through satisfaction of a set of conditions at the fluid-structure and soil-structure interfaces, respectively velocity and stress continuity, and displacement and stress continuity, a final set of equations is obtained. The only unknowns remaining in this set are the modal amplitudes that after solving can be used to linearly combine the mode shapes to give the full dynamic behavior of the tank-fluid system. Motions and stresses at the soil surface can be found with the dynamic soil stiffness matrix.
The dynamic soil-structure interaction is taken into account in the model by considering all wave fields present in the soil, namely the free-field (or incident), the scattered and the radiated wave field. Subsequent satisfaction of the soil-structure interface conditions ensures that soil-structure interaction is properly considered, and it yields a simple result in which the usually known free-field wave field can directly be applied in the excitation term of the plate's equations of motion.
Results are obtained in the frequency domain and can be transformed to the time domain with the inverse Fourier transform. Output can be obtained similar to the output of FE

models with stresses and displacements at each location of the tank domain. In the fluid domain, velocities can be found as well as related variables, such as the fluid pressures at the fluid-tank interfaces and the fluid elevation at the fluid surface (sloshing). Regarding the soil, stresses can be obtained at the soil-structure interface and displacements at the soil surface. Besides, the model can give more insight in the effects of SSI, compared to a tank-fluid system founded on a rigid soil.
Limitations of the model include the inability to model nonlinear effects, as a result of the linearity of the model, so that nonlinear failure mechanisms as buckling cannot be modeled, or nonlinear stress-strain relations. At the same time, nonlinear effects are not extensively covered in the other available analytical methods either.
With regard to engineering practice, roofs, ring stiffeners and anchors are commonplace, but have yet to be included in the model. Similarly, the capacity to model multiple soil layers would bring the model a step closer to reality. Besides more accurate modeling of the soil composition at a greater depth, it would admit a more realistic model of the soil directly underneath the tank, which is often improved in case of initially unsuitable grounds. Before the model can be applied in practice however, it needs to be validated, for example with a FE model or experimentally.
To increase the model's competitive advantage of computational efficiency, measures can be taken to improve it. The greatest improvements can be made in the assembly of the dynamic soil stiffness matrix by reducing the number of elements of the soil-structure interface. With the applied axisymmetric discretization, many of the matrix entries are the same, so that only a small number actually needs to be computed. However, a large number of very small elements is concentrated in the center of the soil-structure interface that does not add to the accuracy of the solution. Other discretizations could reduce computation time by reducing the number of elements and thereby the size of the dynamic soil stiffness matrix.

Contents

1 Introduction

Liquid storage tanks are essential structures in most societies for the storage of potable water, petroleum, fuel and chemicals, and for the treatment of sewage. Each of these liquids can be either of critical importance directly after an earthquake event or destructive by causing fires or chemical hazards. To prevent or mitigate health-related, economic and environmental losses, it is imperative to be able to design liquid storage tanks such that they satisfy safety requirements during seismic events.
Therefore, the seismic behavior of liquid storage tanks has been a subject of research for decades. While basic models were developed as early as the 1950's, the interaction effects that occur between both the soil and the tank as well as the fluid and the tank are complex. Ongoing research is aimed at developing ever more accurate or faster models through different approaches. In this thesis, a model is presented to predict the seismic response of cylindrical liquid storage tanks on shallow foundations, including both soil-structure and fluid-structure interaction with a semi-analytical approach. The purpose of this approach is to increase computational efficiency while maintaining the accuracy of more advanced models such as finite element models.
The remainder of the introduction is aimed at summarizing the various aspects of predicting the seismic response of liquid storage tanks, providing an overview of the current methodology, formulating the main research questions, and presenting the outline of this thesis.

1.1 Theoretical background

1.1.1 Earthquakes

Earthquakes are a shaking of the ground, caused by releases of energy in the earth's crust that are transported through seismic waves. The origins of the releases of energy can be natural, such as tectonic plate movements or volcanic eruptions, and human-made or induced, such as bomb explosions, filling of reservoirs or the collapse of underground cavities as a result of mining or drilling (Elnashai and Di Sarno (2015)).
The response of a structure to a release of energy is determined by the combination of two main aspects. The first is the excitation, or the fraction of the original release of energy that reaches the structure and the wave forms in which the energy is transported. While tectonic plate movements tend to have the highest energy release and generally lead to the most destructive earthquakes, induced earthquakes with a smaller energy release can also lead to significant damage in cases of a small focal depth or unfavourable soil conditions. The second aspect is the manner in which the structure responds to such excitations, or its structural dynamic behavior.
Concentrating on the aspect of the excitation, seismic waves come in different forms. A first distinction can be made between body waves that travel through the earth's interior layers and surface waves that travel across the earth's outer layers (Elnashai and Di Sarno (2015)). Body waves can then be subdivided between P-waves (longitudinal, pressure or primary waves) and S-waves (transverse, shear or secondary waves). P-waves displace particles parallel to the direction of propagation and cause the medium to expand and contract. S-waves displace particles perpendicular to the direction of propagation and thereby incite shear deformations in the medium, which can be subdivided into horizontal (SH) and vertical (SV) shear deformation.

In turn, surface waves, which originate from the constructional interference of body waves, can be subdivided into Rayleigh waves and Love waves (figure 1.1). Love waves behave like SH-waves with horizontal particle motion perpendicular to the wave direction. On the other hand, Rayleigh waves behave like coupled PSV-waves with vertical particle motion perpendicular to the wave direction, and horizontal particle motion parallel to the wave direction, resulting in a retrograde vertical elliptic motion (Novotny (1999)).

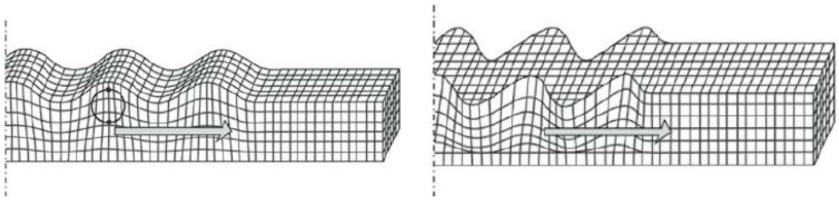

(a) (b)

Figure 1.1 – *Depiction of Rayleigh wave (a) and Love wave (b), adapated from Bolt (1999)*

Besides a distribution among different wave types, the released energy is distributed among waves with different frequencies. For example, at the source, the energy of a signal generated by an earthquake will be distributed more evenly accross all frequencies than the energy of a signal generated by a machine vibrating at a certain frequency.
What fraction of the released energy reaches the location of interest, and how that energy is distributed among the different wave types and frequencies, is dependent on the media through which the waves travel. Material properties determine the wave speeds and the amount of energy dissipation, while differences in material properties influence to what extent waves are reflected or transmitted and through which wave types (P- or S-waves) (see the book by Aki and Richards (2009) for more detail). In addition, the waves of each type will differ in wave length for each frequency of excitation and they are, in practice, dispersive.
In the end, the manner in which the seismic waves excite the structure also depends on the dynamic properties of the structure itself. The interaction between soil and structure is explained in more detail in the next subsection.

1.1.2 Soil-structure interaction

When ground surface motions are unhindered by the presence of structures, they are called free-field surface motions; the free-field waves thus make up the entire wave field at the ground surface. Whenever a structure is present, the ground motions influence the motions of the structure, while the structure affects the free-field motions. The effect soil and structure have on each other are collectively called soil-structure interaction (SSI) (Kramer (1996); Wolf (1985)).
First, if the shape of the structure does not match the shape of the free-field waves, the waves are reflected or scattered from the soil-structure interface. The total wave field then no longer consists of just the free-field waves, but is altered to include the scattered wave field. Since the motions of the structure can be imagined to average out the motions at the interface of the soil in the free-field situation, this effect is sometimes called base slab averaging (Stewart, Comartin, and Moehle (2004)). Second, if the structure is in motion, it transfers stresses to the supporting soil due to its inertia, thereby causing an additional

wavefield to the free-field waves. As a result of soil stiffness properties, the stresses generated are dependent on the frequencies of the structures' motions. The two interaction effects are called kinematic and dynamic soil-structure interaction respectively.
The relevance of SSI effects for a structure's design depend on the dynamic properties of both the structure and the soil. Interaction effects occur, when the behavior of the structure's domain influences the boundary of the soil domain and vice versa. In case the soil is extremely stiff, the structure's behavior will hardly influence the soil domain, so that interaction effects are negligble (Wolf (1985)). In less extreme cases, the presence of soil essentially introduces a flexible component into the system, which increases the fundamental periods of the system. Whether this is beneficial for the structure depends on the frequency content of the seismic input motion. Considering the response spectra in figure 1.2, including SSI can move the modeled system to a part of the spectrum with lower energy content to the right of the plateaus. On the other hand, a system with the relevant fundamental periods left of the plateaus, the incorporation of SSI can shift the period into the range of high seismic excitation.

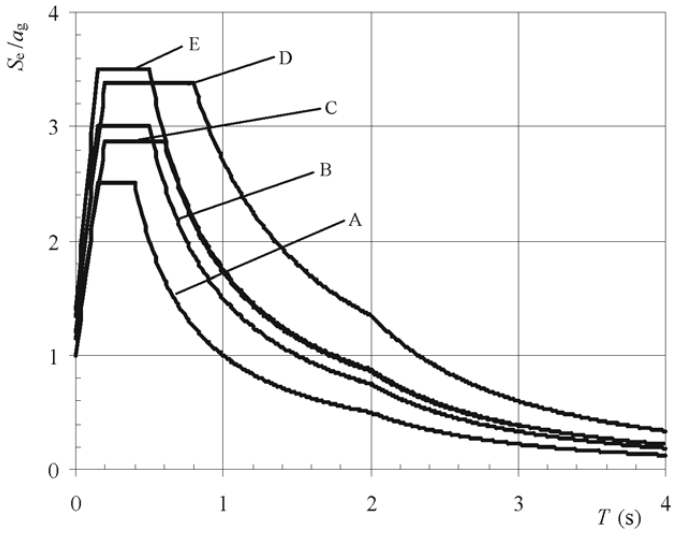

Figure 1.2 – *Elastic response spectra for single degree of freedom system for various soil types, from EN 1998-1 (2005)*

Another SSI effect is an increase of the system's damping, resulting from travelling waves that carry energy away from the structure. For soils resembling a half-space, this occurs in both horizontal and vertical direction, while waves can be reflected back to the structure in case of layered soils. In addition, soil layers act as wave guides, so that waves will not propagate at frequencies below the cut-off frequency, which depends on the soil layer's material and geometrical properties.
Finally, the wave-passage effect becomes relevant, when wave lengths approach the relevant dimensions of the structure (Elnashai and Di Sarno (2015)). The general relation between wave speed, wavelength and frequency is at its simplest

$$c = \frac{\omega}{k} \tag{1.1}$$

in which c is the wave speed, k the wavenumber, equal to the inverse of the wavelength, and

ω the angular frequency. The wave speed increases with stiffer soils, so at a given frequency the wavelength will increase. As the magnitude of wavelengths approaches relevant dimensions of the considered structure, which is most often the case for softer soils, the motions of the structure become more affected.

Recognition and modeling of SSI are far from new and the theoretical framework, still used in more modern methods today, was developed over the course of the 19^{th} and 20^{th} century, as described by Kausel (2010). Lamé and Clapeyron discussed, for example, the half-space problem early in the 19^{th} century and Thompson (or Lord Kelvin) and Stokes offered the first fundamental solutions for, respectively, static (1848) and dynamic forces (1849) in infinite elastic media. The first research into dynamic SSI was performed by Reissner, published in 1936, when he examined the dynamic behavior of circular disks (representing an actual structure) on an elastic half space. Kinematic SSI in its turn was first shown to exist by Housner (1957), who concluded, based on measurements, that the presence of a structure can filter out waves of certain lengths.
More recent methods to model SSI can be subdivided into the direct and indirect, or substructuring, approaches (Lu (2016); Tsouvalas (2017)). In the direct approach, both soil and structure are modeled in one model, whereas the substructuring approach treats soil and structure as separate systems that are subsequently coupled at their interface.
The direct approach requires fewer assumptions and offers the possibility to include nonlinearities, making it theoretically more accurate. It is generally applied using the finite element method (FEM), which poses certain challenges. For example, the software needs to be able to compute both soil and structure accurately, the boundaries of the soil domain need to properly handle the combination of radiating waves and seismic input motions, and the element size needs to be small enough to model the shortest waves, while the soil domain needs to be large enough to model the longest waves (Tsouvalas (2017)). Obtaining a stable model and useful results is time-consuming and therefore more expensive.
The substructuring approach is limited to linear models, but in general computationally much more efficient than the direct approach. Most often, the FEM is applied for the structure, and the soil is reduced to a dynamic stiffness matrix that can be directly applied in the structure's model. The soil domain, the cause of most issues in the direct approach, can be modeled more efficiently this way, for example by employing the boundary element method (BEM) or analytical methods.
Common numerical methods to model the soil domain are the FEM and more recently the BEM, in which the boundary of a domain of interest is discretized, instead of its interior. Considering the particular issue of needing small enough elements in a large enough soil domain, discretizing a surface instead of a volume can lead to significant time savings. In addition, the BEM automatically satisfies the radiation conditions, without the need for special boundary conditions (Menglin, Huaifeng, Xi, and Yongmei (2011)).
Analytical models of the dynamic soil stiffness comprise springs and dashpots in various configurations (even lumped for simplified structures). The simplest of these is the Winkler foundation, which consists of uncoupled, frequency independent, linear elastic, vertical springs. While computationally efficient, it disregards most of the complexity of soils. Efforts to improve the model are, for example, to add dashpots to the components, representing material and radiation damping, to couple the components and to add horizontal components to represent shear effects (Horvath (2002)). The increase in accuracy, however, comes at the cost of having to determine additional parameters that are usually site-specific.
More accurate analytical models to describe the dynamic response of soils have been pro-

vided by Kausel (1974, 2010) and Wolf (1985). They regarded the soil in their models as an elastodynamic continuum and have presented fundamental solutions for various types of loading and soil configurations, such as a half-space or soil strata on top of a half-space. These models can also be applied in modeling SSI, as shown by Molenkamp (2018), whose model is also applied in this thesis to represent the soil.

1.1.3 Fluid-structure interaction

When a fluid and a structure are in contact and the motions of the fluid affect the motions of the structure, while the motions of the structure in turn influence the motions of the fluid, fluid-structure interaction (FSI) occurs (Bhakade, Kumbhar, Mohite, and Kengar (2016)). FSI is not limited to civil structures, but is also an area of interest in marine technology for the design of propellors, in offshore engineering for determining wave impact, in aerospace engineering for the stability analysis of wings and in biomechanics for blood flow through vessels.
As in the case of SSI, and many other fields of mechanics and dynamics, the field of FSI was developed largely in the 19^{th} and 20^{th} century. Among the first to describe FSI effects was Bessel in 1828, who introduced the concept of hydrodynamic mass while investigating the motion of a pendulum in fluid (Jo (2008)). Stokes in 1843 was the first to quantify the added mass, considering the case of an infinite cylinder moving through an infinite fluid medium with a uniform acceleration. Further developments in the 20^{th} century were also driven by practical applications in a variety of fields. Stability analysis was needed for the advancement of aeronautics and the design of bridges, of which the Tacoma Narrows bridge is a notorious example. Also, the earthquake resistance of nuclear power plants and dams was researched (Westergaard in 1933). From the 1960s onward, the development of computers opened up many new possbilities in numerical analysis of FSI problems (Bungartz, Mehl, and Schäfer (2010)). While in specific cases, that admit simplifications of the fluid's behavior, analytical solutions are available, often the complexity of the physical processes involved requires numerical methods to be applied.
As in the case of SSI, the modeling of FSI can be subdivided in direct and substructuring approaches, which in literature are more often called monolithic and partitioned respectively (Bhakade et al. (2016); Bungartz et al. (2010); Zawawi et al. (2018)). In the monolithic approach both fluid and soil domains are modeled in one model and the equations regarding their behavior are solved at once. In the partitioned approach both domains are solved separately, with consideration of the behavior of the other domain through satisfaction of conditions at the interface between the two domains.
Since for the monolithic approach both domains are modeled in the same model and solved simultaneously, the discretization method for both domains is the same, generally the FEM. While the approach is relatively stable, because the coupling of the domains is done directly, the partitioned approach is much more popular in practice (Bhakade et al. (2016)). For structural analysis, the dominant discretization method is the FEM, whereas the preferred method of discretization for the fluid domain is highly dependent on the physical process that is being modeled (Bungartz et al. (2010)). Having to model both domains with the same discretization method can therefore be disadvantageous.
With the partitioned approach, the separate domains can be modeled with the most effective and appropriate methods. The use of specialized software, based on principles of computational fluid dynamics, permit modeling of fluid processes otherwise infeasible. At the same time, partitioning increases the difficulty of coupling the domains at the interface, especially

when nonlinear effects are considered. Solutions for both domains need to converge, while satisfying the behavior of the other domain at the interface. The interface conditions must also be satisfied at each time step, even though the time steps of both domains are not necessarily the same, as a result of computational optimization (Bungartz et al. (2010)).
Analytical models of FSI consider the fluid through the linear wave equation and assume the fluid to be inviscid and irrotational. Through the latter assumption, the fluid velocity may be expressed as the gradient of a scalar velocity potential, which simplifies much of the mathematics involved. Linearization does require that the amplitude of the motions of the fluid and structure are small compared to the wavelengths involved (Linton and McIver (2001)), and is therefore not suitable for all cases of FSI. An advantage of the analytical models, however, is that they are computationally efficient compared to the numerical methods described above.

1.1.4 Liquid storage tanks

Liquid storage tanks come in different configurations. Regarding their foundation, they can be elevated, based on the soil surface or embedded, and can be founded on piles in each of these cases. Most often tanks are made of steel, but concrete and composite tanks are not unusual either. Finally, common shapes are cylindrical (either horizontally or vertically), rectangular or spherical, depending on the tank's use case.
Concentrating on the vertically cylindrical tanks, common failure mechanisms include buckling of the walls, failure of the roofs and the roof-wall connections, and local rupture of the base plate (Maekawa (2012)). The buckling modes include bending buckling in the form of elephant foot buckling (elasto-plastic) or diamond buckling (elastic), and shear buckling (see figure 1.3).

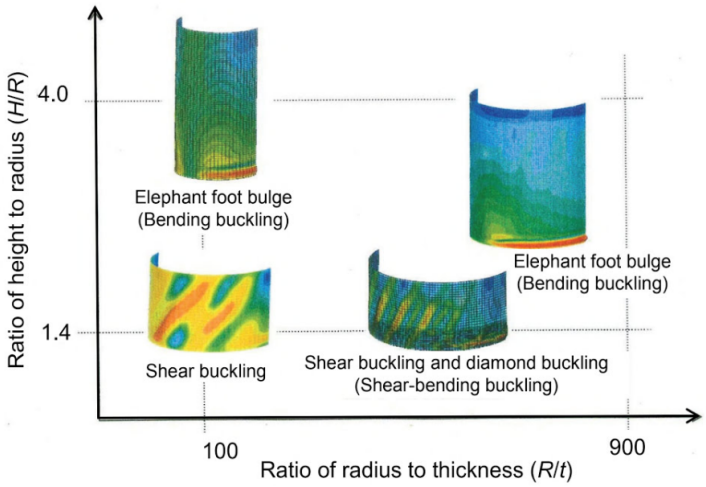

Figure 1.3 – *Visualizations of various buckling modes, from Maekawa (2012)*

Failure of tank roofs and roof-wall connections is associated with sloshing, when the fluid comes into contact with the roof. Finally, the base plate of a tank can fail, when the horizontal motion of the fluid causes an overturning moment so large that part of the bottom plate is lifted. In the case of anchored tanks, the overturning moment can result in failure of the anchors.

What exactly constitutes failure depends in addition on the safety requirements imposed on the design, which stem from the risks associated with a loss of containment and the required functionality during or after an earthquake event. For instance, the Eurocode defines an ultimate limit state, which is the state prior to structural collapse, and a damage limitation state. The latter corresponds to an 'integrity' requirement, satisfied if the tank remains leakproof and fully operational, or a 'minimum operating level', which allows limited damage to occur to a degree at which the system can still operate at a pre-defined level.
The application of FSI in the examination of cylindrical liquid storage tanks dates back to 1949, when Jacobsen found the dynamic fluid pressures that develop during an earthquake in a cylindrical tank containing fluid (Housner George W. (1957)). Housner later formulated the concept of the impulsive mass, the part of the fluid that moves synchronously with the walls, and the convective mass, the oscillating mass that represents the so-called sloshing part of the fluid (Housner (1963)). The simple model he presented is still at the base of design codes today (see figure 1.4).

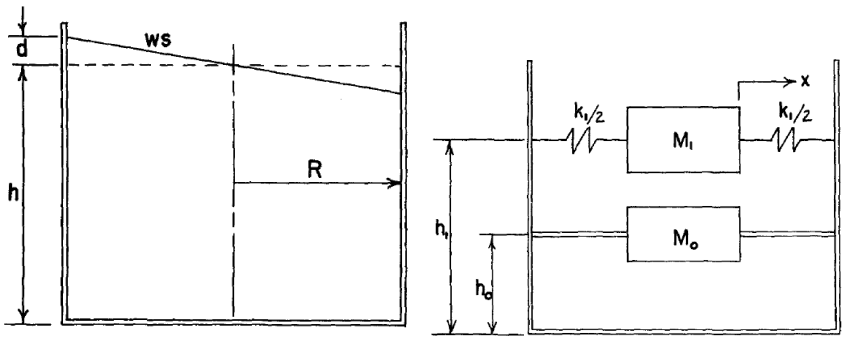

Figure 1.4 – *Housner's mechanical model (a) and lumped mass approximation (b) with M_0 as the impulsive mass and M_1 as the convective mass, from Housner (1963)*

However, the behavior of the liquid storage tanks proved more complex than these simple models suggested, as observed from the discrepancies between expected and measured behavior (Haroun (1980)). One such example is the original focus on just the asymmetrical vibrations resulting from horizontal excitations and neglect of the axisymmetrical response resulting from vertical excitation (Shahverdiani, Rhai, and Khoshnoudian (2008)). Also, the flexibility of the tank itself significantly affects the behavior of the fluid-structure system (Nicolici and Bilegan (2013)). Since then, research has been aimed at improving the predictive capacity of models and development of simple design methods. Both analytical and numerical paths of research have been pursued.
Edwards (1969) was the first to apply numerical methods to research this topic by employing the FEM and many others have followed, such as Haroun and Housner (1981), Veletsos (1984) and Tang (1986). In more recent years, improvements in numerical models are still being made, mostly in adding nonlinear effects (Phan and Paolacci (2018)).
At the same time, analytical methods were developed to solve the coupled fluid-structure problem. Relatively simplified models include for example the one by Veletsos, who included a flexible wall in the model of Housner. The more advanced models have been linear in nature and make use of shell theory for the tank. The fluid is generally modeled as inviscid, irrotational and incompressible, which allows linear potential theory to be applied. Many

of the studies, however, included either a flexible wall and rigid bottom plate or vice versa, thereby capturing only part of the physical processes (see Amabili, Païdoussis, and Lakis (1998) for a more extensive list). Bauer and Siekmann (1971) did include both a flexible wall and a flexible bottom plate, but these were not connected. Amabili et al. (1998) overcame this problem by coupling both parts through rotational springs. Still, in these models that consider FSI accurately, the soil domain is considered either as rigid, or simplified as a Winkler foundation, in some cases supplemented with viscous dampers. The latter is developed by Canny (2018); Tsouvalas, Canny, Versluis, Peng, and Metrikine (2018), whose fluid-tank model is incorporated in this thesis.
While analytical methods have been developed to accurately assess soil behavior as discussed above, these have not widely been applied in models for liquid storage tanks. Some have modeled the effect of SSI on a liquid-tank system, such as Tang and Veletsos (1990) who consider kinematic and dynamic SSI, or Haroun and Abdel-Hafiz (1986) and Larkin (2008), whose work seems to build on the work by Gazetas (1983) that includes frequency dependent springs, but is based on the motion of just a rigid plate. Even though they have shown that SSI influences the behavior of the liquid-tank system, these studies lump the soil behavior into greatly simplified parameters, such as a single stiffness and damping parameter. Malhotra (1997) divides the bottom plate into segments that individually treat the repsonse of the soil at each location, but he in turn simplifies the fluid as a lumped parameter.
Some efforts have been made to model liquid storage tanks with FSI and SSI effects using a nonlinear FEM (Chaithra, Krishnamoorthy, and Naurin Nafisa (2017); Gibson, Mistry, Go, and Lubkowski (2015)), claiming that accurate modeling of all domains, as opposed to lumping domains into simplified parameters, allows optimization of the tank design. This can lead to material savings or a safer tank design. Especially in extreme cases, such as very large tanks in areas prone to earthquakes, a more detailed assessment might be desired, than can be provided by simplified design rules.

1.2 Research questions

As can be concluded from the above, both SSI and FSI can play an important role in the seismic behavior of liquid storage tanks. Models that consider all domains in detail are finite element models that tend to be expensive in computation and calibration time. Analytical models on the other hand usually are computationally efficient, but model at most one of the two interaction effects accurately. Even though these studies can yield useful results depending on the case at hand, information is lost that may be valuable for a more safe and economic tank design.
In summary, an improvement over the current set of available tools for modeling liquid storage tanks including both SSI and FSI would be a model that can make predictions at the speed of an analytical model with the accuracy of a more advanced numerical model. In addition, a model that accurately incorporates both FSI and SSI could be used to contribute to the current body of knowledge with a more in-depth study of the effects of various soil parameters on the seismic response of liquid storage tanks. The main question addressed in this thesis is therefore:

To what extent can the seismic behavior of cylindrical liquid-storage tanks on shallow foundation be predicted with a semi-analytical dynamic substructuring technique considering both soil-structure and fluid-structure interaction?

To provide an answer to the main question, the following subquestions are answered:

How can dynamic soil-structure interaction be included in a semi-analytical tank-fluid model?

What is the influence of soil layer height, shear wave speed and tank aspect ratio on the seismic response of a liquid storage tank?

How can the amount of damping be determined of the tank-fluid system through soil-structure interaction?

The goal of the model can be specified as being able to generate results with an analytical model that are comparable to the output of a finite element model, e.g. stresses and displacements at any location in the tank, stresses at the soil-structure interface, soil surface displacements outside the soil-structure interface and the fluid pressures acting on the tank.

1.3 Layout of report

In the next section (section 2) of this report, the soil-fluid-structure model is presented. First, an overview is given of all included elements, the underlying assumptions and the limitations. This is followed by a mathematical formulation of the model, describing the motions of the substructures and the conditions at their boundaries and interfaces. The excitation of the system is also described, as well as the manner in which soil-structure interaction is properly considered.
In section 3, convergence of the model is verified and the model is applied to a realistic case study, showing the possibilites it offers.
In the subsequent section, section 4, the model is used to assess the impact of the height of the soil layer, of the soil type and of the tank's aspect ratio on the increase of the fundamental period of the tank. The model is also compared to a soil model consisting of uncoupled static springs and dashpots.
The final section, section 5, provides concluding remarks, a discussion of the model and recommendations for future improvements.

2 Methods

In this section, the proposed semi-analytical approach to model the soil-structure-fluid system is treated in more detail. Descriptions of the tank, fluid and soil domain are presented, followed by a more in-depth explanation of the method of solution and the underlying assumptions. Next, the differential equations governing the motions of each domain are given, as well as their solutions. The latter are applied in the conditions that need to be satisfied at the boundaries and interfaces of the domains to arrive at the final set of equations that needs to be solved.

2.1 Model description

To find the linear response of the structure-fluid-soil system, a semi-analytical dynamic substructuring approach is applied, specifically the mode-matching technique, or eigenfunction expansion technique. To that end, the system is divided into three substructures: the tank, the fluid and the soil (figure 2.1). The tank can be filled with fluid up to any level, and is located on top of the soil, so not embedded and without a pile foundation. Because of the circular symmetry of the system, a cylindrical coordinate system is adopted.

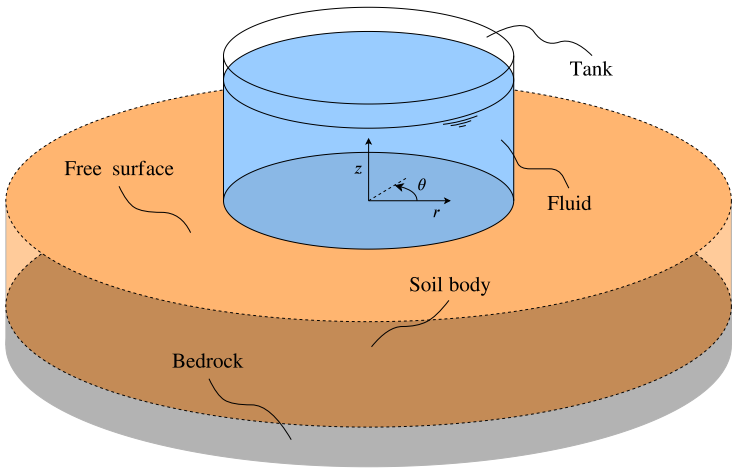

Figure 2.1 – *Liquid storage tank, partially filled with fluid, located on top of a horizontally unbounded soil layer. The global coordinate system has its origin at the center of the mid-surface of the tank's bottom plate.*

2.1.1 Solution method

First, eigenvalue problems are solved for the tank and fluid separately. By satisfying their respective boundary and interface conditions, the vibration modes or shapes of both domains can be found. Combining these modes in an infinite series allows them to form any arbitrary shape by assigning the proper amplitudes to each mode. While the mode shapes are constant system properties, the amplitudes vary with the load case.
To find the motions of the coupled fluid-tank system, the mode shapes of both domains

must be assembled in such linear combinations that their final motions respect the behavior of the other domain at the interface. To that end, interface conditions are formulated that must be satisfied in addition to the equations governing the motions of both domains.
The soil is substructured in a slightly different manner. As with the other domains, an eigenvalue problem is solved for the soil layer, yielding displacement shapes that can be combined linearly to produce any vibration shape. Contrary to the other two domains, the response of the soil is found for unit surface loads in horizontal and vertical directions, uniformly distributed over a circular area with an arbitrary radius. The functions describing the relation between the load and the response are called Green's influence functions (Wolf (1985)). By discretizing the soil-structure interface into circles with sufficiently small radii (infinitesimally small to obtain an exact solution) loads and displacement fields of arbitrary shape can be represented. Instead of matching the shapes of soil and structure at their interface, as was the case for the fluid-structure interface, the stresses from the soil acting on the tank bottom are related to the tank's displacement field in the tank's equations of motion. The advantage of this approach is that incorporating more soil layers only changes the Green's influence functions.
Finally, to find the modal amplitudes and thereby the motions of the tank and fluid, the earthquake excitation is introduced into the system. As the seismic waves excite the system through the soil and its interface with the structure, a displacement field is prescribed in the soil stress term of the equations of motion of the tank's bottom plate. Now a system of algebraic equations equal in number to the unknown modal amplitudes can be solved. While that number should, in theory, be infinity to obtain an exact solution, computational limitations require the truncation of this infinite series of modes, so that the found solution is an approximation of the actual solution. The final system of equations is simplified by using the orthogonality properties of the vibration modes.
To solve the soil-structure-fluid system in the frequency domain, the Fourier transform pair is used to transform equations from the time domain to the frequency domain, or vice versa. The Fourier transform can also be applied to transform equations from a spatial domain to its related wavenumber domain:

$$\begin{aligned} \mathcal{F}(\omega) &= \int_{-\infty}^{\infty} f(t) e^{-i\omega t} \mathrm{d}t \qquad \mathcal{F}(k) = \int_{-\infty}^{\infty} f(x) e^{-ikx} \mathrm{d}x \\ f(t) &= \frac{1}{2\pi} \int_{-\infty}^{\infty} \mathcal{F}(\omega) e^{i\omega t} \mathrm{d}\omega \quad f(x) = \frac{1}{2\pi} \int_{-\infty}^{\infty} \mathcal{F}(k) e^{ikx} \mathrm{d}k \end{aligned} \tag{2.1}$$

Because solutions in the frequency domain take account of frequency content, but not time, they are usually applied to find the steady-state response of a system. However, transient responses can in principle still be handled by superposition of harmonics through the inverse Fourier transform. In the case of earthquakes, the excitation signal is of finite duration and variable frequency content over time. Very short earthquake signals might not have the time to excite all modes in full. To analyze the response of a tank to an actual earthquake, use can be made, for example, of the short-time Fourier transform.
One of the advantages of the substructuring approach is that variations of the substructures do not require recalculation of the entire system, but just of the relevant substructure. This allows, for example, relatively quick sensitivity analyses. An advantage of a semi-analytical approach is that within the assumptions of the linear regime, the model can achieve very high accuracy. The only approximations present are the discretization of the soil-structure interface, the modal truncation, and the rounding errors in the determination of the eigenfrequencies and eigenwavenumbers. At the same time, the number of equations

to be solved is minimal compared to a FEM or BEM model, making the computation more efficient.

2.1.2 Assumptions

The tank itself is modeled as a combination of shell elements; the bottom plate is a circular plate, while the wall is represented by cylindrical shell elements. Liquid storage tanks often have walls consisting of multiple stacked segments of varying thickness, which is reflected in the model by the possibility to incorporate any number n wall segments. All parts of the tank are assumed to be connected at their mid-surfaces. The tank model does not include ring stiffeners, a roof, or anchors.
The description of the shell's motions is based on Love's theory. This assumes a small shell thickness, compared to the smallest radius of curvature, so that the in-plane motions vary linearly through the shell thickness. Furthermore, small displacements and strains are assumed in order to accurately describe motions in the linear regime. In addition, straight lines normal to the middle surface remain straight during deformations, which implies that shear strains, as well as normal strains in the out-of-plane direction, are 0 (Soedel (2005)).
The tank's material is considered to be homogeneous, isotropic, and linearly elastic. Finally, if material damping is included, possible through adding an imaginary term to the material's modulus of elasticity (Tsouvalas (2015)), coupled complex modes are found in theory, so that linear superposition of the modes is not possible. However, for small material damping values, e.g. of steel, the effect of coupling of the modes on the tank's total response is considered negligible.
The fluid is modeled as being inviscid, irrotational, and incompressible, as is customary for this type of system (Amabili et al. (1998); Bauer and Siekmann (1971)). The latter assumption does not allow normal strains to develop, so that compressional waves, and therefore the effects of disturbances, move with an infinite wave speed. Considering the compressional wave speeds in different types of fluid and the dimensions of the tank, disturbances can be considered to spread through the tank's content approximately instantaneously, so that this simplification is acceptable.
The effects of vorticity, or rotational flow, are in fluid dynamics related to the influence of a boundary. In the case of the liquid storage tanks, however, the influence of the vorticity at the small layer near the fluid-structure interface on the seismic behavior of the entire system is considered to be negligible. Assuming an inviscid fluid neglects the development of viscous stresses that arise from the energy transport between two fluid domains that travel with different speeds (Linton and McIver (2001)). While this energy transport tends to occur for the flow of a fluid near a rigid boundary, as was the case for rotational flow, this effect is not considered to have any significant impact on the seismic behavior of the entire system.
The soil substructure is considered as a homogeneous, isotropic, linear elastic, infinite, horizontal layer on top of immovable bedrock. Few soils satisfy all assumptions, given that soil is often heterogeneous and behaves nonlinearly. However, the representation of soil as a three-dimensional continuum is considered to be far more realistic than previous soil representations in tank-fluid-soil models. In addition, extending the model to incorporate a larger number of soil layers to improve the model further is relatively easy and does not introduce additional complexity in the solution method elaborated in this thesis.

2.2 Tank

The tank substructure consists of two parts, namely the bottom and the wall, that are described by a plate element and cylindrical shell elements, respectively. Both parts experience motions in-plane and out-of-plane of the mid-surface, which can be described with three degrees of freedom.
For both parts, the equations of motion are formulated below, describing the forces (in units of pressure) that are related to the motions of the plate. These can thus be regarded as the dynamic conditions the system needs to satisfy. They are formulated according to Love's shell theory and are of the form (Soedel (2005))

$$L_i(u_1, u_2, u_3) + q_i = \rho h \frac{\partial^2 u_i}{\partial t^2} \tag{2.2}$$

in which u_i is the displacement in the i-th degree of freedom, L represents internal forces from deformations, q represents external forces, and the right-hand side of the equation describes the inertia forces. The external forces for each tank part are attributed to a combination of pressure from the fluid and stresses from the soil.
For each degree of freedom, the eigenfunctions are presented, with references made to the relevant appendices for their derivations. To arrive at the vibration shapes of the entire tank, the boundary and interface conditions are formulated, to which the different tank parts must adhere (section 2.2.3). This is followed by a short description of the numerical procedure followed to determine the eigenfrequencies and vibration shapes of the entire tank.

2.2.1 Equations of motion - bottom plate

The equations of motion of the circular bottom plate are given below with degrees of freedom in radial, circumferential, and vertical direction. Please note that positive displacements of the plate in the vertical direction are downward, as a result of aligning the positive directions of the circumferential degree of freedom for the bottom plate and the wall (figure 2.2).

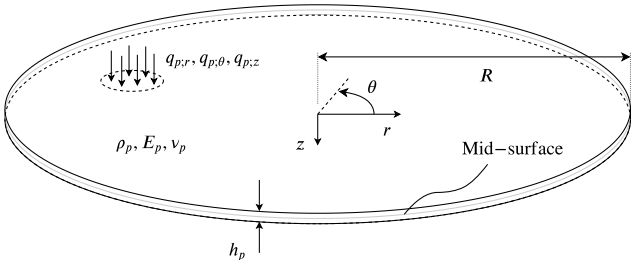

Figure 2.2 – *Geometrical and material properties of the bottom plate. External forces shown in positive z-direction, but can act in each degree of freedom.*

The three equations can be written in matrix form as

$$\mathbf{L}_p \mathbf{u}_p(r, \theta, t) + \mathbf{I}_p \ddot{\mathbf{u}}_p(r, \theta, t) = \boldsymbol{\sigma}_s(r, \theta, t) + \mathbf{p}_{fl}(r, \theta, t) \tag{2.3}$$

The 3×3 matrix $\mathbf{L}_p$, representing the stiffness of the plate, and the 3×3 matrix $\mathbf{I}_p$, representing the inertia of the plate, are given in more detail in section A.1.2. Displacements are

denoted by $\mathbf{u}_p(r,\theta,t) = [u_{p;r}, u_{p;\theta}, u_{p;z}]^T$, Newton's dot notation is used to denote its time derivatives, fluid pressure by $\mathbf{p}_{fl} = [0, 0, p_{fl;z}]^T$ and soil stresses by $\boldsymbol{\sigma}_s = [\sigma_{s;r}, \sigma_{s;\theta}, \sigma_{s;z}]^T$. With the forward Fourier transform (equation (2.1)), equation (2.3) can be rewritten as

$$\mathbf{L}_p\tilde{\mathbf{u}}_p(r,\theta,\omega) - \omega^2\mathbf{I}_p\tilde{\mathbf{u}}_p(r,\theta,\omega) = \tilde{\boldsymbol{\sigma}}_s(r,\theta,\omega) + \tilde{\mathbf{p}}_{fl}(r,\theta,\omega) \tag{2.4}$$

In the applied solution method, the soil is considered through a dynamic soil stiffness matrix, $\mathbf{K}_s(\omega)$, which comes into expression in the soil stresses acting on the plate as

$$\boldsymbol{\sigma}_s(r,\theta,\omega) = \mathbf{K}_s(r,\theta,\omega)\left(\tilde{\mathbf{u}}_i(r,\theta,\omega) - \tilde{\mathbf{u}}_p(r,\theta,\omega)\right) = \begin{bmatrix} K_{rr} & K_{r\theta} & K_{rz} \\ K_{\theta r} & K_{\theta\theta} & K_{\theta z} \\ K_{zr} & K_{z\theta} & K_{zz} \end{bmatrix} \left(\begin{bmatrix} u_{i;r} \\ u_{i;\theta} \\ u_{i;z} \end{bmatrix} - \begin{bmatrix} u_{p;r} \\ u_{p;\theta} \\ u_{p;z} \end{bmatrix} \right) \tag{2.5}$$

The dynamic soil stiffness matrix is treated more in-depth in section 2.4, whereas details on the incorporation of dynamic and kinematic SSI can be found in section 2.4.4. It is noted that equation (2.5) holds when the prescribed displacements $\tilde{\mathbf{u}}_i(r,\theta,\omega)$ have the same positive direction as $\tilde{\mathbf{u}}_p(r,\theta,\omega)$.

Although the equations of the in-plane motion are uncoupled from the equation of the out-of-plane motion for the general case, as shown in section A.1.2, including SSI through the dynamic soil stiffness matrix couples the degrees of freedom. Through the stiffness matrix, a displacement in the z-direction causes stresses in the θ- and r-directions, and similarly, forces develop for the other combinations of degrees of freedom.

Through formulation of the eigenvalue problem

$$\mathbf{L}_p\tilde{\mathbf{u}}_p(r,\theta,\omega) - \omega^2\mathbf{I}_p\tilde{\mathbf{u}}_p(r,\theta,\omega) = \mathbf{0} \tag{2.6}$$

and transformation to the frequency domain and separation of variables, the following eigenfunction expansions are found for each degree of freedom of the plate (section A.1.2):

$$\begin{aligned}
\tilde{u}_{p;r}(r,\theta,\omega) &= \sum_{m=1}^{\infty}\sum_{n=0}^{\infty}\left[\tilde{C}_{mn}\frac{\mathrm{d}J_n(k_{\Phi;mn}r)}{\mathrm{d}r} + \tilde{D}_{mn}\frac{n}{r}J_n(k_{\Psi;mn}r)\right]\cos(n\theta) \\
\tilde{u}_{p;\theta}(r,\theta,\omega) &= \sum_{m=1}^{\infty}\sum_{n=0}^{\infty}\left[-\tilde{C}_{mn}\frac{n}{r}J_n(k_{\Phi;mn}r) - \tilde{D}_{mn}\frac{\mathrm{d}J_n(k_{\Psi;mn}r)}{\mathrm{d}r}\right]\sin(n\theta) \\
\tilde{u}_{p;z}(r,\theta,\omega) &= \sum_{m=1}^{\infty}\sum_{n=0}^{\infty}\left[\tilde{A}_{mn}J_n(k_{mn}r) + \tilde{B}_{mn}I_n(k_{mn}r)\right]\cos(n\theta)
\end{aligned} \tag{2.7}$$

The trigonometric functions give the shapes in circumferential direction, whereas the terms with J_n and I_n, respectively the Bessel function and modified Bessel function (both of the first kind) express the shapes in radial direction. The value of n is the eigenwavenumber in circumferential direction and $k_{\Phi;mn}$, $k_{\Psi;mn}$ and k_{mn} are the eigenwavenumbers in radial direction of radial mode m and circumferential mode n. They are defined as

$$\begin{aligned}
k_{\Phi;mn}^2 &= \frac{\omega_{mn}^2\rho_p}{E_p}\left(1-\nu_p^2\right) \\
k_{\Psi;mn}^2 &= \frac{\omega_{mn}^2\rho_p}{E_p}\,2(1+\nu_p) \\
k_{mn}^4 &= \frac{\omega_{mn}^2\rho_p}{E_p}\,\frac{12(1-\nu_p^2)}{h_p^2}
\end{aligned} \tag{2.8}$$

The only unknowns in equations (2.7) and (2.8) are the eigenfrequencies ω_{mn}^2 and the constants A_{mn}, B_{mn}, C_{mn} and D_{mn}. The procedure to determine them is explained in more detail in section 2.2.4.

2.2.2 Equations of motion - wall segments

The cylindrical shells representing the wall segments that make up the tank wall also have degrees of freedom in the vertical, circumferential, and radial direction. Basic properties of the wall segments are shown in figure 2.3.

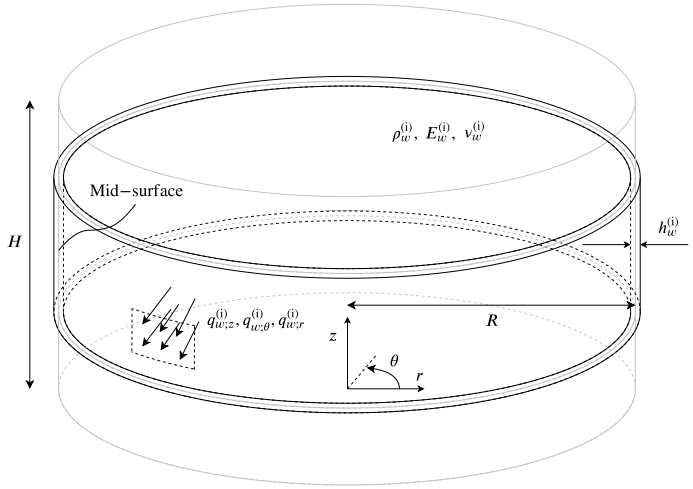

Figure 2.3 – *Geometrical and material properties of wall segment i. External forces shown in positive r-direction, but can act in each degree of freedom.*

Their coupled equations of motion can be written in matrix form as

$$\mathbf{L}_w^{(i)}\mathbf{u}_w^{(i)}(z,\theta,t) + \mathbf{I}_w^{(i)}\ddot{\mathbf{u}}_w^{(i)}(z,\theta,t) = \mathbf{p}_{fl}^{(i)}(z,\theta,t) \tag{2.9}$$

The 3×3 matrix $\mathbf{L}_w^{(i)}$ represents the stiffness of wall segment i, and the 3×3 matrix $\mathbf{I}_w^{(i)}$ represents the inertia of wall segment i. Their expressions can be found in more detail in section A.1.3. Displacements are denoted by $\mathbf{u}_w^{(i)}(z,\theta,t) = [u_{w;z}^{(i)}, u_{w;\theta}^{(i)}, u_{w;r}^{(i)}]^T$ and Newton's dot notation is used to denote its time derivatives. The external force in this case is the fluid pressure, $\mathbf{p}_{fl}^{(i)} = [0, 0, p_{fl}^{(i)}]^T$.
Eigensolutions to satisfy the eigenvalue problem associated with equation (2.9)

$$\mathbf{L}_w^{(i)}\mathbf{u}_w^{(i)}(z,\theta,t) + \mathbf{I}_w^{(i)}\ddot{\mathbf{u}}_w^{(i)}(z,\theta,t) = \mathbf{0} \tag{2.10}$$

are sought in the form:

$$\begin{aligned} u^{(i)}_{w;z}(z,\theta,\omega) &= \sum_{m=1}^{\infty}\sum_{n=0}^{\infty}\sum_{l=1}^{8} U^{(i)}_{z;mnl}\exp(\lambda^{(i)}_{mnl}z)\cos(n\theta)\exp(i\omega_{mn}t) \\ u^{(i)}_{w;\theta}(z,\theta,\omega) &= \sum_{m=1}^{\infty}\sum_{n=0}^{\infty}\sum_{l=1}^{8} U^{(i)}_{\theta;mnl}\exp(\lambda^{(i)}_{mnl}z)\sin(n\theta)\exp(i\omega_{mn}t) \\ u^{(i)}_{w;r}(z,\theta,\omega) &= \sum_{m=1}^{\infty}\sum_{n=0}^{\infty}\sum_{l=1}^{8} U^{(i)}_{r;mnl}\exp(\lambda^{(i)}_{mnl}z)\cos(n\theta)\exp(i\omega_{mn}t) \end{aligned} \tag{2.11}$$

The exponential function related to time expresses the assumption that the tank wall is expected to vibrate harmonically at the eigenfrequencies ω_{mn}. The latter are at this stage unknown, but can be found by specifying boundary conditions, substituting equation (2.11) into those boundary conditions, and finding the nontrivial solution of the related eigenvalue problem. This is discussed in more detail in section 2.2.4.
The trigonometric functions again represent the shapes in circumferential direction. For the summation over their wavenumber, the same symbol, n, the foresight is used that the circumferential modes of the plate and the cylindrical shells are coupled through the interface between the wall and the plate. The linear combination of the exponential functions determines the vibration shape in vertical direction.
The eigenwavenumbers $\lambda^{(i)}_{mnl}$ are the eigenvalues of the eigenvalue problem in equation (2.10). After substitution of equation (2.11) into equation (2.10), the function related to time cancels out and the stiffness and inertia matrix can be summed to form a new matrix, $\mathbf{M}$. The characteristic equation related to this matrix is a polynomial of order eight, hence the summation limits of l. A polynomial of this order has no closed-form solution, as was the case for the plate's wavenumbers in equation (2.8).
Finally, the unknown constants $U^{(i)}_{z;mnl}$, $U^{(i)}_{\theta;mnl}$ and $U^{(i)}_{r;mnl}$ are related to one another through

$$\begin{aligned} U^{(i)}_{z;mnl} &= \gamma^{(i)}_{mnl}\, U^{(i)}_{r;mnl} \\ U^{(i)}_{\theta;mnl} &= \delta^{(i)}_{mnl}\, U^{(i)}_{r;mnl} \end{aligned} \tag{2.12}$$

The factors $\gamma^{(i)}_{mnl}$ and $\delta^{(i)}_{mnl}$ depend on the stiffness and inertia properties of wall segment i and can be expressed through matrix $\mathbf{M}$ as

$$\begin{aligned} \gamma^{(i)}_{mnl} &= \frac{M_{12}M_{23} - M_{13}M_{22}}{M_{12}^2 - M_{11}M_{22}} \\ \delta^{(i)}_{mnl} &= \frac{M_{12}M_{13} - M_{11}M_{23}}{M_{12}^2 - M_{11}M_{22}} \end{aligned} \tag{2.13}$$

At each eigenfrequency ω_{mn}, each wall segment i therefore has eight unknown constants, $U^{(i)}_{r;mnl}$.

2.2.3 Boundary and interface conditions

Up to this point, the equations of motion and the eigenfunction expansions have been formulated for each tank part individually. However, the tank parts are connected to each other, while the top of the wall is free to vibrate. To include these physical aspects in the

mathematical description of the tank, boundary and interface conditions must be specified. Thus, these must represent the fact that the bottom plate is connected monolithically to the lowest wall segment, that the wall segments are also connected monolithically to each segment above and below, and that the upper edge of the upper wall segment is free to displace and rotate around the circumferential axis. These conditions have been specified by Tsouvalas (2006), based on the work by Soedel (2005).
At the interface between the bottom plate and the lowest wall segment, the following condition specifies at the outer edge of the bottom plate and the bottom edge of the bottom wall segment, the continuity of displacements in z, θ and r, as well as the continuity of slopes ϕ.

$$\mathbf{u}_w^b(z=0,\theta,t) = \mathbf{u}_p(r=R,\theta,t) \tag{2.14}$$

with $\mathbf{u}_w^b = [u_{w;z}^b, u_{w;\theta}^b, u_{w;r}^b, \phi_{w;z}^b]^T$ (with $\phi_{w;z}^b = -\partial u_{w;z}^b/\partial z$) and $\mathbf{u}_p = [u_{p;z}, u_{p;\theta}, u_{p;r}, \phi_{p;r}]^T$ (with $\phi_{p;r} = -\partial u_{p;r}/\partial r$) (see figure 2.4).
In addition, at this interface, there is a continuity of forces, namely

$$\mathbf{f}_w^b(z=0,\theta,t) = \mathbf{f}_p(r=R,\theta,t) \tag{2.15}$$

with $\mathbf{f}_w = [M_{zz}, N_{zz}, V_{zr}, T_{z\theta}]^T$ and $\mathbf{f}_p = [M_{rr}, V_r, N_{rr}, N_{r\theta}]^T$.

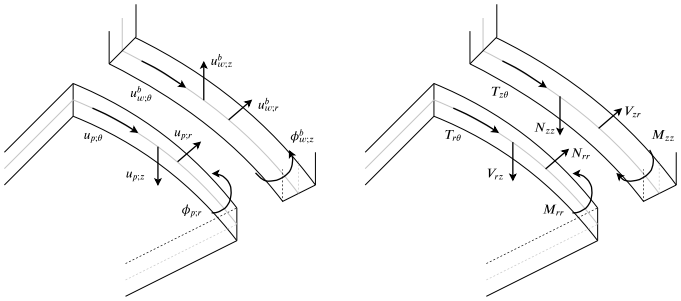

Figure 2.4 – *Bottom view of displacement (left) and force (right) continuity at the interface between the bottom plate and the bottom wall segment.*

Each wall segment, except for the bottom and top ones, is connected monolithically to the wall segments above and below. Again, this means continuity of the displacements in all degrees of freedom and the slope along the vertical direction (figure 2.5), so

$$\mathbf{u}_w^{(i)}(z=Z_{\text{if}}^{(i)},\theta,t) = \mathbf{u}_w^{(i+1)}(z=Z_{\text{if}}^{(i)},\theta,t) \tag{2.16}$$

with $\mathbf{u}_w^{(i)} = [u_{w;z}^{(i)}, u_{w;\theta}^{(i)}, u_{w;r}^{(i)}, \phi_{w;z}^{(i)}]^T$. The index i denotes the i-th wall segment, and $Z_{\text{if}}^{(i)}$ the z-coordinate at which the interface between wall segment i and $i+1$ is located. In addition, there is a continuity of forces at the interfaces between the wall segments, expressed as

$$\mathbf{f}_w^{(i)}(z=Z_{\text{if}}^{(i)},\theta,t) = \mathbf{f}_w^{(i+1)}(z=Z_{\text{if}}^{(i)},\theta,t) \tag{2.17}$$

again with $\mathbf{f}_w = [M_{zz}, N_{zz}, V_{zr}, T_{z\theta}]^T$.

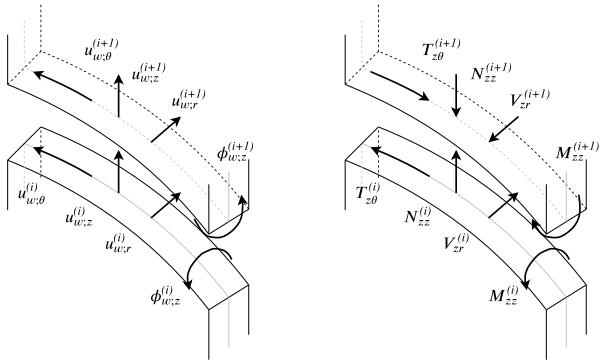

Figure 2.5 – *Displacement (left) and force (right) continuity at the interface between two wall segments.*

Finally, at the top of the top wall segment, the shell is free to displace. As a result, the internal forces at the top edge are equal to zero:

$$\mathbf{f}_w^t(z = H, \theta, t) = \mathbf{0} \tag{2.18}$$

in which H is the height of the tank, so the coordinate at the upper edge of the top wall segment, and $\mathbf{f}_w^t$ are the forces in the top wall segment, which are the same as shown in figure 2.5.

2.2.4 Mode shapes and eigenfrequencies

To find the mode shapes and eigenfrequencies of the tank, an eigenvalue problem must be formulated and solved. It is noted that each of the displacements and forces specified in the boundary and interface conditions (equations (2.14) to (2.18)) can be expressed in terms of known material and geometrical properties and unknown displacements $u_{p;r}$, $u_{p;\theta}$, $u_{p;z}$, $u_{w;z}$, $u_{w;\theta}$ and $u_{w;r}$. At the same time, expressions for the displacements have been formulated in terms of eigenfunction expansions in equations (2.7) and (2.11). As was stated before, the only unknowns in these expressions are the eigenfrequencies and unknown constants: 4 for the plate and 8 per wall segment.
To formulate the eigenvalue problem, equations (2.7) and (2.11) are substituted into equations (2.14) to (2.18). This produces a system of $4 + 8n_{segments}$ equations and an equal number of unknown constants, which can be rewritten to

$$\mathbf{G}\mathbf{c} = \mathbf{0} \tag{2.19}$$

in which the entries of matrix $\mathbf{G}$ are frequency dependent and the vector $\mathbf{c}$ contains the unknown constants of the eigenfunction expansions. By setting

$$\mathrm{Det}\,(\mathbf{G}) = 0 \tag{2.20}$$

the nontrivial solution to the system of equations can be found. The values of the frequency at which equation (2.20) holds, are the eigenfrequencies, while the related eigenvector, $\mathbf{c}$, gives the ratios of all the unknown constants in equations (2.7) and (2.11). Due to the transcendental nature of $\mathrm{Det}(\mathbf{G})$, an infinite number of eigenfrequencies can be found. Given the fact that the ratios between the unknowns $\tilde{A}_{mn}$, $\tilde{B}_{mn}$, $\tilde{C}_{mn}$, $\tilde{D}_{mn}$ and $\tilde{U}_{r;mnl}^{(i)}$ have been

found, the vibration shapes or modes at each eigenfrequency are now known. The amplitudes of each mode are dependent on the frequency of excitation and can be expressed by a single parameter, X_{mn}. Expressions for the motions the plate and the wall segments can be written as

$$\tilde{\mathbf{u}}_p(r,\theta,\omega) = \sum_{m=1}^{\infty}\sum_{n=0}^{\infty} \tilde{X}_{mn}(\omega)\tilde{\mathbf{U}}_{p;mn}(r,\theta) \tag{2.21}$$

in which

$$\tilde{\mathbf{U}}_{p;mn}(r,\theta) = \begin{bmatrix} \tilde{U}_{p;rmn}(r)\cos(n\theta) \\ \tilde{U}_{p;\theta mn}(r)\sin(n\theta) \\ \tilde{U}_{p;zmn}(r)\cos(n\theta) \end{bmatrix} \tag{2.22}$$

and

$$\tilde{\mathbf{u}}_w(z,\theta,\omega) = \sum_{m=1}^{\infty}\sum_{n=0}^{\infty} \tilde{X}_{mn}(\omega)\tilde{\mathbf{U}}_{w;mn}(z,\theta) \tag{2.23}$$

in which

$$\tilde{\mathbf{U}}_{w;mn}(z,\theta) = \begin{bmatrix} \tilde{U}_{w;zmn}(z)\cos(n\theta) \\ \tilde{U}_{w;\theta mn}(z)\sin(n\theta) \\ \tilde{U}_{w;rmn}(z)\cos(n\theta) \end{bmatrix} \tag{2.24}$$

Finally, the vibration mode shapes satisfy the orthogonality relation

$$\int_{\theta=0}^{2\pi}\int_{r=0}^{R} \tilde{\mathbf{U}}_{w;mn}^T\tilde{\mathbf{U}}_{w;qs}\mathrm{d}r\mathrm{d}\theta + \int_{\theta=0}^{2\pi}\int_{r=0}^{R} \tilde{\mathbf{U}}_{p;mn}^T\tilde{\mathbf{U}}_{p;qs}\mathrm{d}r\mathrm{d}\theta = \Gamma_{mn}\delta_{mq}\delta_{ns} \tag{2.25}$$

which will be applied at a later stage in section 2.5.
Because equation (2.20) has no closed-form solution, the eigenfrequencies of the tank are found numerically. The procedure is performed by considering a range of frequencies, using each frequency to compute all frequency dependent values in matrix $\mathbf{G}$ and checking whether equation (2.20) holds. While theoretically the inclusion of material damping would yield complex modes and eigenfrequencies, in this case the damping is assumed to be negligible, so that the imaginary part of the modes is negligible. Eigenfrequencies are therefore sought in the postive real domain.

2.3 Fluid

The fluid in the tank is modeled as inviscid, irrotational and incompressible, as described previously. The first two allow the application of potential flow theory (Linton and McIver (2001)), so that the velocity of the fluid may be expressed as

$$\mathbf{v}_{fl}(r,\theta,z,t) = \nabla\phi(r,\theta,z,t) \tag{2.26}$$

The assumption of incompressibility further reduces the wave equation that describes the fluid's motion to Laplace's equation, so

$$\nabla^2\phi(r,\theta,z,t) = 0 \tag{2.27}$$

The motions of the fluid in the tank in all degrees of freedom, once again r, θ and z, can now be described in terms of the velocity potential. The resulting pressures (figure 2.6) on the tank can be found from the linearized Bernoulli equation:

$$p_{fl}(r,\theta,z,t) = -\rho_{fl}\dot{\phi}(r,\theta,z,t) \tag{2.28}$$

More detailed derivations can be found in the work of, for example, Linton and McIver (2001); Tsouvalas (2017).
The approach to solving equation (2.27) is again to find the eigenfunctions and use them in a modal series expansion with amplitudes that depend on the excitation.

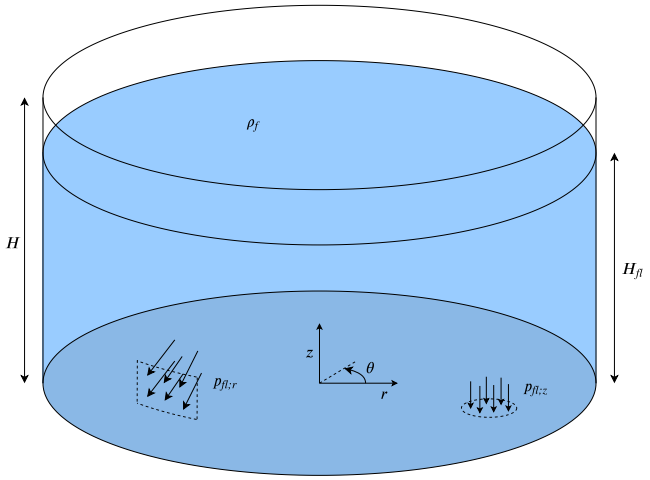

Figure 2.6 – *Material properties of the fluid and the positive directions of the fluid pressure.*

2.3.1 Velocity potential

Some foresight is used regarding the satisfaction of the boundary conditions and the velocity potential is rewritten as the superposition of three potential functions

$$\phi(r,\theta,z,t) = \phi_1(r,\theta,z,t) + \phi_2(r,\theta,z,t) + \phi_3(r,\theta,z,t) \tag{2.29}$$

that each must satisfy equation (2.27). The boundary and interface conditions the system needs to adhere to are: velocity continuity at the interface with the wall, velocity continuity at the interface with the plate, and the free surface at the water level. While displacement continuity was used in the case of the tank, using the velocity is simpler in this case. Mathematically, these are expressed respectively as

$$\begin{aligned}
\left.\frac{\partial\phi(r,\theta,z,t)}{\partial r}\right|_{r=R} &= \frac{\partial u_{w;r}(z,\theta,t)}{\partial t} \\
\left.\frac{\partial\phi(r,\theta,z,t)}{\partial z}\right|_{z=0} &= -\frac{\partial u_{p;z}(r,\theta,t)}{\partial t} \\
\left.\frac{1}{g}\frac{\partial^2\phi(r,\theta,z,t)}{\partial t^2}\right|_{z=H_{fl}} &= -\left.\frac{\partial\phi(r,\theta,z,t)}{\partial z}\right|_{z=H_{fl}}
\end{aligned} \tag{2.30}$$

The decomposition in equation (2.29) can now be applied to have each of the scalar functions of the total potential satisfy a subset of the conditions, while the others satisfy a homogeneous boundary condition. As such, the fluid-tank system is regarded as the summation of three fluid-tank systems, that each satisfy the boundary and interface conditions, such that

their sum yields the original fluid-tank system (see figure 2.7).
The fluid velocity at the wall, for example, is then the summation of the velocities of each of the three virtual fluid-tank systems, only the first of which has a non-zero velocity at the fluid-wall interface, so that

$$\left.\frac{\partial \phi(r,\theta,z,t)}{\partial r}\right|_{r=R} = \left.\frac{\partial \phi_1(r,\theta,z,t)}{\partial r}\right|_{r=R} + 0 + 0 \tag{2.31}$$

Since each of the potential functions now, in addition, has homogeneous boundary conditions in one of the directions, a solution can be found through an eigenfunction expansion. So first, each of these functions is transformed to the frequency domain (equation (2.1)) and solved by means of the method of separation of variables. This procedure is treated in detail by others, such as Amabili et al. (1998); Bauer and Siekmann (1971); Canny (2018); Tsouvalas et al. (2018), so is not covered further in this thesis.

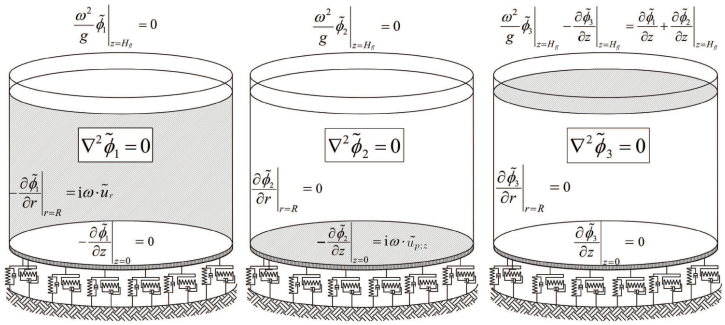

Figure 2.7 – *Satisfaction of the boundary conditions through the decomposition of the fluid potential, adopted from Tsouvalas et al. (2018).*

The resulting modal expressions of the liquid potentials are

$$\begin{aligned}\tilde{\phi}(r,\theta,z,\omega) &= \tilde{\phi_1}(r,\theta,z,\omega) + \tilde{\phi_2}(r,\theta,z,\omega) + \tilde{\phi_3}(r,\theta,z,\omega) \\ &= \sum_{n=0}^{\infty}\sum_{a=1}^{\infty}\tilde{P}_{na}(\omega)\tilde{\Phi}^1_{na} + \sum_{n=0}^{\infty}\sum_{b=1}^{\infty}\tilde{Q}_{nb}(\omega)\tilde{\Phi}^2_{nb} + \sum_{n=0}^{\infty}\sum_{c=1}^{\infty}\tilde{S}_{nc}(\omega)\tilde{\Phi}^3_{nc}\end{aligned} \tag{2.32}$$

$$\begin{aligned}\tilde{\Phi}^1_{na}(r,\theta,z) &= I_n\left(\frac{\pi(2a-1)r}{2H_l}\right)\cos\left(\frac{\pi(2a-1)z}{2H_l}\right)\cos(n\theta) \\ \tilde{\Phi}^2_{nb}(r,\theta,z) &= \left(\cosh(\varepsilon_{nb}z/R) - \frac{\sinh(\varepsilon_{nb}z/R)}{\tanh(\varepsilon_{nb}H_l/R)}\right)J_n(\varepsilon_{nb}r/R)\cos(n\theta) \\ \tilde{\Phi}^3_{nc}(r,\theta,z) &= \cosh(\varepsilon_{nc}z/R)J_n(\varepsilon_{nc}r/R)\cos(n\theta)\end{aligned} \tag{2.33}$$

2.4 Soil

The soil substructure is reduced in the model to a dynamic stiffness matrix, connected to the tank-fluid system through the equations of motion of the bottom plate (equation (2.3)). To construct that matrix, first, the force response of the soil layer (figure 2.8) is found to a unit uniform time-dependent load on a circular area on the soil surface, both in horizontal and

vertical directions (figure 2.9). Then, the soil-structure interface is discretized into circular elements. The response at each location i to a load at each location j can be calculated and structured as the entries of the dynamic stiffness matrix.
This matrix is subsequently implemented in the equation of motion of the bottom plate, as it relates the displacements of the plate to the resulting stresses from the soil. The surface Green's functions are thus applied because the soil-structure interaction occurs at the soil surface. The incorporation of SSI is explained in more detail in section 2.4.4.

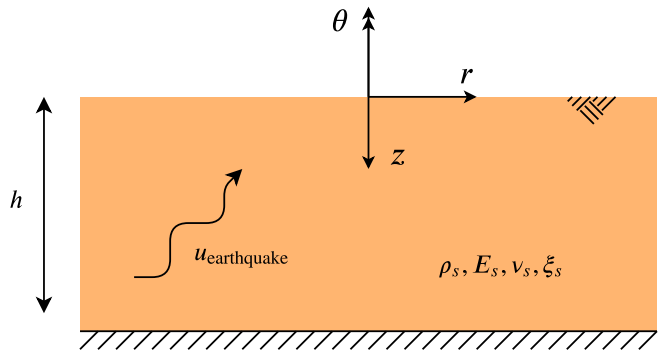

Figure 2.8 – *Soil layer of height h with a free surface, located on top of bedrock and excited by seismic waves.*

The initial assumptions under which the flexibility functions are derived, stresses on the circular area and zero stresses outside the circular area (figure 2.9), may seem to be violated through this discretization of the interface into many loaded elements. However, the model is linear, so that the principle of superposition may be applied. The stress field can be thought of as a superposition of stress fields in which each of the elements is loaded by itself, while the other elements are not loaded. The response to the superposition of these load situations is the superposition of the individual responses to each load situation. The advantage of this approach is that, with a sufficiently fine discretization, any displacement field can be transformed into a corresponding stress field acting on the bottom plate. Alternatively, finding the Green's functions relating stress and displacement for any given displacement field in a circle is relatively complex.

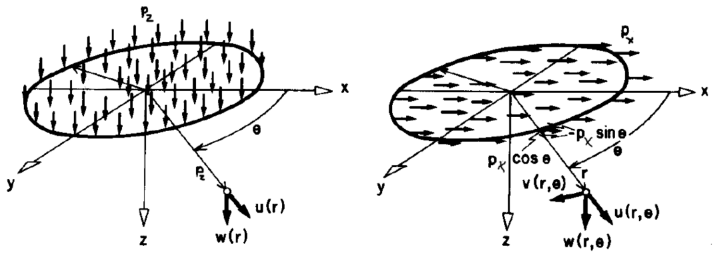

Figure 2.9 – *Vertical (left) and horizontal (right) load case*

Below, the Green's functions are given, as well as an explanation on their derivation. For the complete derivation of these functions, see Molenkamp (2018) and Wolf (1985). Also, the

applied discretization is briefly discussed, as well as the assembly of the dynamic stiffness matrix in cylindrical coordinates. This section concludes with remarks on the inclusion of kinematic soil-structure interaction.

2.4.1 Green's influence functions

The displacements in the soil layer are specified below as a function of the amplitudes of the load described in figure 2.9, the Green's influence functions. Similar to the displacements of the tank and the velocity potential of the fluid, the displacements are written as an infinite sum over vibration shapes that in this case depend on the wavenumbers of SH-waves and PSV-waves. The equations in this section are adopted from Molenkamp (2018) and Wolf (1985) with only minor changes.
The vibration shapes and related wavenumbers are found through solving the eigenvalue problem to the motions of the soil, which are described by the wave equation

$$G_s \nabla^2 \mathbf{u} + (\lambda_s + G_s) \nabla \nabla \cdot \mathbf{u} + \mathbf{f} = \rho_s \ddot{\mathbf{u}} \tag{2.34}$$

in which ∇^2 is the Laplace operator, $\mathbf{u}$ represents the three-dimensional soil displacements and $\mathbf{f}$ represents the three-dimensional forces. The parameters λ_s and G_s are Lamé's first parameter and the shear modulus respectively, expressed as

$$\begin{aligned} G_s &= \sqrt{\frac{E_s(1+i\xi_s)}{2(1+\nu_s)}} \\ \lambda_s &= \frac{E_s \nu_s (1+2i\xi_s)}{(1+\nu_s)(1-2\nu_s)} \end{aligned} \tag{2.35}$$

in which E_s is the soil's modulus of elasticity, ξ_s the soil material damping ratio and ν_s the soil's Poisson's ratio.
Solutions to the wave equation contain a function related to the horizontal coordinates and the vertical coordinate:

$$\begin{aligned} \tilde{u}_n &= \frac{1}{k} \frac{\partial J_n(kr)}{\partial r} u(z) + \frac{n}{kr} J_n(kr) v(z) \\ \tilde{v}_n &= \frac{n}{kr} J_n(kr) u(z) + \frac{1}{k} \frac{\partial J_n(kr)}{\partial r} v(z) \\ \tilde{w}_n &= -J_n(kr) w(z) \end{aligned} \tag{2.36}$$

with the solution for the vertical coordinate:

$$\begin{aligned} u(z) &= l_x \left(A_p \mathrm{e}^{iksz} + B_p \mathrm{e}^{-iksz} \right) - m_x t \left(A_{sv} \mathrm{e}^{iktz} - B_{sv} \mathrm{e}^{-iktz} \right) \\ v(z) &= A_{sh} \mathrm{e}^{iktz} + B_{sh} \mathrm{e}^{-iktz} \\ w(z) &= -il_x s \left(A_p \mathrm{e}^{iksz} - B_p \mathrm{e}^{-iksz} \right) - im_x \left(A_{sv} \mathrm{e}^{iktz} + B_{sv} \mathrm{e}^{-iktz} \right) \end{aligned} \tag{2.37}$$

Through the constitutive relations, solutions can also be found for the stresses at the soil surface:

$$\begin{aligned} \tilde{\sigma}_{zr} &= \frac{1}{k} \frac{\partial J_n(kr)}{\partial r} \sigma_{zr}(z) + \frac{n}{kr} J_n(kr) \sigma_{z\theta}(z) \\ \tilde{\sigma}_{z\theta} &= \frac{n}{kr} J_n(kr) \sigma_{zr}(z) + \frac{1}{k} \frac{\partial J_n(kr)}{\partial r} \sigma_{z\theta}(z) \\ \tilde{\sigma}_{zz} &= -J_n(kr) \sigma_{zz}(z) \end{aligned} \tag{2.38}$$

with

$$\begin{aligned}
\sigma_{zr}(z) &= i2l_x sG_s\left(A_p\mathrm{e}^{iksz} - B_p\mathrm{e}^{-iksz}\right) + ikm_x(1-t^2)G_s\left(A_{sv}\mathrm{e}^{iktz} - B_{sv}\mathrm{e}^{-iktz}\right)\\
\sigma_{z\theta}(z) &= iktG_s\left(A_{sh}\mathrm{e}^{iktz} + B_{sh}\mathrm{e}^{-iktz}\right)\\
\sigma_{zz}(z) &= -kl_x(1-t^2)G_s\left(A_p\mathrm{e}^{iksz} + B_p\mathrm{e}^{-iksz}\right) - 2km_xtG_s\left(A_{sv}\mathrm{e}^{iktz} - B_{sv}\mathrm{e}^{-iktz}\right)
\end{aligned} \tag{2.39}$$

As was the case for the other substructures, the unknowns in this case are the wavenumbers and the amplitudes related to the eigenfunctions.
A difference in this case is that the soil is bounded in the vertical direction, but unbounded in horizontal direction. While standing waves, or vibrations, are the result of constructive interference of reflected waves, waves will not be reflected in an unbounded domain, so that standing waves can only form for the vertical coordinate. For a given frequency and for every mode with a given vertical component, k_v, a horizontal component, k_h, can be found through

$$k_h^2 = \frac{\omega^2}{c^2} - k_v^2 \tag{2.40}$$

which is the value that is summed over in the modal summation in equations (2.43) and (2.44). The value of this component additionally determines whether the waves are propagating (real or complex values) or evanescent (imaginary values).
Through substitution of equations (2.36) to (2.39) into the free vibration boundary conditions of the soil layer, namely free displacements at the surface and a rigid boundary at the bottom of the layer, the following two matrix equations result:

$$\begin{bmatrix}
l_x\mathrm{e}^{iksh} & l_x\mathrm{e}^{-iksh} & -m_xt\mathrm{e}^{ikth} & m_xt\mathrm{e}^{-ikth}\\
-il_xs\mathrm{e}^{iksh} & il_xs\mathrm{e}^{-iksh} & -im_x\mathrm{e}^{ikth} & -m_x\mathrm{e}^{-ikth}\\
2ikl_xsG_s & -2ikl_xG_s & ikm_x(1-t^2)G_s & ikm_x(1-t^2)G_s\\
-kl_x(1-t^2)G_s & -kl_x(1-t^2)G_s & 2km_xtG_s & -2km_xtG_s
\end{bmatrix}\begin{bmatrix}A_p\\B_p\\A_{sv}\\B_{sv}\end{bmatrix} = \mathbf{0} \tag{2.41}$$

and

$$\begin{bmatrix}\mathrm{e}^{ikth} & \mathrm{e}^{-ikth}\\ iktG_s & -iktG_s\end{bmatrix}\begin{bmatrix}A_{sh}\\B_{sh}\end{bmatrix} = \mathbf{0} \tag{2.42}$$

Equation (2.41) is related to the PSV wavenumbers, while equation (2.42) is related to the SH wavenumbers.
The wavenumbers and mode shapes can then be used to find the displacements at any location in the soil layer, as a function of the vertical distributed load amplitude, as shown on the left in figure 2.9, through the expressions

$$\begin{aligned}
\begin{bmatrix}u(r)\\v(r)\\w(r)\end{bmatrix} &= r_e\pi i\sum_{k_P} H_1^{(2)}(k_Pr_e)\begin{bmatrix}F_{uz}J_1(k_Pr)/(\partial F_{uw}/\partial k_P)\\0\\F_{wz}J_0(k_Pr)/(\partial F_{uw}/\partial k_P)\end{bmatrix}p_z - \begin{bmatrix}0\\0\\F_{wz}(0)\end{bmatrix}p_z, \quad 0 < r \le r_e\\
&= r_e\pi i\sum_{k_P} J_1(k_Pr_e)\begin{bmatrix}F_{uz}H_1^{(2)}(k_Pr)/(\partial F_{uw}/\partial k_P)\\0\\F_{wz}H_0^{(2)}(k_Pr)/(\partial F_{uw}/\partial k_P)\end{bmatrix}p_z, \qquad r_e \le r
\end{aligned} \tag{2.43}$$

The displacements as a function of the horizontal distributed load amplitude, as shown on the right in figure 2.9, are expressed as

$$\begin{aligned}
\begin{bmatrix} u(r,\theta) \\ v(r,\theta) \\ w(r,\theta) \end{bmatrix} &= r_e \pi i \mathbf{D}(\theta) \sum_{k_P} H_1^{(2)}(k_P r_e) \begin{bmatrix} F_{ux}(J_0(k_P r) - J_1(k_P r)/k_P r)/(\partial F_{uw}/\partial k_P) \\ F_{ux} J_1(k_P r)/(k_P r \partial F_{uw}/\partial k_P) \\ -F_{wx} J_1(k_P r)/(\partial F_{uw}/\partial k_P) \end{bmatrix} p_x \\
&+ r_e \pi i \mathbf{D}(\theta) \sum_{k_S} H_1^{(2)}(k_S r_e) \begin{bmatrix} F_{vx} J_1(k_S r)/(k_S r \partial F_v/\partial k_S) \\ F_{vx}(J_0(k_S r) - J_1(k_S r)/k_S r)/(\partial F_v/\partial k_S) \\ 0 \end{bmatrix} p_x \\
&- \frac{1}{2} \mathbf{D}(\theta) \begin{bmatrix} F_{ux}(0) + F_{vx}(0) \\ F_{ux}(0) + F_{vx}(0) \\ 0 \end{bmatrix} p_x, \qquad 0 < r \leq r_e \\
&= r_e \pi i \mathbf{D}(\theta) \sum_{k_P} J_1(k_P r_e) \begin{bmatrix} F_{ux}(H_0^{(2)}(k_P r) - H_1^{(2)}(k_P r)/k_P r)/(\partial F_{uw}/\partial k_P) \\ F_{ux} H_1^{(2)}(k_P r)/(k_P r \partial F_{uw}/\partial k_P) \\ -F_{wx} H_1^{(2)}(k_P r)/(\partial F_{uw}/\partial k_P) \end{bmatrix} p_x \\
&+ r_e \pi i \mathbf{D}(\theta) \sum_{k_S} J_1(k_S r_e) \begin{bmatrix} F_{vx} H_1^{(2)}(k_S r)/(k_S r \partial F_v/\partial k_S) \\ F_{vx}(H_0^{(2)}(k_S r) - H_1^{(2)}(k_S r)/k_S r)/(\partial F_v/\partial k_S) \\ 0 \end{bmatrix} p_x \\
&- \frac{r_e^2}{r^2} \mathbf{D}(\theta) \begin{bmatrix} F_{vx}(0) - F_{ux}(0) \\ F_{ux}(0) - F_{vx}(0) \\ 0 \end{bmatrix} p_x, \qquad r_e \leq r
\end{aligned} \tag{2.44}$$

The amplitudes of the loads acting in horizontal and vertical directions are p_x and p_z, respectively, and the radius of the element on which the loads act is r_e. The functions J_0 and J_1 are Bessel functions of the first kind of orders 0 and 1, and $H_0^{(2)}$ and $H_1^{(2)}$ are Hankel functions of orders 0 and 1. They represent the shapes of the modes included and also originate from the transformation of the load shape to the wavenumber domain.
The matrix $\mathbf{D}(\theta)$ is a diagonal matrix to consider the variation of the response amplitude over the circumferential coordinate. It has the entries $[\cos(\theta), -\sin(\theta), \cos(\theta)]$ for a load in x-direction and the entries $[\sin(\theta), \cos(\theta), \sin(\theta)]$ for a load in y-direction. This matrix is only present in the response to the horizontal load, as the vertical load produces an axisymmetric response.
The flexibility of the soil is represented by the following flexibility functions:

$$\begin{aligned}
F_{ux} &= \sin(hk(s+t))st - \sin(hk(s-t))st + \sin(hk(s+t)) + \sin(hk(s-t)))(t^2+1)t \\
F_{uz} &= F_{wx} = (-1 - st^3 + (-2s^2+1)t^2 + 3st)\cos(hk(s-t)) \\
&\quad + (1 - st^3 + (2s^2-1)t^2 + 3st)\cos(hk(s+t)) + 2st(t^2-3) \\
F_{wz} &= (\sin(hk(s+t))st + \sin(hk(s-t))st + \sin(hk(s+t)) - \sin(hk(s-t)))(t^2+1)s \\
F_{uw} &= ((-t^4 + 4st + 2t^2 - 1)(st-1)\cos(hk(s-t)) \\
&\quad - (t^4 + 4st - 2t^2 + 1)(st+1)\cos(hk(s+t)) - 8st^3 + 8st)kG \\
F_{vx} &= \sin(kth) \\
F_v &= ktG\cos(kth)
\end{aligned} \tag{2.45}$$

The parameter h represents the thickness of the soil layer, and s and t are expressed as

$$\begin{aligned} s &= -i\sqrt{1-\frac{1}{l_x^2}} \quad \text{with} \quad l_x = \frac{c_p}{c} \quad \text{and} \quad c_p = \sqrt{\frac{\lambda_s + 2G_s}{\rho_s}} \\ t &= -i\sqrt{1-\frac{1}{m_x^2}} \quad \text{with} \quad m_x = \frac{c_s}{c} \quad \text{and} \quad c_s = \sqrt{\frac{G_s}{\rho_s}} \end{aligned} \tag{2.46}$$

in which ρ_s is the soil density, c_s is the shear wave velocity, c_p is the compressional wave velocity, and $c = \omega/k$. The flexibility functions are thus dependent on the material and geometrical properties of the soil layer, and the frequency of excitation with the related wavenumbers.

2.4.2 Soil-structure interface discretization

In order to produce a stiffness matrix that can be applied in the equations of motion of the tank's bottom plate, the soil-structure interface needs to be discretized into circular elements. Although discretizing a circle into smaller circles will lead to some overlap of the elements, this should have a negligible effect if the elements are small and the location of the elements and their radii are determined such that the area and the second moment of area remain the same as those of the undiscretized interface. In that case, the force equilibria are not violated and the stress distributions approximate the original one.
The method of discretization here is as follows. First, the interface is split into parts of equal degrees along the circumferential direction and increasing size along the radial direction in order to obtain parts that are not too slender (see figure 2.10). Then circles are fitted to the resulting parts with the same area and second moment of area with respect to the center of the soil-structure interface. The radius of the element is determined through

$$\int_{\theta=0}^{2\pi/n_\theta} \int_{r_i}^{r_{i+1}} r \mathrm{d}r\mathrm{d}\theta = \pi r_e^2 = A_e \qquad \rightarrow \qquad r_e = \sqrt{\frac{r_{i+1}^2 - r_i^2}{n_\theta}} \tag{2.47}$$

in which n_θ is the number of segments in circumferential direction, r_i is the smaller radial boundary of a part and r_{i+1} the larger radial boundary of a part. The distance of the center of each element to the center of the interface is calculated with

$$\int_{\theta=0}^{2\pi/n_\theta} \int_{r_i}^{r_{i+1}} r^3 \mathrm{d}r\mathrm{d}\theta = \frac{\pi}{2} r_e^4 = I_e \qquad \rightarrow \qquad r = \sqrt{\frac{r_{i+1}^2 - r_i^4}{2n_\theta r_e^2} - \frac{r_e^2}{2}} \tag{2.48}$$

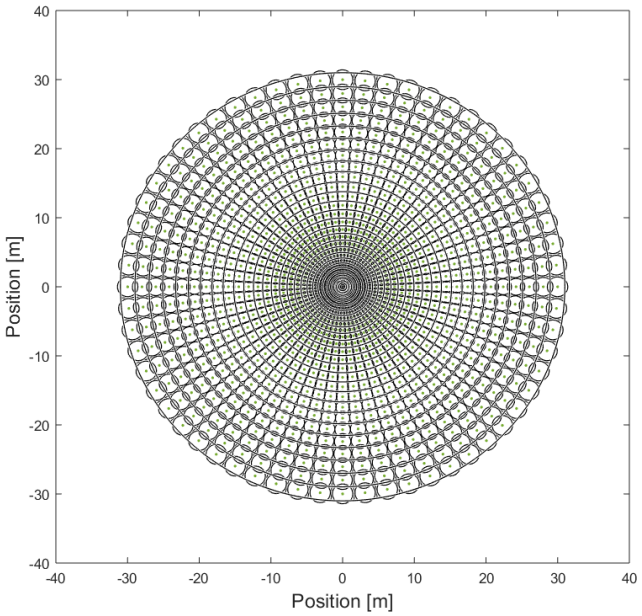

Figure 2.10 – *Discretization of soil-structure interface*

To determine the required number of elements, a convergence criterium needs to be applied, which is discussed in more detail in section 3.2.
Please note that this discretization is also applied to the plate's mode shapes, so that the dynamic stiffness matrix can be applied in the plate's equations of motion. This means that the displacement functions $\tilde{\mathbf{u}}_p(r,\theta,\omega)$ and $\tilde{\mathbf{u}}_i(r,\theta,\omega)$ in equation (2.4) need to be evaluated at the locations of the center of the circular elements of the discretization.

2.4.3 Matrix assembly

To find the entries of the stiffness matrix, first, the displacements from equations (2.43) and (2.44) are described in the global Cartesian coordinate system:

$$\begin{bmatrix} u_x \\ u_y \\ u_z \end{bmatrix} = \begin{bmatrix} \cos(\theta_e) & -\sin(\theta_e) & 0 \\ \sin(\theta_e) & \cos(\theta_e) & 0 \\ 0 & 0 & 1 \end{bmatrix} \begin{bmatrix} u \\ v \\ w \end{bmatrix} \tag{2.49}$$

in which θ_e is the element's local circumferential coordinate. To apply the stiffness matrix in the equations of motion of the tank's bottom plate, defined in cylindrical coordinates, an additional transformation is needed. The operation can be performed by making use of rotation matrices based on the circumferential coordinate of each element with respect to the global coordinate system. In the latter, $\theta = 0$ coincides with the x-axis. A force at location i in the Cartesian coordinate system is related to the cylindrical coordinate system through

$$\mathbf{f}_{i,Cart} = \begin{bmatrix} \cos(\theta_i) & -\sin(\theta_i) & 0 \\ \sin(\theta_i) & \cos(\theta_i) & 0 \\ 0 & 0 & 1 \end{bmatrix} \mathbf{f}_{i,cyl} = \mathbf{R}_i \mathbf{f}_{i,cyl} \tag{2.50}$$

in which θ_i is the angle between location i and the x-axis with the origin of the coordinate system at the center of the plate. A similar relation holds for displacements at location j:

$$\mathbf{u}_{j,Cart} = \begin{bmatrix} \cos(\theta_j) & -\sin(\theta_j) & 0 \\ \sin(\theta_j) & \cos(\theta_j) & 0 \\ 0 & 0 & 1 \end{bmatrix} \mathbf{u}_{j,cyl} = \mathbf{R}_j \mathbf{u}_{j,cyl} \tag{2.51}$$

The relation between a force at location i and displacements at location j can then be given by

$$\mathbf{u}_{j,Cart} = \begin{bmatrix} R_{xx} & R_{xy} & R_{xz} \\ R_{yx} & R_{yy} & R_{yz} \\ R_{zx} & R_{zy} & R_{zz} \end{bmatrix} \mathbf{f}_{i,Cart} = \mathbf{R}_{Cart} \mathbf{f}_{i,Cart} \tag{2.52}$$

in which the elements of $\mathbf{R}_{Cart}$ contain the Green's functions from equations (2.43) and (2.44). Finally, the stresses at location i due to a displacement in j can be found as

$$\mathbf{f}_{i,cyl} = \mathbf{R}_i^T \mathbf{R}_{Cart}^{-1} \mathbf{R}_j \mathbf{u}_{j,cyl} = \mathbf{K}_{cyl} \mathbf{u}_{j,cyl} \tag{2.53}$$

in which use is made of the identity $\mathbf{R}_i^{-1} = \mathbf{R}_i^T$ that originates from the orthogonality of $\mathbf{R}_i$. By assembling the matrices $\mathbf{K}_{cyl}$ for all elements, the complete dynamic stiffness matrix is formed.

2.4.4 Excitation

The excitation of the system during a seismic event stems from accelerations of the soil, which are transferred to the structure through stresses acting on the soil-structure interface. Generally, measurements of such accelerations are available for the free-field response, so it would be beneficial to be able to apply such measured signals directly in the model. At the same time, the description of the excitation of the system in the model needs to incorporate both kinematic and dynamic soil structure interaction.
At the interface between the soil and the structure, interface conditions hold. It is assumed that the soil and structure are connected monolithically, meaning that there is a continuity of displacements and stresses, expressed mathematically as

$$\begin{aligned} \mathbf{u}_p &= \mathbf{u}_s \\ \boldsymbol{\sigma}_p &= \boldsymbol{\sigma}_s \end{aligned} \tag{2.54}$$

in which the displacements of the soil and the plate at the interface are $\mathbf{u}_s = [u_{s;r}, u_{s;\theta}, u_{s;z}]^T$ and $\mathbf{u}_p = [u_{p;r}, u_{p;\theta}, u_{p;z}]^T$, respectively. The stresses $\boldsymbol{\sigma}_s = [\sigma_{s;zr}, \sigma_{s;z\theta}, \sigma_{s;zz}]^T$ are the soil stresses acting on the surface normal to the z-coordinate and $\boldsymbol{\sigma}_p = [\sigma_{p;zr}, \sigma_{p;z\theta}, \sigma_{p;zz}]^T$ are the plate stresses on the surface normal to the z-coordinate. Note that the stress continuity condition is satisfied in the plate's equation of motion.
As introduced in section 1.1.2, the dynamic SSI is mainly concerned with stresses originating from the motions and inertia of the plate, causing a radiated wave field, whereas the kinematic SSI is concerned with the alteration of the free-field waves by the addition of a scattered wave field resulting from the presence of a structure. Due to the linearity of the model, the total motions of the soil can be regarded as the superposition of these two cases:

$$\mathbf{u}_s = \mathbf{u}_r + \mathbf{u}_i + \mathbf{u}_{sc} \tag{2.55}$$

in which $\mathbf{u}_r$ is the radiated wave field, $\mathbf{u}_i$ is the free-field wave field and $\mathbf{u}_{sc}$ is the scattered wave field. Substitution of equation (2.55) into the displacement continuity condition in equation (2.54) yields

$$\mathbf{u}_p = \mathbf{u}_r + \mathbf{u}_i + \mathbf{u}_{sc} \tag{2.56}$$

which can be rewritten as

$$\mathbf{u}_p - \mathbf{u}_i = \mathbf{u}_r + \mathbf{u}_{sc} \tag{2.57}$$

The soil stresses acting on the plate, $\boldsymbol{\sigma}_s$, can be expressed with use of the dynamic stiffness matrix as defined in the previous sections through

$$\boldsymbol{\sigma}_s = \mathbf{K}_s\mathbf{u}_r + \mathbf{K}_s\mathbf{u}_i + \mathbf{K}_s\mathbf{u}_{sc} \tag{2.58}$$

Realizing that the free-field displacement field by definition produces zero stresses at the soil surface, the second term in the right-hand side of equation (2.58) disappears, so that

$$\boldsymbol{\sigma}_s = \mathbf{K}_s\left(\mathbf{u}_r + \mathbf{u}_{sc}\right) \tag{2.59}$$

Substituting equation (2.57) into equation (2.59) results in

$$\boldsymbol{\sigma}_s = \mathbf{K}_s\left(\mathbf{u}_p - \mathbf{u}_i\right) \tag{2.60}$$

As such, the soil stresses are conveniently expressed in terms of a generally known free-field displacement field and the unknown displacements of the plate that the plate's equations of motion will be solved for. Both dynamic and kinematic soil-structure interaction are thus accounted for. For application in equation (2.3) on the right-hand side, the sign of equation (2.60) needs to reflect that positive motions of the plate generate stresses from the soil that act in the opposite direction.
Finally, the excitation is usually given as an acceleration signal with components in Cartesian coordinates, which can be transformed to a frequency spectrum with equation (2.1). The displacement field can then be given as

$$\begin{bmatrix}\tilde{u}_{i;r}(r,\theta,\omega)\\ \tilde{u}_{i;\theta}(r,\theta,\omega)\\ \tilde{u}_{i;z}(r,\theta,\omega)\end{bmatrix} = -\frac{1}{\omega^2}\begin{bmatrix}\cos(\theta) & -\sin(\theta) & 0\\ \sin(\theta) & \cos(\theta) & 0\\ 0 & 0 & 1\end{bmatrix}\begin{bmatrix}\tilde{a}_x(\omega)P_x(r,\theta,\omega)\\ \tilde{a}_y(\omega)P_y(r,\theta,\omega)\\ \tilde{a}_z(\omega)P_z(r,\theta,\omega)\end{bmatrix} \tag{2.61}$$

in which the x-direction coincides with $\theta = 0$. The functions P_x, P_y and P_z are shape functions that describe the distribution of the accelerations at each frequency across the soil-structure interface. In case of a Rayleigh-type surface wave, for example, they would be $P_x = P_y = P_z = \exp(-ir\cos(\theta)\omega/c_R)$, while they are $P_x = P_y = P_z = 1$ for uniform accelerations in each direction.

2.4.5 Damping

A system is damped if energy is dissipated from it over time. In the system at hand, damping can stem from material damping in the tank, from the sloshing of the fluid, from the soil material damping and the radiation damping. It is generally assumed that the soil damping is relatively large compared to the damping from the tank-fluid system itself, which is reflected in the maximum values allowed by the Eurocode for each type of damping. These are 5%, 0.5% and 25% for the structure, fluid and soil respectively (EN 1998-4 (2007)). Currently, in the model only material damping of the tank and soil, and radiation damping

are incorporated.
To obtain a measure of the damping caused by the soil, it is proposed in this thesis to evaluate the amount of dissipated energy as a percentage of the total energy in the system at a given frequency over the time duration of one period.
The amount of energy that is dissipated over one period can be determined with the imaginary part of the complex valued dynamic soil stiffness matrix (Gazetas (1983); Molenkamp (2018)), that represents the damping part of the soil. When the tank is in motion, each element of the discretized soil-structure interface can experience displacements resulting from the plate's displacements and generates damping forces through the imaginary part of the soil stiffness matrix. By evaluating the amount of dissipated energy for each element and summing over all elements, the total amount of dissipated energy can be found.
In general, the energy dissipated by a viscous damper can be expressed as

$$\Delta W = \int F_c \mathrm{d}u \tag{2.62}$$

Realizing that the velocity is the time derivative of the displacement, $v = \mathrm{d}u/\mathrm{d}t$, we can write that $\mathrm{d}u = v\mathrm{d}t$. The amount of dissipated energy over time is then

$$\Delta W = \int F_c v \mathrm{d}t \tag{2.63}$$

in which $T = 2\pi/\omega$. Radiation damping occurs when soil waves carry energy away from the fluid-tank system. In order for these waves to be generated, the bottom plate of the tank must move relative to the motions that the soil would experience without the presence of the tank. This difference, which was also applied in the equations of motion of the bottom plate of the tank, is expressed as

$$\tilde{\mathbf{u}}_\Delta(r,\theta,\omega) = \tilde{\mathbf{u}}_i(r,\theta,\omega) - \tilde{\mathbf{u}}_p(r,\theta,\omega) \tag{2.64}$$

The damping force can thus be calculated by

$$\tilde{\mathbf{F}}_c(r,\theta,\omega) = \mathrm{i}\,\mathrm{Im}\left(\mathbf{K}_s(r,\theta,\omega)\right)\ \tilde{\mathbf{u}}_\Delta(r,\theta,\omega) \tag{2.65}$$

Considering equation (2.63), to obtain the amount of dissipated energy, the velocity needs to be known, which can be expressed in the frequency domain as

$$\tilde{\mathbf{v}}_\Delta(r,\theta,\omega) = \mathrm{i}\omega\tilde{\mathbf{u}}_\Delta(r,\theta,\omega) \tag{2.66}$$

To obtain the total amount of energy dissipated through the soil over a duration of time in the time domain, $\tilde{\mathbf{F}}_c(\omega)\tilde{\mathbf{v}}_\Delta(\omega)$ can first be transformed to the time domain with the inverse Fourier transform (equation (2.1)). The resulting value $F_c v$ can then be applied in equation (2.63) for given time limits of integration. As such, the total amount of energy dissipated through the soil can be computed for an earthquake event.
It is also possible to compute the amount of dissipated energy at each frequency over one period. In that case equation (2.63) can be evaluated to

$$\Delta W = \int_0^{\omega/2\pi} \mathrm{i}\omega|\tilde{\mathbf{u}}_\Delta(r,\theta,\omega)|\ \mathrm{i}\,\mathrm{Im}\left(\mathbf{K}_s(r,\theta,\omega)\right)\ |\tilde{\mathbf{u}}_\Delta(r,\theta,\omega)|\mathrm{d}t \tag{2.67}$$

in which the phase of $\tilde{\mathbf{u}}_\Delta(r,\theta,\omega)$ is discarded by taking its absolute value, which is allowed, because the damping will be determined over one period. Transforming the terms in the

integral to the time domain, evaluating the integral and transforming the result back to the frequency domain, yields the dot product

$$\Delta W = \pi \left|\tilde{\mathbf{u}}_\Delta(r,\theta,\omega)\right| \operatorname{Im}\left(\mathbf{K}_s(r,\theta,\omega)\right) \left|\tilde{\mathbf{u}}_\Delta(r,\theta,\omega)\right| \tag{2.68}$$

Then the total amount of energy present in the tank-fluid system needs to be determined. The motions of the tank are expressed as a summation of vibration modes, each containing an amount of energy that is the sum of the kinetic energy and the strain energy. Over the course of one period, the strain energy will attain a maximum value as the displacements reach a maximum. At this specific point in time, the velocity will be zero. On the other hand, realizing that the vibrations are harmonic in time, at each location in the tank, the stresses will be zero at some moment during the time span of a period, so that the strain energy at that location is then zero.
The velocity at that moment attains a maximum value, so that the total energy at that location at that moment in time is equal to the kinetic energy. The fluid on the other hand is assumed to be incompressible and can therefore not contain any strain energy. Its total energy is therefore also evaluated on the basis of the kinetic energy.

$$W_{\text{tank}} = W_w + W_p \tag{2.69}$$

$$\mathrm{d}m_w = \rho_w h_w R \mathrm{d}\theta \mathrm{d}z \tag{2.70}$$

$$\mathrm{d}W_w = \frac{1}{2}\mathrm{d}m_w v_w^2 = \frac{1}{2}\rho_w h_w R \left[\mathrm{i}\omega\tilde{\mathbf{u}}_w(r,\theta,\omega)\right]^2 \mathrm{d}\theta\mathrm{d}z \tag{2.71}$$

$$W_w = \int \mathrm{d}W_w = \int_{z=0}^{H}\int_{\theta=0}^{2\pi} \frac{1}{2}\rho_w h_w R \left[\mathrm{i}\omega\tilde{\mathbf{u}}_w(r,\theta,\omega)\right]^2 \mathrm{d}\theta\mathrm{d}z \tag{2.72}$$

with

$$\tilde{\mathbf{u}}_w(r,\theta,\omega) = \sum_{m=1}^{\infty}\sum_{n=0}^{\infty} \tilde{X}_{mn}(\omega)\tilde{\mathbf{U}}_{w;mn}(r,\theta) \tag{2.73}$$

$$\mathrm{d}m_p = \rho_p h_p r \mathrm{d}\theta \mathrm{d}r \tag{2.74}$$

$$\mathrm{d}W_p = \frac{1}{2}\mathrm{d}m_p v_p^2 = \frac{1}{2}\rho_p h_p r \left[\mathrm{i}\omega\tilde{\mathbf{u}}_p(r,\theta,\omega)\right]^2 \mathrm{d}\theta\mathrm{d}r \tag{2.75}$$

$$W_p = \int \mathrm{d}W_p = \int_{z=0}^{R}\int_{\theta=0}^{2\pi} \frac{1}{2}\rho_p h_p r \left[\mathrm{i}\omega\tilde{\mathbf{u}}_p(r,\theta,\omega)\right]^2 \mathrm{d}\theta\mathrm{d}r \tag{2.76}$$

with

$$\tilde{\mathbf{u}}_p(r,\theta,\omega) = \sum_{m=1}^{\infty}\sum_{n=0}^{\infty} \tilde{X}_{mn}(\omega)\tilde{\mathbf{U}}_{p;mn}(r,\theta) \tag{2.77}$$

For the fluid, we have for an infinitesimal fluid volume of dimensions $r\mathrm{d}\theta$ x $\mathrm{d}r$ x $\mathrm{d}z$ a total kinetic energy of

$$\mathrm{d}W_{fl} = \frac{1}{2}\mathrm{d}m_{fl} v_{fl}^2 = \frac{1}{2}\rho_{fl}\left(\nabla\tilde{\phi}(r,\theta,z,\omega)\right)^2 r\mathrm{d}\theta\mathrm{d}r\mathrm{d}z \tag{2.78}$$

in which equation (2.26) is substituted, which gives the velocity of the fluid in terms of its velocity potential. The total kinetic energy of the fluid is then found by integrating over the entire fluid domain:

$$W_{fl} = \int \mathrm{d}W_{fl} = \int_{z=0}^{H_{fl}}\int_{r=0}^{R}\int_{\theta=0}^{2\pi} \frac{1}{2}\rho_{fl}\left(\nabla\tilde{\phi}(r,\theta,z,\omega)\right)^2 r\mathrm{d}\theta\mathrm{d}r\mathrm{d}z \tag{2.79}$$

Evaluation of the fluid velocity term with the use of equations (2.32) and (2.33) in the frequency domain gives

$$\begin{aligned}\tilde{\mathbf{v}}_{fl}(r,\theta,z,\omega) &= \nabla\tilde{\phi_1}(r,\theta,z,\omega) + \nabla\tilde{\phi_2}(r,\theta,z,\omega) + \nabla\tilde{\phi_3}(r,\theta,z,\omega) \\ &= \sum_{n=0}^{\infty}\sum_{a=1}^{\infty}\tilde{P}_{na}(\omega)\nabla\tilde{\Phi}^1_{na} + \sum_{n=0}^{\infty}\sum_{b=1}^{\infty}\tilde{Q}_{nb}(\omega)\nabla\tilde{\Phi}^2_{nb} + \sum_{n=0}^{\infty}\sum_{c=1}^{\infty}\tilde{S}_{nc}(\omega)\nabla\tilde{\Phi}^3_{nc}\end{aligned} \tag{2.80}$$

The amplitudes are known, as are the velocity shape functions that they need to be multiplied with, so the velocity can be found at each location of interest. The related fluid volume is computed numerically with $r\mathrm{d}\theta$ x $\mathrm{d}r$ x $\mathrm{d}z$. The contributions of each fluid volume are finally added up to give the total kinetic energy of the fluid.

2.5 System of equations

The total number of equations that need to be solved is equal to the number of modes considered. First, the equations governing the vibrations in each degree of freedom of the tank (three for the plate and three for the wall) are written in terms of modal expressions. Then, as all modes for the different degrees of freedom of the tank are related to each other, their equations can simply be added up. As such, the number of equations related to the tank's modes of vibrations equal the number of considered tank modes.
Then the equations that consider the interface conditions between the fluid and tank and the boundary condition at the fluid's free surface are presented, both in terms of modal expressions. This number of equations equals the number of considered fluid modes.
Finally, the system of equations that needs to be solved to find the modal amplitudes is presented.

2.5.1 Tank - general

For every mode of vibration of the tank, it holds that

$$\mathbf{L}\mathbf{u}_{nm} - \omega^2_{nm}\mathbf{I}\mathbf{u}_{nm} = 0 \tag{2.81}$$

as the modes are the solution to the eigenvalue problem as presented in section A. Substituting the modal expressions found previously into the equations of motion that for all parts of the tank are of the form

$$\mathbf{L}\mathbf{u} - \omega^2\mathbf{I}\mathbf{u} = \mathbf{q} \tag{2.82}$$

results in

$$\sum_{n=0}^{\infty}\sum_{m=1}^{\infty}\Big(\mathbf{L}\mathbf{u}_{nm} - \omega^2\mathbf{I}\mathbf{u}_{nm}\Big) = \sum_{n=0}^{\infty}\sum_{m=1}^{\infty}\mathbf{q}_{nm} \tag{2.83}$$

Rearrangement of equation (2.81) gives

$$\mathbf{L}\mathbf{u}_{nm} = \omega^2_{nm}\mathbf{I}\mathbf{u}_{nm} \tag{2.84}$$

which can be substituted into equation (2.83), to yield

$$\sum_{n=0}^{\infty}\sum_{m=1}^{\infty}(\omega^2_{nm} - \omega^2)\mathbf{I}\mathbf{u}_{nm} = \sum_{n=0}^{\infty}\sum_{m=1}^{\infty}\mathbf{q}_{nm} \tag{2.85}$$

thereby eliminating stiffness matrix $\mathbf{L}$.

2.5.2 Bottom plate

Substitution of equation (2.84) in the equations of motion of the plate (equation (2.4)) gives

$$\left(\omega_{nm}^2 - \omega^2\right) \mathbf{I}\tilde{\mathbf{u}}_{p;nm}(r,\theta,\omega) = \mathbf{K}_s(\omega)\left(\tilde{\mathbf{u}}_i(r,\theta,\omega) - \tilde{\mathbf{u}}_{p;nm}(r,\theta,\omega)\right) + \tilde{\mathbf{q}}_{fl;nm} \tag{2.86}$$

Taking the term related to the unknown plate displacements $\tilde{\mathbf{u}}_{p;nm}(r,\theta,\omega)$ to the left hand side and substituting the modal expressions (equation (2.21)) into the equations of motion (equation (2.86)) gives

$$\begin{aligned}
&\sum_{n=0}^{\infty}\sum_{m=0}^{\infty}(\omega_{nm}^2-\omega^2)\rho_p h_p \tilde{X}_{nm}(\omega)\tilde{\mathbf{U}}_{p;mn}(r,\theta) + \mathbf{K}_s(\omega)\sum_{n=0}^{\infty}\sum_{m=0}^{\infty}\tilde{X}_{nm}(\omega)\tilde{\mathbf{U}}_{p;mn}(r,\theta) \\
&\qquad = \mathbf{K}_s(\omega)\begin{bmatrix}\tilde{u}_{i,z}(r,\theta,\omega)\\ \tilde{u}_{i,\theta}(r,\theta,\omega)\\ \tilde{u}_{i,r}(r,\theta,\omega)\end{bmatrix} \\
-\mathrm{i}\omega\rho_{fl}\,\mathbf{r}\sum_{n=0}^{\infty}&\left\{\sum_{a=0}^{\infty}\tilde{P}_{na}(\omega)\tilde{\Phi}_{na}^1(r,\theta,z) + \sum_{b=0}^{\infty}Q_{nb}(\omega)\tilde{\Phi}_{nb}^2(r,\theta,z) + \sum_{c=0}^{\infty}S_{nc}(\omega)\tilde{\Phi}_{nc}^3(r,\theta,z)\right\}\Bigg|_{z=0}
\end{aligned} \tag{2.87}$$

with $\mathbf{K}_s$ as shown in equation (2.5), $\tilde{\mathbf{U}}_{p;mn}(r,\theta)$ as shown in equation (2.22), $\tilde{\Phi}_{na}^1(r,\theta,z)$, $\tilde{\Phi}_{na}^1(r,\theta,z)$, and $\tilde{\Phi}_{na}^1(r,\theta,z)$ as shown in equation (2.33), and $\mathbf{r} = [0,0,1]^T$. Application of the orthogonality property of the trigonometric functions, multiplication with each coordinate's respective axial mode shape and integration over the radius, and finally, addition of the three equations of motion yields:

$$\begin{aligned}
&\sum_{m=0}^{\infty}(\omega_{nm}^2-\omega^2)\rho_p h_p \tilde{X}_{nm}\int_{r=0}^{R}\tilde{\mathbf{U}}_{p;mn}^{*T}(r)\tilde{\mathbf{U}}_{p;mn}^{*}(r)\mathrm{d}r \\
&\quad + \sum_{m=0}^{\infty}\tilde{X}_{nm}\int_{r=0}^{R}\tilde{\mathbf{U}}_{p;mn}^{*T}(r)\int_{\theta=0}^{2\pi}\hat{\mathbf{K}}_s\mathrm{d}\theta\tilde{\mathbf{U}}_{p;mn}^{*}(r)\mathrm{d}r \\
&= \frac{1}{\pi(1+\delta_{n0})}\int_{r=0}^{R}\int_{\theta=0}^{2\pi}\tilde{\mathbf{U}}_{p;mn}^{T}(r,\theta)\mathbf{K}_s\tilde{\mathbf{u}}_i(r,\theta,\omega)\mathrm{d}\theta\mathrm{d}r \\
-\frac{\mathrm{i}\omega\rho_{fl}}{\cos(n\theta)}&\int_{r=0}^{R}\left\{\sum_{a=0}^{\infty}\tilde{P}_{na}\tilde{\Phi}_{na}^1(r,\theta,0) + \sum_{b=0}^{\infty}Q_{nb}\tilde{\Phi}_{nb}^2(r,\theta,0) + \sum_{c=0}^{\infty}S_{nc}\tilde{\Phi}_{nc}^3(r,\theta,0)\right\}\tilde{U}_{p;znm}(r)\mathrm{d}r
\end{aligned} \tag{2.88}$$

with

$$\hat{\mathbf{K}}_s = \begin{bmatrix}K_{rr} & 0 & K_{rz}\\ 0 & K_{\theta\theta} & 0\\ K_{zr} & 0 & K_{zz}\end{bmatrix} \tag{2.89}$$

which contains zeros to account for the elimination of some terms due to the orthogonality properties of the trigonometric functions. The vector

$$\tilde{\mathbf{U}}_{p;mn}^{*}(r) = \begin{bmatrix}\tilde{U}_{p;rnm}(r)\\ \tilde{U}_{p;\theta nm}(r)\\ \tilde{U}_{p;znm}(r)\end{bmatrix}$$

is not to be confused with $\tilde{\mathbf{U}}_{p;mn}(r,\theta)$ as defined in equation (2.22). Vector $\tilde{\mathbf{u}}_i(r,\theta,\omega) = [\tilde{u}_{i;r}, \tilde{u}_{i;\theta}, \tilde{u}_{i;z}]$ represents the incident wave field. The division of the first term on the right-hand side by $\pi(1-\delta_{0n})$ accounts for the result of the integration in the application of the orthogonality property of the trigonometric functions, which yields 2π for $n=0$ and π for $n \geq 1$. The Kronecker delta δ_{ij} evaluates to zero for $i \neq j$ and to one for $i = j$. The addition of the three equations of motion is required to be able to apply the orthogonality condition of the mode shapes, given in equation (2.25).
A more detailed treatment of the steps taken to obtain equation (2.88) from equation (2.87) can be found in section C.1.

2.5.3 Wall

Substitution of equation (2.81) in the equations of motion of the wall (equation (2.9)) gives

$$\left(\omega_{nm}^2 - \omega^2\right) \mathbf{I}\tilde{\mathbf{u}}_{w;nm}(z,\theta,\omega) = \tilde{\mathbf{q}}_{fl;nm} \tag{2.90}$$

Substitution of the modal expressions (equation (2.23)) in the equations of motion (equation (2.90)) gives

$$\sum_{n=0}^{\infty}\sum_{m=0}^{\infty}(\omega_{nm}^2-\omega^2)\rho_w h_w \tilde{X}_{nm}(\omega)\tilde{\mathbf{U}}_{w;mn}(z,\theta) =$$
$$-\mathrm{i}\omega\rho_{fl}\,\mathbf{r}\sum_{n=0}^{\infty}\left\{\sum_{a=0}^{\infty}\tilde{P}_{na}(\omega)\tilde{\Phi}^1_{na}(R,\theta,z)+\sum_{b=0}^{\infty}\tilde{Q}_{nb}(\omega)\tilde{\Phi}^2_{nb}(R,\theta,z)+\sum_{c=0}^{\infty}\tilde{S}_{nc}(\omega)\tilde{\Phi}^3_{nc}(R,\theta,z)\right\} \tag{2.91}$$

with $\tilde{\mathbf{U}}_{w;mn}(z,\theta)$ is defined in equation (2.24) and $\mathbf{r} = [0,0,1]^T$.
Application of the orthogonality property of the trigonometric functions, multiplication with each coordinate's respective axial mode shape and integration over the height, and finally, addition of the three equations of motion yields:

$$\sum_{m=0}^{\infty}(\omega_{nm}^2-\omega^2)\rho_p h_p \tilde{X}_{nm}\int_{z=0}^{H}\tilde{\mathbf{U}}^{*T}_{w;mn}(z)\tilde{\mathbf{U}}^{*}_{w;mn}(z)\mathrm{d}z =$$
$$-\frac{\mathrm{i}\omega\rho_{fl}}{\cos(n\theta)}\int_{z=0}^{H_{fl}}\left\{\sum_{a=0}^{\infty}\tilde{P}_{na}\tilde{\Phi}^1_{na}(R,\theta,z)+\sum_{b=0}^{\infty}Q_{nb}\tilde{\Phi}^2_{nb}(R,\theta,z)+\sum_{c=0}^{\infty}S_{nc}\tilde{\Phi}^3_{nc}(R,\theta,z)\right\}\tilde{U}_{w;rnm}(z)\mathrm{d}z \tag{2.92}$$

The vector

$$\tilde{\mathbf{U}}^{*}_{w;mn}(z) = \begin{bmatrix}\tilde{U}_{w;znm}(z)\\ \tilde{U}_{w;\theta nm}(z)\\ \tilde{U}_{w;rnm}(z)\end{bmatrix}$$

is not to be confused with $\tilde{\mathbf{U}}_{w;mn}(z,\theta)$ as defined in equation (2.24). A more detailed treatment of the steps taken to obtain equation (2.92) from equation (2.91) can be found in section C.2.

2.5.4 Kinematic conditions

At the interface between the fluid and the tank, interface conditions apply. The kinematic conditions are the velocity continuity at the tank wall:

$$\left.\frac{\partial\phi(r,\theta,z,t)}{\partial r}\right|_{r=R} = \frac{\partial u_{w;r}(z,\theta,t)}{\partial t} \tag{2.93}$$

the velocity continuity at the plate bottom: Also transformation to the frequency domain.

$$\left.\frac{\partial\phi(r,\theta,z,t)}{\partial z}\right|_{z=0} = -\frac{\partial u_{p;z}(r,\theta,t)}{\partial t} \tag{2.94}$$

The free surface boundary condition:

$$\left.\frac{1}{g}\frac{\partial^2\phi(r,\theta,z,t)}{\partial t^2}\right|_{z=H_{fl}} = -\left.\frac{\partial\phi(r,\theta,z,t)}{\partial z}\right|_{z=H_{fl}} \tag{2.95}$$

Substitution of the modal expressions of the fluid velocity potentials and the tank's mode shapes results in

$$\left.\frac{\partial}{\partial r}\left(\sum_{n=0}^{\infty}\sum_{a=1}^{\infty}P_{na}\tilde{\Phi}^1_{na}(r,\theta,z)\right)\right|_{r=R} = \mathrm{i}\omega\sum_{n=0}^{\infty}\sum_{m=1}^{\infty}\tilde{X}_{nm}\tilde{U}_{w;rnm}(z)\cos(n\theta) \tag{2.96}$$

Multiplication of both sides with $\cos(q\theta)$ and integration from 0 to 2π, as well as multiplication of both sides with the z-dependent part of $\tilde{\Phi}^1_{na}(r,\theta,z)$ and integration of the fluid height eliminates the summation over n and the summation over a:

$$P_{na}\frac{\partial}{\partial r}\left[I_n\left(\frac{\pi(2a-1)r}{2H_l}\right)\right]\Bigg|_{r=R}\frac{H_l}{2}\delta_{ad} = \mathrm{i}\omega\int_{z=0}^{H_{fl}}\sum_{m=1}^{\infty}\tilde{X}_{nm}\tilde{U}_{w;rnm}(z)\cos\left(\frac{\pi(2a-1)z}{2H_l}\right)\mathrm{d}z \tag{2.97}$$

A more detailed treatment of the steps taken to arrive at equation (2.97) from equation (2.96) is given in section C.3.

For the second interface condition, concerning the velocity continuity at the plate, the modal expressions of the tank bottom displacement in z-direction and of the fluid potential (equations (2.21) and (2.32)) are substituted into equation (2.94), yielding

$$\left.\frac{\partial}{\partial z}\left(\sum_{n=0}^{\infty}\sum_{b=1}^{\infty}Q_{nb}\tilde{\Phi}^2_{nb}(r,\theta,z)\right)\right|_{z=0} = -\mathrm{i}\omega\sum_{n=0}^{\infty}\sum_{m=1}^{\infty}\tilde{X}_{nm}\tilde{U}_{p;znm}(r)\cos(n\theta) \tag{2.98}$$

Making use of the orthogonality properties of the trigonometric functions and the Bessel functions by multiplying both sides by $\cos(q\theta)$ and the r-dependent part of $\tilde{\Phi}^2_{nb}(r,\theta,z)$, and finally, integrating from 0 to 2π and over the radius results in

$$Q_{nb}\frac{\varepsilon_{nb}J_n(\varepsilon_{nb}r/R)}{2\tanh(\varepsilon_{nb}H_l/R)}\left[J_{n+1}(\varepsilon_{nb})\right]^2 = -\mathrm{i}\omega\int_{r=0}^{R}\sum_{m=0}^{\infty}\tilde{X}_{nm}\tilde{U}_{p;znm}(r)rJ_n(\varepsilon_{ne}r/R)\mathrm{d}r \tag{2.99}$$

in which the summation over n and over b are eliminated. A more detailed treatment of the steps taken to arrive at equation (2.99) from equation (2.98) is given in section C.4.
Finally, the modal expression of the fluid potential (equation (2.32)) is substituted into the free surface condition, equation (2.95), yielding

$$\frac{\omega^2}{g}\sum_{n=0}^{\infty}\sum_{c=0}^{\infty}S_{nc}\tilde{\Phi}^3_{nc}(r,\theta,z) = \frac{\partial}{\partial z}\left(\sum_{n=0}^{\infty}\sum_{a=0}^{\infty}P_{na}\tilde{\Phi}^1_{na}(r,\theta,z)+\sum_{n=0}^{\infty}\sum_{b=0}^{\infty}Q_{nb}\tilde{\Phi}^2_{nb}(r,\theta,z)+\sum_{n=0}^{\infty}\sum_{c=0}^{\infty}S_{nc}\tilde{\Phi}^3_{nc}(r,\theta,z)\right)\Bigg|_{z=H_{fl}} \tag{2.100}$$

Making use of the orthogonality properties of the trigonometric functions and the Bessel functions by multiplying both sides by $\cos(q\theta)$ and the r-dependent part of $\tilde{\Phi}^3_{nc}(r,\theta,z)$, and finally, integrating from 0 to 2π and over the radius results in

$$\begin{aligned}\frac{\omega^2}{2g}S_{nc}\cosh\left(\varepsilon_{nc}\frac{H_{fl}}{R}\right)\left[J_{n+1}(\varepsilon_{nc})\right]^2 &= S_{nc}\frac{\varepsilon_{nc}}{2R}\sinh(\varepsilon_{nc}H_{fl}/R)\left[J_{n+1}(\varepsilon_{nc})\right]^2\\ &+\int_{r=0}^{R}\sum_{a=0}^{\infty}P_{na}I_n\left(\frac{\pi(2a-1)r}{2H_l}\right)\left(\frac{\cos(\pi a)\pi(2a-1)}{2H_l}\right)rJ_n(\varepsilon_{nf}r/R)\mathrm{d}r\\ &+Q_{nb}\frac{\varepsilon_{nb}}{2R}\left(\sinh(\varepsilon_{nb}H_{fl}/R)-\frac{\cosh(\varepsilon_{nb}H_{fl}/R)}{\tanh(\varepsilon_{nb}H_{fl}/R)}\right)\left[J_{n+1}(\varepsilon_{nb})\right]^2\end{aligned} \tag{2.101}$$

in which the summation over n, over b, and over c are eliminated. A more detailed treatment of the steps taken to arrive at equation (2.100) from equation (2.101) is given in section C.5.

2.5.5 Final set of equations

By summing equations (C.7) to (C.9) and (C.16) to (C.18), the orthogonality relation can be used in equation (2.25). Together with equations (C.22), (C.27) and (C.31), they form the final set of equations to be solved, and can be written in the matrix equation

$$\mathbf{Gx} = \mathbf{f} \tag{2.102}$$

in which $\mathbf{G}$ contains the mode shapes, $\mathbf{x}$ contains the unknown modal amplitudes and $\mathbf{f}$ contains the systems loading components, which are related to the earthquake excitation.
In theory, an infinite number of modes should be considered. In practice, this is not possible, so in order to accurately solve for the displacements of interest, a proper truncation rule must be specified. In this case, the cut-off criterion is that an additional mode does not change the results by more than 1%. This criterion is also applied to the discretization of the soil, in that an additional ring or angular segment of elements does not change the results by more than 1%.

3 Case study

This section treats two topics. The first is the convergence of the solution and the adoption of criteria for the truncation of the number of modes and the number of soil-structure interface elements. The second is the dynamic response of the tank-fluid-soil system to a realistic ground motion.

3.1 Case description

For the case study, a scenario is examined of a medium-sized tank in the area of Groningen, the Netherlands. A recorded earthquake signal will be applied to the tank that is located on top of a layer of soil. The soil stiffness is selected sufficiently low to expect a detectable amount of soil-structure interaction, while stiff enough to represent a realistic case. The number of wall segments may vary with the size of the tank, but is for this case set at three. The number of segments can easily be adjusted to fit the requirements of a specific design. The considered fluid is water and the tank is assumed to be completely full.
The values of the various model parameters are described in more detail, after which the results are presented and discussed.

3.1.1 System parameters

The soil layer has a thickness of $h_s = 30m$, and is considered to be medium stiff. From table 3.1 in EN 1998-1, this corresponds to a shear wave speed of $c_s = 270$m/s. The parameters in the soil model, E_s, ν_s and ρ_s are selected such that the given shear wave speed is obtained. Reasonable combinations of these parameters are derived from table 2.16 by Fredlund, Rahardjo, and Fredlund (2012), regarding the soil densities. Table 14.4 by Fredlund et al. (2012) and table 5-16 from the U.S. Department of Transportation (2006) provide information regarding the Poisson's ratios.
The soil material damping is fixed at $\xi_s = 0.02$ (introduced in equation (2.35)). The material damping ratio is, as are all soil parameters, not a straight-forward parameter either and is dependent on soil type, loading regime, strain level and measurement methods. However, ranges reported, for example, by Bolton Seed, Wong, Idriss, and Tokimatsu (1986), Vucetic and Dobry (1991), or Lin, Ni, Wright, and Stokoe (1988) include the 2% damping ratio in the linear regime. The applied parameters are listed in table 3.1.

The considered fluid, as stated previously, is water and is considered to fully occupy the tank. The parameter values can again be found in table 3.1.

A steel tank is considered with a radius of $R = 15$m, and an aspect ratio of 1.0, so that the height of the tank is $H = 15$m. The tank wall consists of three wall segments, each with a height of 5m. To determine the wall thicknesses, sections 8.3.1 and 9.2.2 (based on Barlow's formula) of European code EN 14015 (2004) are applied. The wall thickness, e_c, of a segment is given as

$$e_c = \max\left\{ \frac{D}{20S}\left(98W[H_c - 0.3] + p\right) + c \quad ; \quad 5\text{mm} \right\} \tag{3.1}$$

in which D is the tank's diameter, $S = 230\text{N/mm}^2$ is the assumed allowable stress, W is the fluid density, H_c is the distance from the bottom of the segment to the fluid level, $p = 0$mbar

Table 3.1 – *Model parameter values for case study*

Tank				*Fluid*		*Soil*	
R	15m	$H^{(1)}$	5m	H_{fl}/H	1	ρ_s	1800kg/m^3
H	15m	$H^{(2)}$	5m	ρ_{fl}	1000kg/m^3	c_s	270m/s
h_p	7mm	$H^{(3)}$	5m			ν_s	0.3
E_T	200GPa	$h_w^{(1)}$	10mm			h_s	30m
ν_T	0.27	$h_w^{(2)}$	7mm			ξ_s	0.02
ρ_T	7800kg/m^3	$h_w^{(3)}$	6mm				

the assumed internal pressure and $c = 0$mm is the assumed corrosion allowance. The plate thickness, e_a, is determined with

$$e_a = \max\left\{3 + \frac{e_1}{3} \quad ; \quad 6\text{mm}\right\} \tag{3.2}$$

in which e_1 is the thickness of the bottom wall segment.

3.1.2 Excitation

For the excitation of the system, an accelerogram is used that was obtained in the Groningen area in the Netherlands (Deltares (2015)). The time signal is transformed to the frequency domain with the use of the Fourier transform in equation (2.1), as presented in figure 3.1. Due to the shallowness of the induced earthquake, with a focal depth of approximately 3km, the signal shows a significant vertical component.
The spectral accelerations are transformed to the incident displacement field with equation (2.61). The horizontal component of the earthquake is chosen to be in the direction of $\theta = 0$, so that $\tilde{\mathbf{u}}_i(r, \theta, \omega)$ becomes

$$\begin{bmatrix} \tilde{u}_{i;r}(r,\theta,\omega) \\ \tilde{u}_{i;\theta}(r,\theta,\omega) \\ \tilde{u}_{i;z}(r,\theta,\omega) \end{bmatrix} = -\frac{1}{\omega^2} \begin{bmatrix} \cos(\theta) & -\sin(\theta) & 0 \\ \sin(\theta) & \cos(\theta) & 0 \\ 0 & 0 & 1 \end{bmatrix} \begin{bmatrix} \tilde{a}_x(\omega)\exp(-ir\cos(\theta)\omega/c_R) \\ 0 \\ \tilde{a}_z(\omega)\exp(-ir\cos(\theta)\omega/c_R) \end{bmatrix} \tag{3.3}$$

with $c_R = \zeta\sqrt{G_s/\rho_s}$ and $\zeta = (0.862 + 1.14\nu_s)/(1 + \nu_s)$.

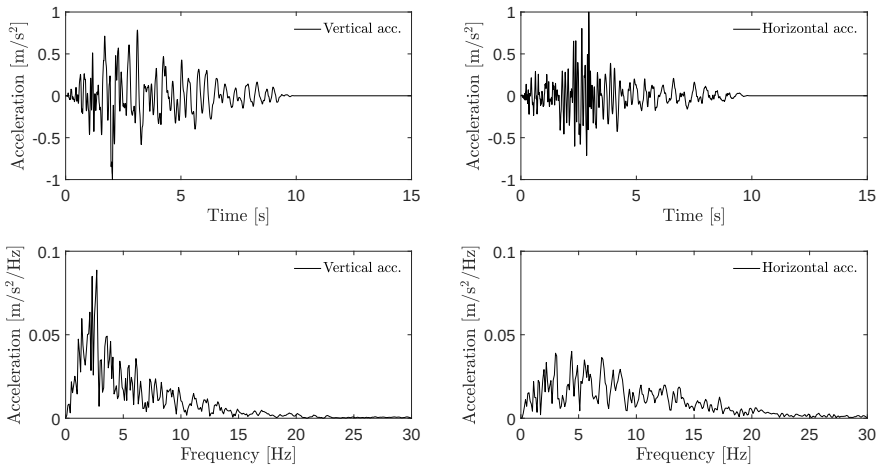

Figure 3.1 – *Vertical (left) and horizontal (right) components of earthquake signal in time (top) and frequency (bottom) domain (source: Deltares (2015))*

3.2 Convergence

The analytical nature of the model theoretically allows an exact solution to the problem, however, the introduction of a number of discretizations practically limits its accuracy. Refinement of the discretizations improves the model's accuracy, but also increases its computation time. In this section, the convergence of the model is therefore investigated.
A 'global' discretization is introduced with the summation over the structure and the fluid modes. A 'local' discretization is introduced with the division of the soil-structure interface into circular elements. Both the number of modes and number of elements included in the model for the analyses are determined in this section.
While all discretizations should be checked for convergence at each frequency of excitation, this is computationally expensive. The checks are instead performed for a number of relevant frequencies of excitation of $f_{\text{excitation}} = \{2, 3, 4, 6\}$Hz, at which the earthquake spectra (figure 3.1) contain a relatively large amount of energy. The examined cases are considered to be representative for the other frequencies of excitation and the resulting discretizations are applied for each of them.
Finally, it is checked whether uplift occurs, by considering the dynamic stresses at the soil-structure interface and adding the static pressure of the tank-fluid system. If the resulting stresses on the soil surface are upwards, uplift is considered to occur and the results are considered to be invalid.

3.2.1 Structure modes

The tank's modes have radial and circumferential components. Convergence for the radial modes is considered here in relation to the maximum stresses in the tank wall. Since, roughly categorized, the lower order modes are related to the plate and the higher order modes to the wall, a response of the wall is more suitable to base the criterium on. The maximum von Mises stress in the wall at cross-section $\theta = 0$ is determined with 15, 20, 25, 30 and 35 radial modes (figure 3.2). The error ε_σ is defined as the percent difference between the

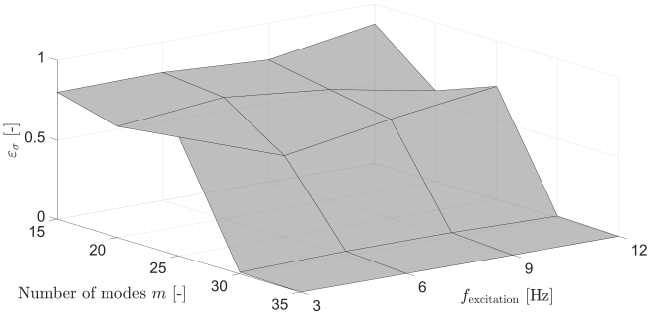

Figure 3.2 – *Convergence of maximum von Mises stress in cross-section of wall at $\theta = 0$ for an increasing number of axial structure modes m*

found von Mises stresses and the estimated asymptotic von Mises stresses that the results converge towards:

$$\varepsilon_\sigma = |\sigma_{\text{vM,max}} - \sigma_{\text{vM,max;asymp}}|/\sigma_{\text{vM,max;asymp}} \tag{3.4}$$

While the error is relatively large at lower numbers of modes, the difference between 30 and 35 modes at each of the considered frequencies is less than 2.7%. The decrease of ε_σ is not monotonic. The 'available' shapes at $m = 15$ to linearly combine into the modeled response of the tank cannot be combined to capture the actual response. While adding more modes should bring the modeled response closer to the actual response, the resulting maximum stress in the tank wall of an erroneous response is not necessarily closer to the actual maximum stress, especially since the vertical coordinate of the maximum stress may vary.
By the same means, the number of circumferential modes n can be determined. It was found that the increase of $n = 4$ to $n = 5$ changed the maximum von Mises stress by less than 0.9%. The numbers of modes applied are therefore $m = 35$ and $n = 5$.

3.2.2 Fluid modes

The fluid is also discretized into axial and circumferential modes. Convergence of the axial fluid modes is related here to the satisfaction of the interface conditions at the wall and bottom plate, which prescribe velocity continuity of the fluid and tank. The satisfaction of the interface conditions was examined for $a = b = c = \{10, 20, 30, 40, 50\}$. Since the satisfaction of the interface conditions was in all cases better for the plate than the wall, the results of the wall are reported (figure 3.3).

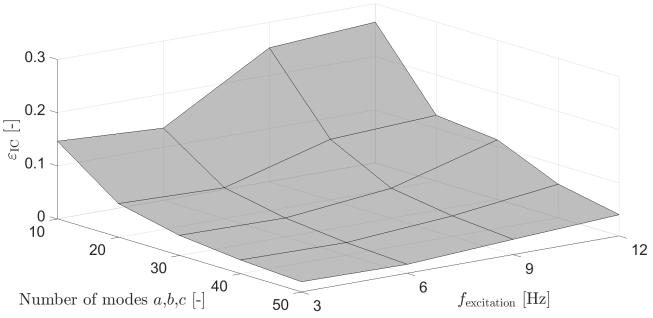

Figure 3.3 – *Convergence of satisfaction of velocity continuity condition at wall for an increasing number of axial fluid modes* $a = b = c$.

The error $\varepsilon_{\mathrm{IC}}$ is defined as

$$\varepsilon_{\mathrm{IC}} = \text{average}\left\{|v_{fl;r} - v_{w;r}|/v_{fl;r}\right\} \tag{3.5}$$

in which $v_{fl;r}$ is the velocity of the fluid at the wall and $v_{w;r}$ is the velocity of the wall. The error is thus the average of the velocity difference between the fluid and the wall over the height of the interface, relative to the fluid velocity. As the number of mode shapes increases, the actual fluid response can better be approximated and the relative error to satisfaction of the interface decreases monotonically. At $a = b = c = 50$, the relative error is reduced to 4%. In practice $a = b = c = 100$ is applied with an error of 1.2%, which is deemed acceptable.
The number of circumferential modes n is the same number that was checked for the structure modes. No additional verifications for this number are thus required.

3.2.3 Soil-structure interface

The final convergence check performed is on the discretization of the soil-structure interface. As reported, the interface is divided into a number of rings, n_r, and a number of angular segments, denoted n_θ. Convergence is related here to the pressure of the fluid on the wall at the location $(r = R, \theta = 0, z = 0)$. The fluid pressure is determined for interface discretizations with 24, 30, 36, 42 and 48 radial segments and with 30, 40, 50, 60 and 70 angular segments (figure 3.4).

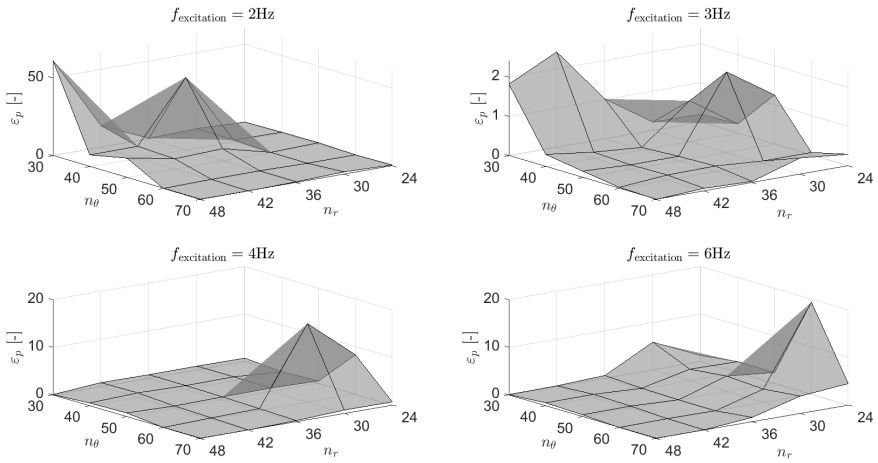

Figure 3.4 – *Convergence of fluid pressure at* $(r = R, \theta = 0, z = 0)$ *for increasing numbers of radial and angular segments.*

The error ε_p is defined as the relative difference between the found fluid pressures and the estimated asymptotic fluid pressure that the results converge towards:

$$\varepsilon_p = \left\{ |p_{\text{fl}} - p_{\text{fl;asymp}}| / p_{\text{fl;asymp}} \right\} \Big|_{r=R,\theta=0,z=0} \tag{3.6}$$

While ε_p can be large and unpredictable at low numbers of n_r and n_θ, the results stabilize for larger numbers. The unpredictability at rough discretizations is not necessarily surprising, as the solution method is essentially a weighted fitting of the mode shapes. Due to the complexity of the system it is not trivial to predict which mode shapes might just fit at which discretizations to give an unexpected response.
The largest difference at the finest discretizations is observed at $f = 3\text{Hz}$ from $n_r = 42$ to $n_r = 48$ with 6.9%. In the analyses, $n_r = 48$ and $n_\theta = 70$ are applied.
Finally, at the soil-structure interface, no tensile stresses from the soil can in reality develop to hold the tank attached to the soil. If they are present in the model at any location of the interface, this would in reality imply the occurence of uplift. A check is therefore performed by adding the static pressure of the fluid to the dynamic stresses at the interface. No uplift was detected, which is unsurprising given the low aspect ratios and the low excitation.

3.3 Results

3.3.1 Tank

After finding the modal amplitudes, the displacements and stresses can be determined at any location in the tank in the frequency domain, and with the inverse Fourier transform in equation (2.1) also in the time domain. Figure 3.5 shows the stresses σ_{zz} at the vertical coordinates $z = 0.30\text{m}, 5.04\text{m}, 10.02\text{m}$ of the tank wall, each in a different wall segment, at $\theta = 0$. The stresses $\sigma_{z\theta}$ and $\sigma_{\theta\theta}$ can also be determined, as well as the von Mises stresses.

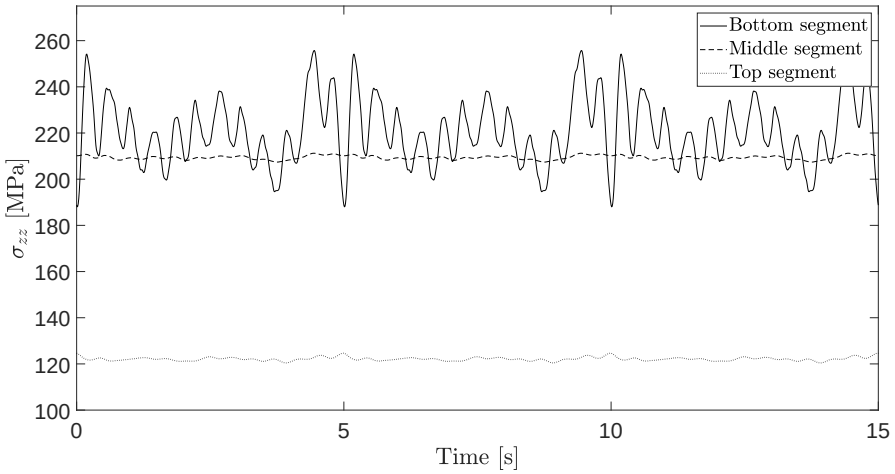

Figure 3.5 – *Static and dynamic stresses for a location in each wall segment* $z = 0.30\text{m}, 5.04\text{m}, 10.02\text{m}$ *at the circumferential section* $\theta = 0$

The stresses shown are the superposition of the static and the dynamic stresses. The static stresses, which result from the hydrostatic fluid pressure, are similar in the lower two segments, whereas the static stresses in the top segment are lower. Due to the minimum thickness criterium in the EN 14015 code, the material's resistance capacity is not fully mobilized. At the same time, the dynamic stresses in the top two segments are much lower than those in the bottom segment. This is related to the vibration shapes of the tank-fluid system, which is treated in more detail below.
Considering the entire tank's displacements and stresses at a moment in time, which can be found in figures 3.6 and 3.7, it is easily seen that the largest stresses occur at the bottom of the tank wall. The displacement and stress patern resemble the elephant foot bulge shown in figure 1.3. There is some variation over the height, but the magnitude of those values is small compared to those found in the bottom segment.

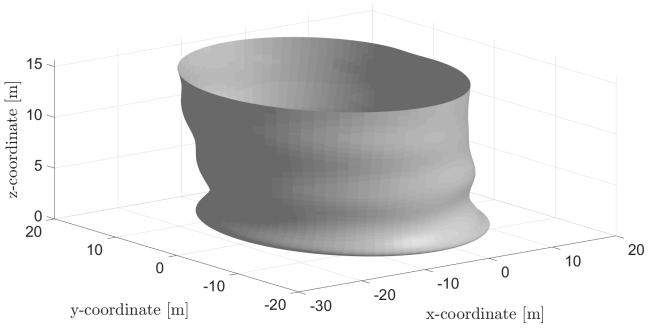

Figure 3.6 – *Displacements (scaled by 500) of tank at time* $t = 1.6s$

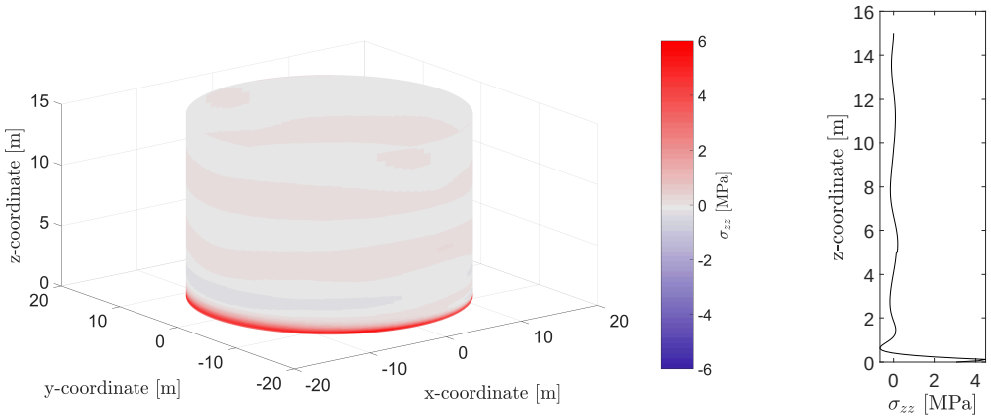

Figure 3.7 – *Dynamic stresses σ_{zz} of tank (left) and of section at $\theta = 0$ at outer surface of wall at time $t = 1.6s$*

Although difficult to see, the stresses jump in magnitude at the interface between the wall segments. The increases are substantial in this specific case with 40% between the bottom and middle segment and 27% between the middle and top segment. Given the small values at both interfaces compared to the static stresses, these jumps are not considered relevant for this scenario, but they can be in other cases. It is thus beneficial to be able to compute them in a direct manner.
Finally, it is noted that, contrary to what is expected of a system with damping, the system's response does not decrease over time, while the excitation does decrease (see figure 3.1). This is the result of the applied lowest considered frequency and frequency resolution, both of 0.2Hz. In the time domain this smallest frequency results in a periodic signal with at most a period of 5s. It is therefore not possible with the applied frequency range to model the response to the signal that lasts almost 10s. The remainder of the results in this section will therefore be presented in the frequency domain. While this invalidates the results in figures 3.5 to 3.7, the figures do show the model's possibilities given the proper frequency range.

3.3.2 Fluid

The behavior of the fluid was split up by Housner into the so called convective and impulsive components (see section 1.1.4). The convective mass is the part of the fluid mass that exhibits a sloshing behavior, whereas the impulsive mass is the part of the fluid mass that moves in tandem with the tank wall. This distinction is observable in figure 3.8, where the elevation of the fluid level represents the sloshing component, and the fluid pressure at the interface between plate and wall represents the impulsive component.

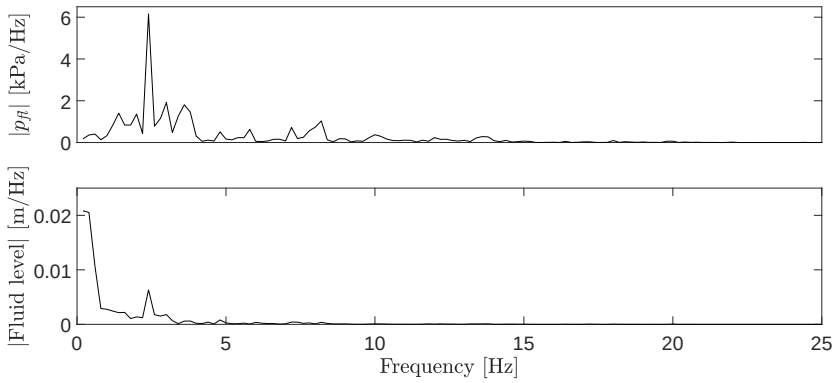

Figure 3.8 – *Absolute values of fluid pressure at* $(z = 0, \theta = 0)$ *and fluid elevation at* $(z = H_f, \theta = 0)$ *in the frequency domain*

The behavior of the convective mass is dominated by much longer period behavior than the impulsive mass, as was shown by Amabili et al. (1998); Bauer and Siekmann (1971); Veletsos (1984). Comparing figure 3.8 with figure 3.5 shows that the impulsive mass and stresses σ_{zz} are closely related, both dominated by vibrations at $f = 2.4$Hz.
The contribution of the fluid pressure on the wall and plate, as well as the elevation of the fluid level at that frequency to the final solution are shown in figures 3.9 to 3.11.

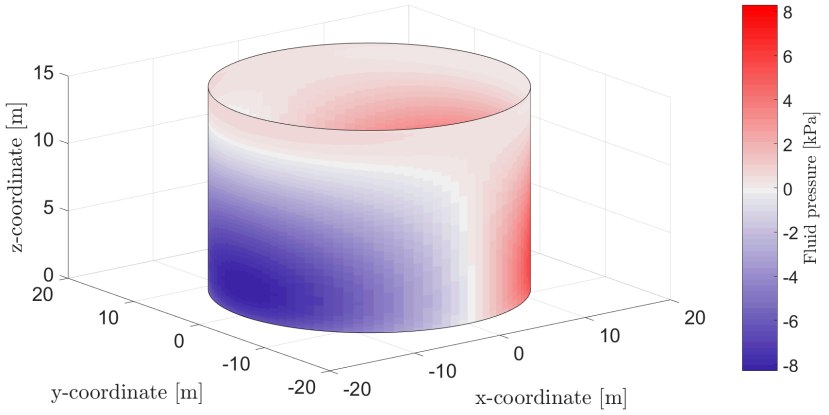

Figure 3.9 – *Pressure of the fluid acting on the wall at* $f = 2.4$Hz *with positive values acting outwards*

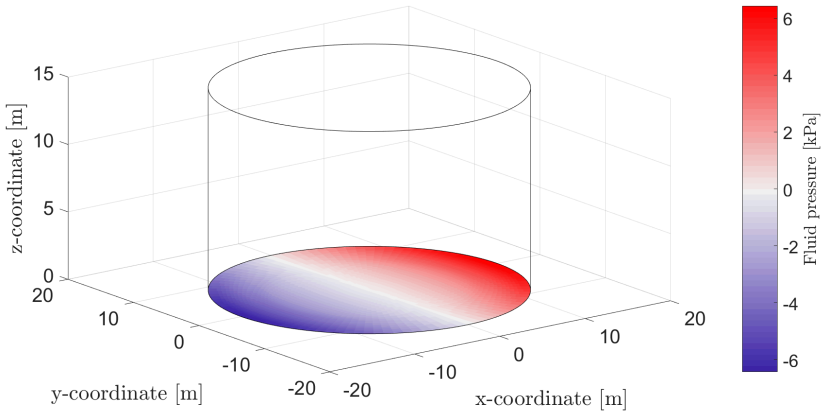

Figure 3.10 – *Pressure of the fluid acting on the plate at* $f = 2.4$Hz *with positive values acting downwards*

It is noted that filling the considered tank to the rim will lead to spilling of its contents at any amount of sloshing, which is why a freeboard is applied in practice.

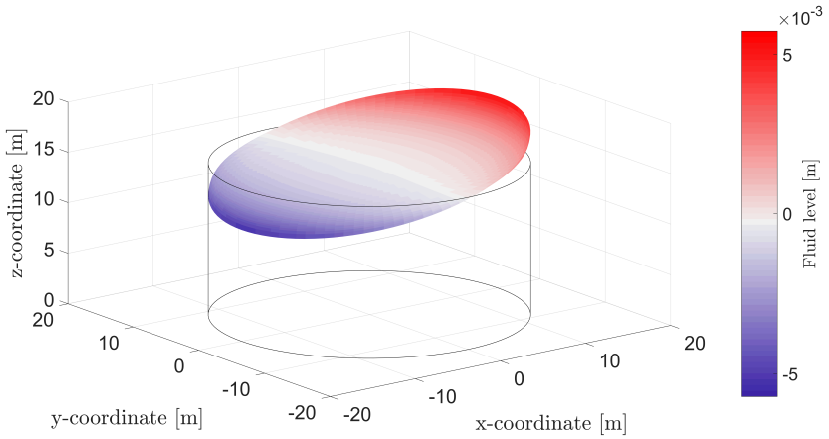

Figure 3.11 – *Elevation of the fluid fluid level at* $f = 2.4$Hz *scaled by 1000*

3.3.3 Soil

In order for the tank to withstand a seismic event, not just the tank itself needs to be verified, but also the soil it is founded on. With knowledge of the stresses at the soil-structure interface, verifications can be performed for the soil. The stresses acting from the soil on the tank's bottom plate are known, as they serve as input in the plate's equations of motion. They are equal to the stresses acting from the plate on the soil, expressed in the stress continuity condition at the soil-structure interface (equation (2.54)). As is the case for all variables in the model, the interface stresses can be presented in both time and frequency domain at every location on the interface.
Comparing the stresses σ_{zz} at the soil surface with the fluid pressure at $f = 2.4$Hz (see

figure 3.10) shows the relation between those two in figure 3.12. While the figure shows a stress patern that somewhat resembles the fluid pressure pattern, this image is distorted by the effects that the tank and the incident wave field have on the interface stresses.

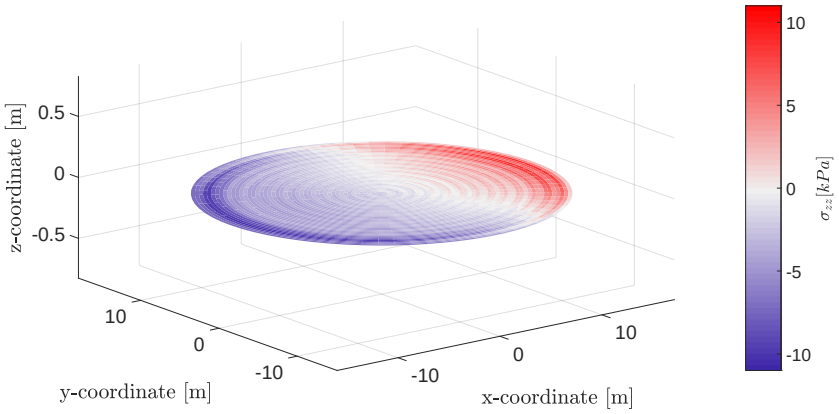

Figure 3.12 – *Stresses σ_{zz} acting from the soil on the soil-structure interface at $f = 2.4$Hz*

It is also clear that the stresses at the edge of the interface are much higher. This is related to a phenomenon noted also by Molenkamp (2018), namely that the effective stiffness at the edge of the interface is larger than at the center. This is also reflected in figure 3.13.

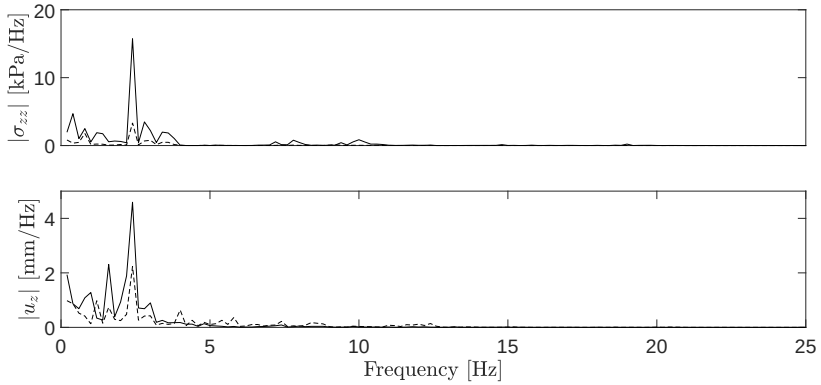

Figure 3.13 – *Absolute values of soil-structure interface stresses and displacements at edge (solid) and center (dashed) in frequency domain with positive values acting upwards*

While stresses and displacements are both higher at the edge of the soil-structure interface, the ratio between the two is larger at the edge than at the center, indicating a higher effective stiffness. The bigger displacements at the edge indicate a rocking behavior, while the presence of vertical displacements at the center indicate that the tank also undergoes vertical translations. The latter is not surprising given the relatively large vertical excitation

component (figure 3.1).
Besides stresses and displacements at the soil-structure interface, the effect can be shown of the motions of the tank-fluid system on the soil displacements surrounding it (figure 3.14). The figure shows that modes of the tank are excited in which the bottom plate vibrates with a relatively high wavenumber. While the figure's scaling exaggerates this effect, it is noted that the low thickness of the plate makes it flexible, allowing this behavior at low frequencies of vibration. In practice, this is unlikely to occur, as some form of foundation improvement would be applied, e.g. a concrete slab or soil improvements, that would reduce the observed behavior.

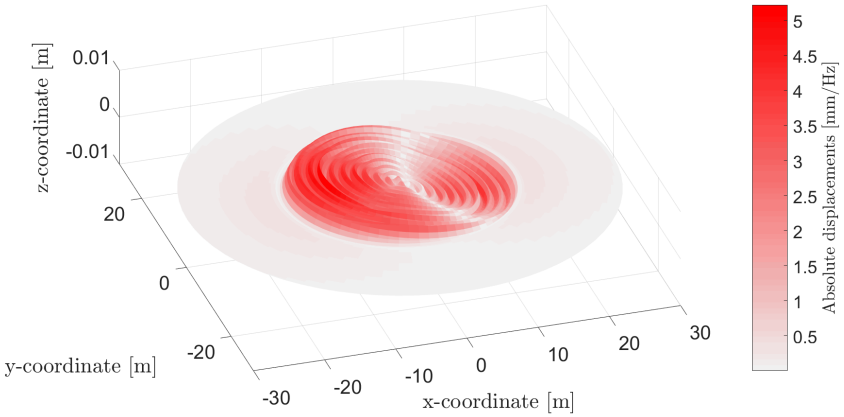

Figure 3.14 – *Soil displacements at soil-structure interface ($r \leq R$) and the soil surface surrounding the tank ($r > R$) as a result of the motions of the tank at $t = 2.4$Hz*

Radiation damping is a form of damping caused by traveling waves that carry energy away from the tank-fluid system. However, traveling waves generated by the motions of the tank-fluid system appear to be absent in figure 3.14. This can be explained considering the wavelengths of the waves traveling at this frequency in this soil, which can be computed to be over 100m with

$$\lambda = \frac{c_R}{\omega} = \frac{0.862 + 1.14\nu_s}{1 + \nu_s} \frac{c_s}{\omega} \tag{3.7}$$

in which c_R is the Rayleigh wave speed. The propagating waves are thus simply not visible in figure 3.14. For practical reasons and the prospect of limited additional information, it was decided to not increase the boundaries of the soil domain of the figure.
As was presented in section 2.4.5, the amount of energy leaving the system over the duration of one period can be computed at every frequency. Expressed as a fraction of the energy in the tank-fluid system, the damping can be shown (figure 3.15) to be frequency dependent. The low values of damping at the lower frequencies can be explained by the cut-off frequency of the soil layer. Waves with frequencies below this value, do not propagate and therefore do not carry much energy away from the tank-fluid system. The occuring damping is the result of material damping.
The fluctuations stem from soil resonances, as was shown by Molenkamp (2018). Depending on the main mode of vibration, e.g. translational or rocking motions, different values of effective damping are expected. Paired with the different combinations of horizontal and

vertical excitation this obscures which exact mechanisms dominate the damping behavior at each frequency. It is also noted that values up to 70% might seem high, but are comparable to the amount of energy dissipated over one period by a single degree of freedom system with a damping ratio of 0.2. The computed damping does not vary linearly with the single degree of freedom damping ratios as values of 50% compare to a damping ratio of 0.1.

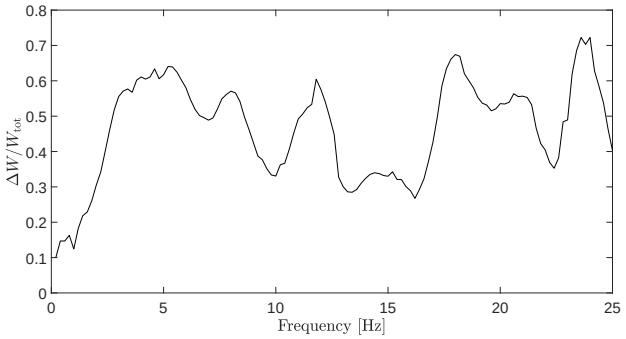

Figure 3.15 – *Ratio of dissipated energy to total energy in the system*

4 Parameter study

This section is concerned with the influence of the thickness of the soil layer, the soil material properties and the aspect ratio of the tank on the fundamental period of the tank-fluid system. This period increase is one of the main effects of including soil-structure interaction and its incorporation can shift the modeled fundamental eigenperiod to a part of the earthquake spectrum with a lower or actually higher excitation.
The current model employs a frequency dependent fully coupled soil stiffness matrix to represent the soil. Others, e.g. Tsouvalas et al. (2018), have used uncoupled vertical and horizontal springs and dashpots, of which the static values are derived from formulas presented by Gazetas (1983), based on a rigid plate. A short comparison is presented to evaluate to what extent this representation of the soil substructure is appropriate.
First, the different parameters and their applied values are discussed in more detail, followed by the parameter study. The comparison between the two soil models is then presented and this section is concluded with some general remarks on the results.

4.1 Parameters

As the attention is centered on the effect of soil-structure interaction, the material and geometrical properties of the soil layer are varied. For the comparison of the two soil models, these soil properties are converted to the respective model parameters with the formulas presented by Gazetas (1983). Also, a number of tank sizes is compared with constant ratios of h_s/R (layer thickness to tank radius), so that potential scaling effects can be observed. Fluid-structure interaction of liquid storage tanks with the current modeling approach has been discussed by others, e.g. Amabili et al. (1998); Bauer and Siekmann (1971); Canny (2018), so is left out of the analyses here.

4.1.1 Soil

The soil's geometrical parameter is the layer thickness that is assumed to be positively related to the flexibility of the system. A thickness of zero is equivalent to a infinitely stiff rigid foundation, whereas an infinite thickness is a half-space. The selected values are in between these limit cases, so that the system will to some extent experience the rigid boundary at the bottom of the layer. The dimensions of the tank itself are also relevant for the effective stiffness of a soil layer. The parameter varied in the investigation is therefore the ratio between the height of the soil layer and the radius of the tank, h_s/R. In addition, a number of tanks with different radii, but a constant h_s/R ratio is examined for potential scaling effects.
The soil material properties that are varied are the stiffness and the density of the soil. While soil is a complex material with greatly varying properties and combinations of properties, the model requires relatively simple parameters that capture soil behavior in general terms. One type of classification of soil in terms of dynamic properties is in shear wave speed (Larkin (2008) or EN 1998-1 (2005)).
Based on table 3.1 in EN 1998-1, wave speeds are selected of 120m/s and 270m/s, that represent soft and moderately dense soils. Reasonable combinations of the parameters of the soil model are selected to obtain these wave speeds. The soil densities ρ_s are derived from table 2.16 by Fredlund et al. (2012). The soil's moduli of elasticity and Poisson's ratios E_s and ν_s are found in table 14.4 by Fredlund et al. (2012) and table 5-16 from the U.S.

Department of Transportation (2006).
The final soil parameter is the material damping parameter ξ_s, which is kept constant at 2% for both soil types. Maintaining a fixed material damping ratio allows for better comparison. An overview of the applied soil parameters can be found in table 4.1.

Table 4.1 – *Soil parameter values*

Soil type	h/R [-]	ρ_s [kg/m^3]	ν_s [-]	c_s [m/s]
1	{1; 2; 4}	1600	0.4	120
2	{1; 2; 4; 6}	1800	0.3	270

In order to compare the currently applied soil model with the one applied by Tsouvalas et al. (2018), model parameters for the latter must be selected such that they represent the same soil layer. The parameters are determined with the formulas presented by Gazetas (1983), which give lumped values of static stiffness parameters for a circular rigid plate on a soil layer over a rigid boundary:

$$\begin{aligned} K_v &= \frac{4G_sR}{1-\nu_s}\left(1+1.28\frac{R}{h_s}\right) \qquad \text{for} \qquad h/R \geq 2 \\ K_h &= \frac{8G_sR}{2-\nu_s}\left(1+\frac{R}{2h_s}\right) \qquad \text{for} \qquad h/R \geq 1 \\ K_r &= \frac{8G_sR^3}{3(1-\nu_s)}\left(1+\frac{R}{6h_s}\right) \qquad \text{for} \qquad 4 \geq h/R \geq 1 \end{aligned} \tag{4.1}$$

The shear modulus G_s is expressed by rewriting equation (2.46) as

$$G_s = \rho_s c_s^2 \tag{4.2}$$

Following Canny's approach, the area, $A = \pi R^2$, and second moment of area, $I = \pi R^4/4$, of the soil-structure interface can be used to transform the lumped parameters to distributed spring parameters. Both K_v and K_r lead to a different value of the vertical spring stiffness, so as a simple compromise the average of the two values is used. The distributed spring values are therefore

$$\begin{aligned} k_h &= K_h/A_p \\ k_v &= \frac{K_v/A_p + K_r/I_p}{2} \end{aligned} \tag{4.3}$$

Following Tsouvalas et al. (2018), the damping ratios are taken as $c_h = 0.03k_h$ and $c_v = 0.03k_v$.

4.1.2 Fluid

Since fluid-structure interaction is not of primary concern in this investigation, the fluid properties are kept constant. The fluid parameters are the density and the fill ratio, which is defined as the level of the fluid relative to the height of the tank (H_{fl}/H). Their values are reported in table 4.2.

Table 4.2 – *Fluid parameter values*

Parameter	*Value*	*Unit*
Density	1000.0	kg/m^3
Fill ratio	1.0	-

4.1.3 Tank

The geometrical parameter of the tank substructure that has the highest impact on its seismic behavior is the aspect ratio, which is defined as AR $= H/R$. As shown in figure 1.3, different aspect ratios are associated with different failure modes and tanks with higher aspect ratios tend to exhibit a rocking motion, whereas tanks with lower aspect ratios tend to display more translational motions (Larkin (2008)). Although these potential differences would be interesting to examine, most tanks with high aspect ratios are anchored, due to the risk of uplifting.
Uplift occurs when, after superposition of the static and dynamic stresses, the net stresses from the tank acting on the soil are upwards. In the model, the soil and tank displacements are equal so that the soil will exert downward stresses on the tank. In reality, the tank will simply lift from the soil, or, in the case of anchored tanks, the anchors will exert the stresses to resist uplift. However, this will lead to different stress distributions that are currently not in the model, so that tanks with such high aspect ratios are not included in the analyses.
Another parameter of the tank, its radius relative to the soil layer height, was discussed earlier. To examine the previously mentioned potential scaling effect, tanks with three different radii are applied in the analyses, associated with small up to large liquid storage tanks.
The applied material of the tanks is steel, which is not varied. The values of the material properties can be found in table 4.3.
To determine the wall and plate thicknesses, use is made of sections 8.3.1 and 9.2.2 of EN 14015 (2004), so that a consistent rule is applied in the determination of the wall and plate thicknesses of all considered tanks. The wall thickness e_c of a segment is computed with

$$e_c = \max\left\{\frac{D}{20S}\left(98W[H_c - 0.3] + p\right) + c \quad ; \quad 5\text{mm}\right\} \tag{4.4}$$

in which D is the tank's diameter, $S = 230\text{N/mm}^2$ is the assumed allowable stress, W is the fluid density, H_c is the distance from the bottom of the segment to the fluid level, $p = 0$mbar the assumed internal pressure and $c = 0$mm is the assumed corrosion allowance. The plate thickness, e_a, is found with

$$e_a = \max\left\{3 + \frac{e_1}{3} \quad ; \quad 6\text{mm}\right\} \tag{4.5}$$

in which e_1 is the thickness of the bottom wall segment. An overview of the applied tank parameter values can be found in table 4.3.

Table 4.3 – *Tank parameter values*

R [m]	H/R [-]	ρ_t [kg/m^3]	ν_t [-]	E_t [GPa]	h_w [m] & h_p [m]
{7.5; 15.0; 30.0}	{0.5; 1.0}	7800	0.27	210	From EN 14015

4.1.4 Excitation

The excitation of the system consists of an incident displacement field (equation (2.61)). The analyses concentrate on the increase of the system's fundamental period, as a result of incorporating SSI and varying the system parameters. The least confounding input displacement field to examine the sensitivity of the system's response to varying system parameters is a horizontal and a vertical uniform displacement. A range of frequencies is considered between 0.2 - 25.0Hz with a step size of 0.2Hz, and an acceleration amplitude at each frequency of 1m/s^2/Hz.

Table 4.4 – *Excitation parameter values*

Type	*Freq. range* [Hz]	*Resolution* [Hz]	*Amplitude* [m/s^2/Hz]
Uniform hor. & vert.	0.2 - 25.0	0.2	1.0

4.2 Results

4.2.1 Determination eigenperiods

The increase of the first eigenperiod is expressed as T_0/T_{stiff}, in which T_{stiff} is the first eigenperiod of a tank-fluid system on a rigid foundation and T_0 the first eigenperiod of the same tank-fluid system, founded on a flexible soil layer ($T_{\text{stiff}} < T_0$). The first eigenperiods of the systems, T_0 are determined by means of so-called peak picking, which is a method of finding the frequency response function of a system and identifying the frequencies at which the frequency response function attains a peak value (see for example figure 4.1).

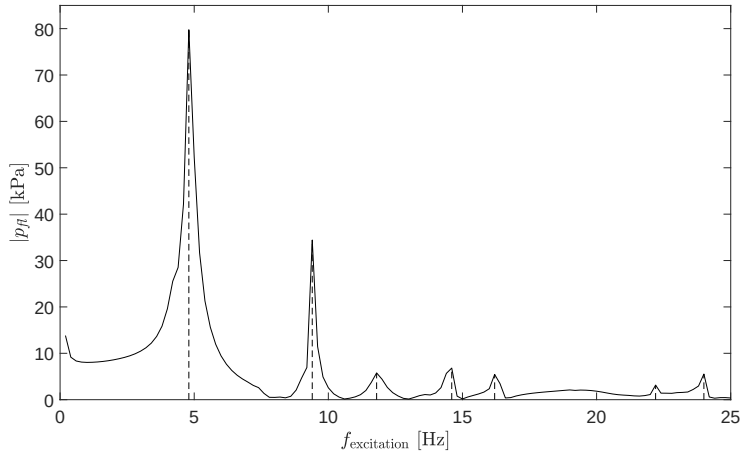

Figure 4.1 – *Peak picking example for a tank with* $R = 15$m*, aspect ratio of 0.5 on a soil layer with a thickness of* $h_s = 15$ *of soil type 2, loaded in vertical direction*

To find the first eigenperiods of a system with a rigid foundation, the following soil parameters were applied in equations (4.1) and (4.3): $\rho_s = 2200\text{kg/m}^3$, $\nu_s = 0.4$ and $c_s = 800\text{m/s}$. The resulting spring stiffnesses were multiplied by 10, resulting in values approximately 1000 times as large as the ones representing flexible soils. For the load case of horizontal excitation at the soil surface, the first eigenperiods of the systems with a rigid foundation

can also be found from equation A.35 in EN 1998-4 (2007), which were compared to the ones obtained from peak picking. The eigenfrequencies for the vertical excitation of the soil surface were obtained just from the peak picking method.

4.2.2 Soil type and layer height

For soil type 2, representing a moderately stiff soil, four ratios of layer height to tank radius were examined (figure 4.2). The fundamental periods of the systems increase compared to the case with a rigid foundation, as the soil layer thickness increases. Especially from h_s/R ratios of 2 to 4 and from 4 to 6, a diminishing effect on the period increase is observed. This is in line with the expectation that the relative layer thickness decreasingly influences the results as the layer thickness increases.

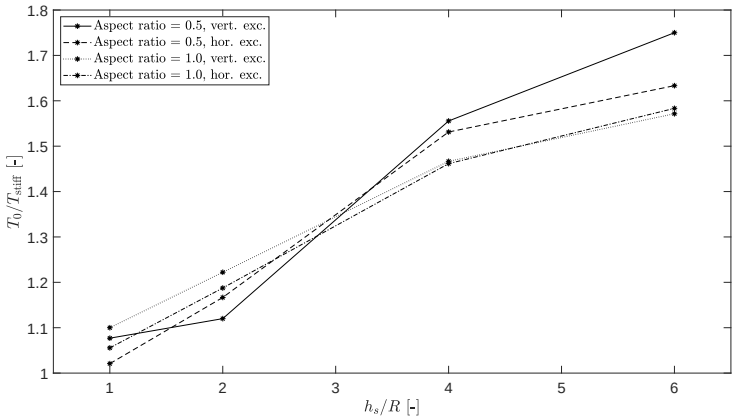

Figure 4.2 – *Period increase for a tank with radius* $R = 15$m *on a soil layer of soil type 2 with varying layer height: 15m, 30m, 60m and 90m*

The trajectory of the scenario of the vertically excited tank with an aspect ratio of 0.5 slightly deviates from the expected pattern at $h_s/R = 2$. This is most likely related to the frequency dependency of the behavior of a soil layer. As shown by Molenkamp (2018), sudden decreases in the effective stiffness and damping can occur at the soil's resonance frequencies. These frequency dependent stiffness and damping properties do not follow a simple relation with the increase of the h_s/R ratio. As the dynamic soil stiffness is the added component to the system, it is not unexpected that some of the found period increases deviate from the expected pattern.
It is also noted that the period increase varies little between tanks with different aspect ratios or between the load directions. For horizontal loading, differences could be expected for different overall behavior, such as rocking as opposed to translational motions. However, in order to observe such differences, tanks with a higher aspect ratio need to be examined.

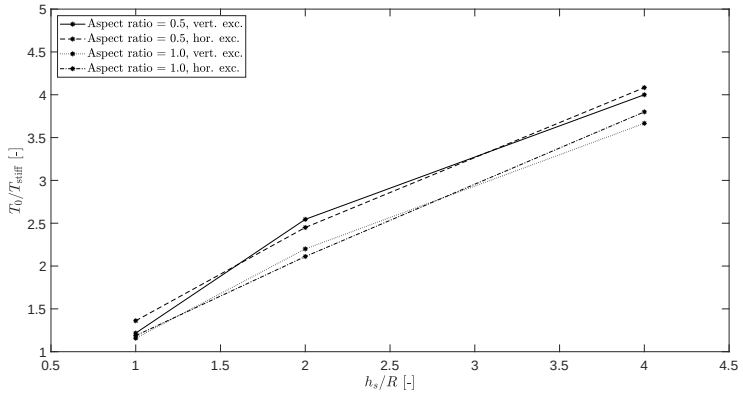

Figure 4.3 – *Period increase for a tank with radius* $R = 15\text{m}$ *on a soil layer of soil type 1 with varying layer height: 15m, 30m and 60m*

For soil type 1, three layer heights were examined, at h_s/R ratios of 1, 2 and 4 (figure 4.3). Compared to soil type 2, the most obvious observation is that the period increase at each h_s/R ratio is much larger with values of up to 4. These results seem high, but are actually similar to the values reported by Larkin (2008) for a tank of similar dimensions based on a design rule by Veletsos (see figure 4.4).

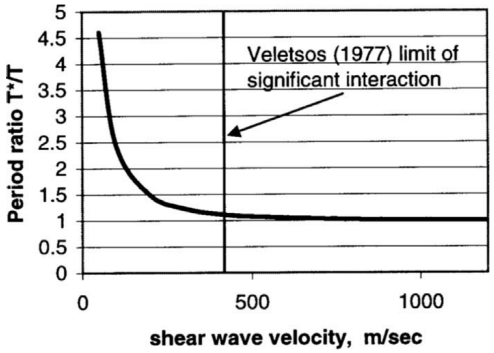

Figure 4.4 – *Period increase for a tank with radius of 10m and a height of 15m on a half space for varying shear wave velocities of the soil (source: Larkin (2008))*

4.2.3 Scale effects

To examine a potential scaling effect, three tanks are considered of radii $R = \{7.5, 15, 30\}\text{m}$ on a soil of type 2, with layer heights increasing in tandem with the radii.

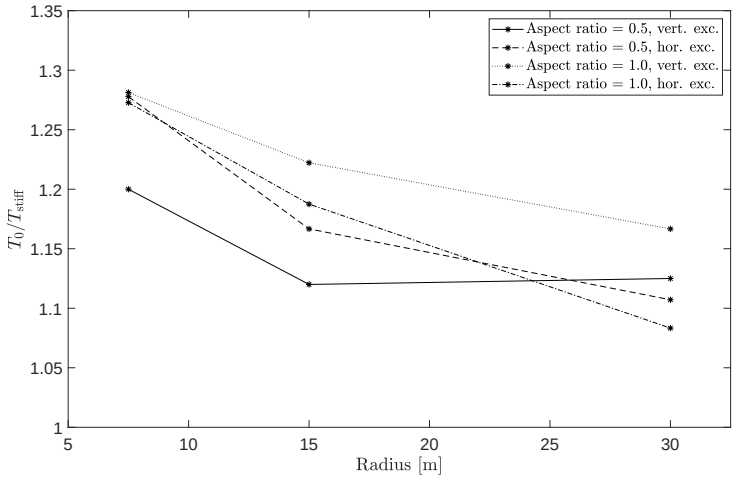

Figure 4.5 – *Period increase for tanks with constant $h_s/R = 2$ and soil type 2 for varying tank radii of $R = \{7.5, 15, 30\}$*m

From figure 4.5 it appears that the larger tanks on the thicker soil layers experience a smaller period increase. In general, structures with a larger foundation lead to a stiffer soil response as the reaction of a larger volume of soil is mobilized. For rocking, the effect of the radius is even stronger as the resistance of the soil to the overturning moment will involve the second moment of inertia of the interface. At the same time, a larger soil thickness should lead to a less stiff response, as the influence of the rigid boundary becomes less marked. It could be expected that the stiffness lowering aspect of increased soil layer thickness would offset the added stiffness of the increased foundation footing.
Figure 4.5 shows that the positive influence on effective soil stiffness of an increased foundation footing is stronger than the negative influence of a larger layer thickness. This is corroborated by Gazetas' formulas (equation (4.1)), in which this effect is even stronger. It is noted however, although they are insightful, the formulas do not consider the flexibility of the tank, nor the additional mass from the fluid, which are likely to have an effect on the mobilized soil. Figure 4.5 at least shows that the influence of the h_s/R ratio on the fundamental period increase shown in figures 4.2 and 4.3 should be complemented by a scale factor.

4.3 Comparison soil models

In this section a comparison is made between soil modeled as a spring-dashpot foundation, as presented by Tsouvalas et al. (2018), and the soil as a dynamic soil stiffness matrix. Roughly, two categories are compared, namely a relatively small tank on a relatively stiff soil and a larger tank on a relatively soft soil. As such, potential differences between the two models can be observed for systems that are expected to have relatively high and low fundamental eigenperiods respectively.
In the stiff category is a tank with a radius of $R = 7.5$m and an aspect ratio of 1.0, founded on a soil layer with a thickness of $h_s = 15$m of soil type 2 (see tables 4.1 and 4.3). The spring parameters are calculated with equation (4.3) and the excitation is applied as uniform horizontal soil surface displacements.
The first natural frequencies of the dynamic soil stiffness model and the modified Winkler

model are 6.6Hz and 7.6Hz respectively (figure 4.6). Compared to the first eigenfrequency of a rigidly founded tank of 8.4Hz, this difference is considered to be substantial. It is noted that, with the exception of the magnitude of the fluid pressure at the first eigenfrequency, the frequency response functions are rather similar, especially at the second eigenfrequency. It is also noted that the modified Winkler model produces smoother results than the dynamic soil stiffness model. This can be explained by the frequency dependency of the soil's effective stiffness and damping that are reflected in the dynamic response of the entire system.

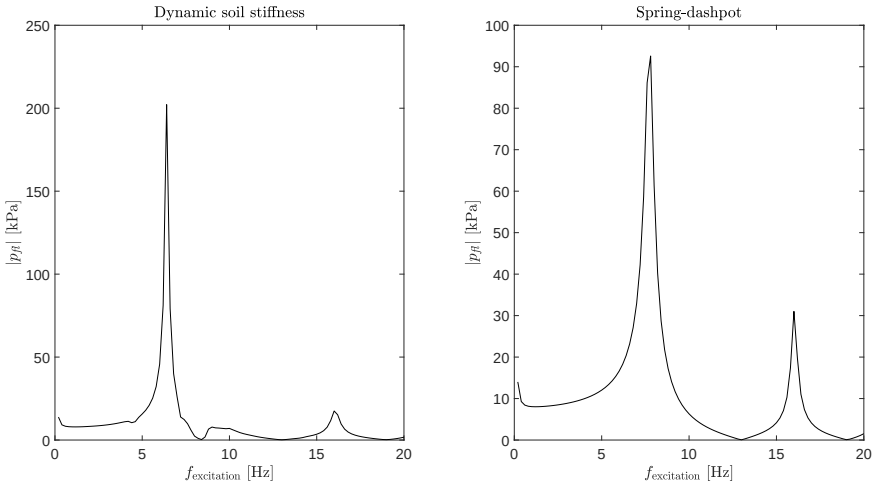

Figure 4.6 – *Frequency response functions of tank with radius* $R = 7.5$m*, aspect ratio of 1.0 on soil with* $h_s = 15$m *of soil type 2, horizontally excited*

Changing the aspect ratio of the previous scenario to 0.5 yields fundamental eigenfrequencies of 10.8Hz and 12.2Hz for the dynamic soil stiffness and the modified Winkler model respectively (figure 4.7). Compared to the first eigenfrequency of 13.8Hz for a rigid foundation, the difference is again considered to be substantial.
Other observations are also similar to the previous case. The magnitude of the fluid pressure at the first eigenfrequency is higher for the dynamic soil stiffness case, which might be explained by the frequency dependent damping of the soil. Molenkamp (2018) has shown that the damping of the soil can experience sharp decreases at the resonance frequencies of the soil. It is well possible that the these coincide with the eigenfrequency of the system. However, a more detailed analysis is required to investigate whether this is the case. For the comparison of the fundamental period increase between the two soil models, the current depth of analysis is sufficient.

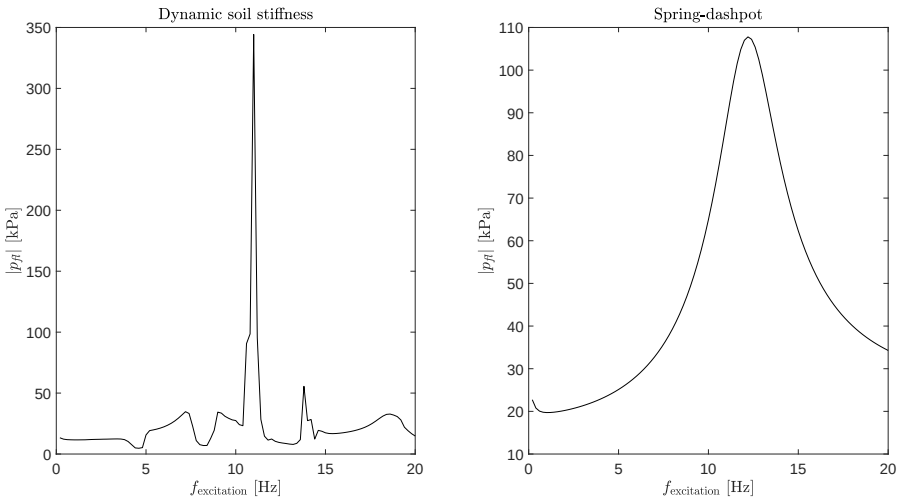

Figure 4.7 – *Frequency response functions of tank with radius* $R = 7.5$m*, aspect ratio of 0.5 on soil with* $h_s = 15$m *of soil type 2, horizontally excited*

In the category of systems with a low expected eigenfrequency, a tank is considered with a radius of $R = 15$m and an aspect ratio of 1.0 on top of a soil layer with thickness $h_s = 60$m of soil type 1 (see tables 4.1 and 4.3 for more details), excited in horizontal direction. This system experiences a considerable period increase with the first eigenfrequency at 1.0Hz and 2.8Hz for the dynamic soil structure and modified Winkler models respectively (figure 4.9), compared to the first eigenfrequency of 3.8Hz for the rigid foundation case. Relative to the stiffer previous cases, the difference between the two soil models is greater.

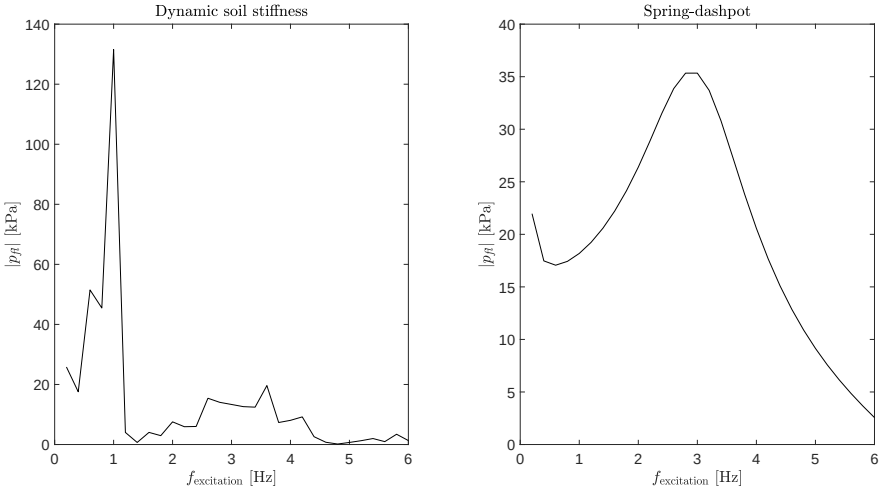

Figure 4.8 – *Frequency response functions of tank with radius* $R = 15$m*, aspect ratio of 1.0 on soil with* $h_s = 60$m *of soil type 1, horizontally excited*

Finally, the same tank is considered with uniform vertical displacements of the soil surface. The first eigenfrequencies of the dynamic soil stiffness and the modified Winkler models are 1.2Hz and 3.2Hz respectively (figure 4.8), whereas the first eigenfrequency of the tank on a rigid foundation is 4.4Hz. Again, the difference in the estimate of the first eigenperiod between the soil models is greater than in the stiffer scenarios.

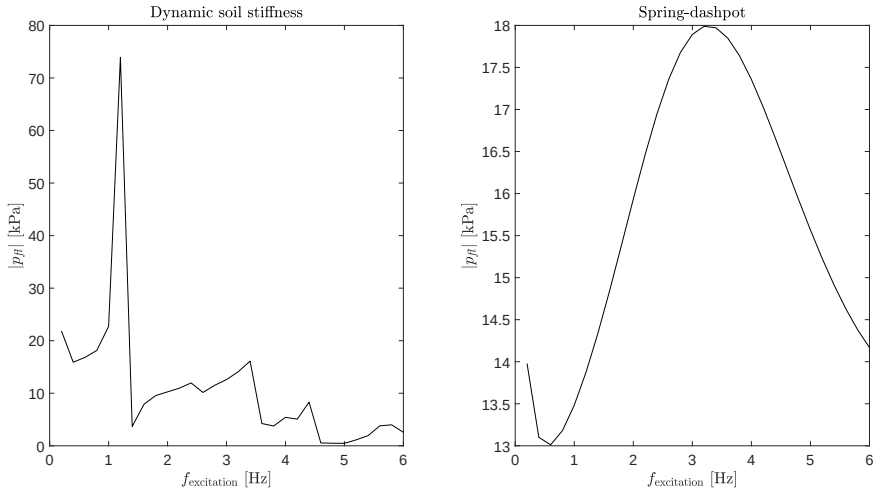

Figure 4.9 – *Frequency response functions of tank with radius* $R = 15$m*, aspect ratio of 1.0 on soil with* $h_s = 60$m *of soil type 1, vertically excited*

Overall, it is observed that the prediction of the first eigenfrequency of the two considered soil models diverges. The discrepancies increase for softer soils and larger soil layer thicknesses. The soil models differ in two main respects. The first is that the springs of the modified Winkler model have been derived from equations applicable for rigid plates, while the dynamic soil stiffness model is not. The second is that the modified Winkler model is frequency independent, while the dynamic soil stiffness model is not. Additional research would be required to find how much of the discrepancies between the results of the two models is caused by which of the main two model differences.

4.4 Conclusion

In this section, the effect of soil layer height and soil type as well as tank dimensions on the period increase of the system were examined. Then, the results of the dynamic soil stiffness model were compared to those of the modified Winkler model.
Overall, it is observed that both soil layer height and soil type have a substantial effect on the period increase of the system. Increasing the h_s/R ratio to 6 increased the first eigenperiod of the system up to 1.7 for soil type 2, representing a moderately stiff soil. For soil type 1, representing a soft soil, the period increased up to 4 times for a h_s/R ratio of 4. These results were similar to results obtained by Larkin (2008) for a tank of similar dimensions.
It was also found that the tanks experience a scaling effect. For a constant h_s/R ratio and soil type, tanks with a larger radius and the same aspect ratio experience a smaller period increase. This effect was supported by the formulas by Gazetas that show for a rigid plate

that doubling both layer thickness and plate radius doubles the stiffness of the soil.
To observe significant differences in fundamental period increases for rocking as opposed to translational motions, tanks with a higher aspect ratio need to be included. As these are at risk of uplift, a nonlinear effect that cannot be modeled by the linear model, anchors should be included in the model.

The comparison between the modified Winkler model and the dynamic soil stiffness model showed that the modified Winkler model estimates lower period increases than the dynamic soil stiffness model. This effect is stronger for softer soils with a larger layer thickness and is attributed to two main differences between the models. First, the spring parameters of the modified Winkler model are derived from formulas for a rigid plate. As Molenkamp (2018) showed, there is a difference in effective stiffness between the edge and the center of the interface that becomes larger for softer soils. This effect is not considered by a model for a rigid plate. Second, the modified Winkler model is not frequency dependent, while the response of the system was observed to be influenced by the soil's frequency dependency for the dynamic soil stiffness model. Certainty on the extent to which either of the two model differences influences the observed differences in period increases requires additional research, e.g. with a rigid bottom plate. It can however be concluded that accurate incorporation of soil-structure interaction is not just relevant for very soft soils, but also for moderately stiff ones.
Regarding computational efficiency, the modified Winkler model outperforms the dynamic soil stiffness model. To improve the latter, reducing the number of elements of the soil-structure interface should be considered. The axisymmetry of the applied discretization offers the advantage of having to compute many values just once, as they can be reused for other entries of the matrix. However, at the center, more elements are defined than necessary for accuracy purposes. As the sheer size of the matrix slows the computation down, it could be beneficial to develop an axisymmetric discretization with fewer elements at the center.
Finally, in practice, tanks such as the ones presented in figures 4.8 and 4.9 will not be constructed as such without foundation improvements. Although the scenarios are of theoretical value, in practice the layering of soil or addition of a foundation slab should be included in the model to examine tanks on such soft soils.

5 Conclusions & discussion

In this thesis, a model has been presented to predict the seismic response of liquid storage tanks, incorporating both fluid-structure and soil-structure interaction through a semi-analytical dynamic substructuring technique. As the main contribution has been the coupling of a more advanced soil model to the tank-fluid system, the focus is on soil-structure interaction.
The purpose has been to develop a model with the computational efficiency and ease of use comparable to other analytical models, while performing at a level of accuracy comparable to FE models. To achieve this, the computationally efficient mode-matching technique is used. This technique only sacrifices on accuracy through the limitations imposed by the assumptions of the underlying theories and a number of truncations. These are the number of soil, structure and fluid modes and the number of elements of the discretization at the soil-structure interface.
The model properly incorporates dynamic soil-structure interaction and the influence of soil-structure interaction is shown on the fundamental period increase of the tank-fluid system. In addition, a method is presented to determine the amount of damping of the tank-fluid system that occurs through soil-structure interaction.

5.1 Conclusions

5.1.1 Model

Results of the soil, structure and fluid domains can be obtained both in the time and the frequency domain. These include displacements and stresses at any location in the tank, fluid pressure on the tank at any location of the fluid-structure interface, the fluid surface elevation, the stresses and displacements at the soil-structure interface and displacements at the soil surface surrounding the tank. In addition, an earthquake signal can be applied in the model as traveling waves. The model is thus capable of producing output similar to numerical models, such as FE models, with the ease of use and computational efficiency comparable to other analytical models.

As the model's accuracy stems from the analytical nature of the model, each of the previously mentioned approximations needs to be limited. Therefore, the numbers of modes and elements were truncated such that additional modes or elements did not contribute substantially to the system's response. All discretizations showed convergence and changes were found of less than 3% for the addition of a number of modes. Only the soil-structure interface was slightly above that value, but truncated for practical purposes. Given the convergence of the model, it is concluded to be sufficiently accurate. A convergence check is however no replacement for a model validation, which still needs to be performed before the model can be applied in practice.

It is shown that dynamic soil-structure interaction is properly considered in the model, through a simple application of the usually known free-field ground motions in the equations of motion of the bottom plate. By considering all expected wave fields (free-field, scattered and radiated) associated with soil-structure interaction in the satisfaction of the conditions at the soil-structure interface, soil-structure interaction is properly accounted for.

5.1.2 Soil-structure interaction effects

For a fictitious case study, it was shown how the amount of damping of the tank-fluid system can be determined at each frequency of excitation. With the imaginary component of the dyanmic soil-stiffness matrix, the damping force for each element can be found. After transformation of the damping force and velocity to the time domain, the total amount of energy dissipated through the soil can be calculated for a given time domain. It can also be computed at each frequency over the time duration of one period and divided by the total amount of energy in the tank-fluid system. It then gives an indication of the effect of soil-structure interaction on system damping. Damping increases for frequencies above the cut-off frequency of the soil layer as radiation damping then starts to play a significant role.

The model was also applied to investigate the influence of the soil layer height, the soil type and tank dimensions on the fundamental period increase of the system. Both layer height and soil type were found to have substantial effects with an increase of approximately 1.7 times for a moderately stiff soil ($c_s = 270$m/s) and a h_s/R ratio of 6 and an increase of up to 4 for soft soil ($c_s = 120$m/s) with a h_s/R ratio of 4. These values were comparable to those reported by Larkin (2008) for a tank of similar dimensions.
In addition, it was found that larger tanks with the same h_s/R ratio tend to experience a smaller period increase. This is not surprising as structures with larger foundations experience stiffer soil behavior. The difference in the increase of the effective stiffness and the increase of the eigenperiod is related to the aproportional changes in the mass and stiffness of the tank-fluid system itself.
Finally, the dynamic soil stiffness model was compared to a modified static Winkler model consisting of horizontal and vertical uncoupled springs and dashpots. For softer soils with a greater layer thickness, higher discrepancies were observed. Two main model differences cause this effect. First, as concluded by Molenkamp (2018), there is a difference in effective stiffness at the edge and at the center of the interface, which becomes greater for softer soils. This is not included in the modified Winkler model. Second, the frequency dependent stiffness and damping were shown to have an effect on the results of the dynamic soil stiffness model, which is also not incorporated in the static modified Winkler model. The extent to which either of these model differences influences the observed response differences could be investigated further by eliminating one of the model differences, for example with a rigid tank bottom plate. From the analyses it can be concluded that soil-structure interaction should not only be considered properly for structures founded on very soft soils, but also on moderately dense soils.

5.2 Discussion and recommendations

A fundamental limitation of the model is that it is linear and that nonlinear effects can therefore not be included. Neither large displacements and strains of the tank itself can modeled, nor nonlinear failure mechanisms, such as buckling. Nonlinearities in the soil include stress-strain relations, sliding effects, nonlinear damping-strain relations and the inability to withstand tensile stresses other than some possible cohesion effects. However, this limitation does not disqualify the model. For example, stresses in the tank can still be calculated to compare to buckling stresses and modeling soil as an elastic continuum is widely adopted in seismic engineering and is considered accurate enough to describe the relevant physical phenomena, such as seismic wave propagation (Achenbach (2003); Aki and Richards (2009)).

A recommendation to improve the practical applicability of the current model is to add a roof, ring stiffeners and anchors to the model. The roof and ring stiffeners are likely to influence the mode shapes of the tank and thus the response, while the anchors will allow modeling of tanks with higher aspect ratios. Although tanks with higher aspect ratios can in principle be modeled, they are very likely to experience uplift, which currently invalidates the model.
It is also recommended to implement the possbility of multiple soil layers. Soils are often composed of various layers with rather different properties and it allows a more accurate representation of the soil directly underneath the tank. It was found in the case study that a tank mode was excited with a high wavenumber, while this mode might be less dominant in practice, since the material directly below the tank is often made stiffer with soil improvements or even a concrete slab.
Furthermore, the computational efficiency of the model could be inmproved, for example by applying a different discretization method that reduces the size of the soil stiffness matrix. While the axisymmetric discretization offeres computational benefits, the large number of elements at the center of the interface does not improve the model accuracy. It is therefore recommended to develop a discretization that is axisymmetric but with fewer elements to reduce the size of the soil stiffness matrix.
Finally, the model needs to be validated by means other than convergence checks. Finite element models can be considered with proper inclusion of the fluid, structure and soil, although strictly speaking, both models could still differ from reality. Another possibility is therefore experimental validation. Performing at least one of these is essential for safe future application of the model.

Appendix A Shells

In this appendix, the eigenfunction expansions are found of the tank's bottom plate and wall segments, based on the work by Soedel (2005) and Tsouvalas (2006).

A.1 Shell eigenfunction expansion

A.1.1 Shell equations of motion

First order approximations of vibrations of thin walled shell elements are characterized by the following 5 general equations, also known as Love's equations (Soedel, 2005):

$$-\frac{\partial(N_{11}A_2)}{\partial\alpha_1}-\frac{\partial(N_{21}A_1)}{\partial\alpha_2}-N_{12}\frac{\partial A_1}{\partial\alpha_2}+N_{22}\frac{\partial A_2}{\partial\alpha_1}-A_1A_2\frac{Q_{13}}{R_1}+A_1A_2\rho h\ddot{u}_1=A_1A_2q_1 \quad (A.1)$$

$$-\frac{\partial(N_{12}A_2)}{\partial\alpha_1}-\frac{\partial(N_{22}A_1)}{\partial\alpha_2}-N_{21}\frac{\partial A_2}{\partial\alpha_1}+N_{11}\frac{\partial A_1}{\partial\alpha_2}-A_1A_2\frac{Q_{23}}{R_2}+A_1A_2\rho h\ddot{u}_2=A_1A_2q_2 \quad (A.2)$$

$$-\frac{\partial(Q_{13}A_2)}{\partial\alpha_1}-\frac{\partial(Q_{23}A_1)}{\partial\alpha_2}+A_1A_2\left(\frac{N_{11}}{R_1}+\frac{N_{22}}{R_2}\right)+A_1A_2\rho h\ddot{u}_3=A_1A_2q_3 \quad (A.3)$$

$$\frac{\partial(M_{11}A_2)}{\partial\alpha_1}+\frac{\partial(M_{21}A_1)}{\partial\alpha_2}+M_{12}\frac{\partial A_1}{\partial\alpha_2}-M_{22}\frac{\partial A_2}{\partial\alpha_1}-Q_{13}A_1A_2=0 \quad (A.4)$$

$$\frac{\partial(M_{12}A_2)}{\partial\alpha_1}+\frac{\partial(M_{22}A_1)}{\partial\alpha_2}+M_{21}\frac{\partial A_2}{\partial\alpha_1}-M_{11}\frac{\partial A_1}{\partial\alpha_2}-Q_{23}A_1A_2=0 \quad (A.5)$$

The terms α_1 and α_2 represent the two-dimensional curvilinear surface coordinates.
A_1 and A_2 are the so called fundamental form parameters, which are specific to the geometry under consideration. Their values are defined as

$$A_i=\left|\frac{\partial\bar{r}}{\partial\alpha_i}\right| \qquad i=1,2 \quad (A.6)$$

in which $\bar{r}$ is the position vector for each location P on the shell's neutral surface.
u_1, u_2 and u_3 represent the displacements in the curvilinear coordinate system, where the latter is the displacement normal to the shell's surface.
q_1, q_2 and q_3 are external forces acting in each degree of freedom.
The forcing terms N_{11}, N_{22}, N_{12}, N_{21}, M_{11}, M_{22}, M_{12} and M_{21} are expressed as (Tsouvalas, 2009)

$$N_{11}=\frac{Eh}{1-\nu^2}\left(\left(\frac{1}{A_1}\frac{\partial u_1}{\partial\alpha_1}+\frac{u_2}{A_1A_2}\frac{\partial A_1}{\partial\alpha_2}+\frac{u_3}{R_1}\right)+\nu\left(\frac{1}{A_2}\frac{\partial u_2}{\partial\alpha_2}+\frac{u_1}{A_1A_2}\frac{\partial A_2}{\partial\alpha_1}+\frac{u_3}{R_2}\right)\right) \quad (A.7)$$

$$N_{22}=\frac{Eh}{1-\nu^2}\left(\nu\left(\frac{1}{A_1}\frac{\partial u_1}{\partial\alpha_1}+\frac{u_2}{A_1A_2}\frac{\partial A_1}{\partial\alpha_2}+\frac{u_3}{R_1}\right)+\left(\frac{1}{A_2}\frac{\partial u_2}{\partial\alpha_2}+\frac{u_1}{A_1A_2}\frac{\partial A_2}{\partial\alpha_1}+\frac{u_3}{R_2}\right)\right) \quad (A.8)$$

$$N_{12}=N_{21}=\frac{Eh}{2(1+\nu)}\left(\frac{A_2}{A_1}\frac{\partial}{\partial\alpha_1}\left(\frac{u_2}{A_2}\right)+\frac{A_1}{A_2}\frac{\partial}{\partial\alpha_2}\left(\frac{u_1}{A_1}\right)\right) \quad (A.9)$$

$$M_{11}=\frac{Eh^3}{12(1-\nu^2)}\left[\left(\frac{1}{A_1}\frac{\partial\phi_1}{\partial\alpha_1}+\frac{\phi_2}{A_1A_2}\frac{\partial A_1}{\partial\alpha_2}\right)+\nu\left(\frac{1}{A_2}\frac{\partial\phi_2}{\partial\alpha_2}+\frac{\phi_1}{A_1A_2}\frac{\partial A_2}{\partial\alpha_1}\right)\right] \quad (A.10)$$

$$M_{22} = \frac{Eh^3}{12(1-\nu^2)} \left[\nu \left(\frac{1}{A_1} \frac{\partial \phi_1}{\partial \alpha_1} + \frac{\phi_2}{A_1 A_2} \frac{\partial A_1}{\partial \alpha_2} \right) + \left(\frac{1}{A_2} \frac{\partial \phi_2}{\partial \alpha_2} + \frac{\phi_1}{A_1 A_2} \frac{\partial A_2}{\partial \alpha_1} \right) \right] \tag{A.11}$$

$$M_{12} = M_{21} = \frac{Eh^3}{24(1+\nu)} \left[\frac{A_2}{A_1} \frac{\partial}{\partial \alpha_1} \left(\frac{\phi_2}{A_2} \right) + \frac{A_1}{A_2} \frac{\partial}{\partial \alpha_2} \left(\frac{\phi_1}{A_1} \right) \right] \tag{A.12}$$

in which

$$\phi_1 = \frac{u_1}{R_1} - \frac{1}{A_1} \frac{\partial u_3}{\partial \alpha_1} \tag{A.13}$$

$$\phi_2 = \frac{u_2}{R_2} - \frac{1}{A_2} \frac{\partial u_3}{\partial \alpha_2} \tag{A.14}$$

As such, the equations of motion are described in terms of known geometrical and material parameters and unknown displacements for each degree of freedom.
Kirchhoff's effective shear forces are (Soedel, p. 36-37):

$$V_{13} = Q_{13} + \frac{1}{A_2} \frac{\partial M_{12}}{\partial \alpha_2} \tag{A.15}$$

$$V_{23} = Q_{23} + \frac{1}{A_2} \frac{\partial M_{21}}{\partial \alpha_1} \tag{A.16}$$

$$T_{12} = N_{12} + \frac{M_{12}}{R_2} \tag{A.17}$$

$$T_{21} = N_{21} + \frac{M_{21}}{R_1} \tag{A.18}$$

A.1.2 Circular plate

For circular plates it is convenient to adopt a cylindrical coordinate system with r for the radial, θ for the circumferential and z for the vertical coordinate, so that:

$$\alpha_1 = r \qquad \alpha_2 = \theta \tag{A.19}$$

Plates are a special case of shells characterized by zero curvature at each location, so $1/R_r = 0$ and $1/R_\theta = 0$. The position vector of the circular plate, $\bar{r}$, is defined as

$$\bar{r} = r \cos\theta \bar{e}_1 + r \sin\theta \bar{e}_2 \tag{A.20}$$

Substitution of equations (A.19) and (A.20) into equation (A.6) results in

$$A_1 = 1 \qquad A_2 = r \tag{A.21}$$

With equations (A.19) and (A.21) Love's equations (equations (A.1) to (A.5)) can be reduced to:

$$-\frac{\partial (N_{rr} r)}{\partial r} - \frac{\partial (N_{\theta r})}{\partial \theta} + N_{\theta\theta} + r\rho h \ddot{u}_r = r q_r \tag{A.22}$$

$$-\frac{\partial (N_{r\theta} r)}{\partial r} - \frac{\partial (N_{\theta\theta})}{\partial \theta} - N_{\theta r} + r\rho h \ddot{u}_\theta = r q_\theta \tag{A.23}$$

$$-\frac{\partial (Q_{rz} r)}{\partial r} - \frac{\partial (Q_{\theta z})}{\partial \theta} + r\rho h \ddot{u}_z = r q_z \tag{A.24}$$

$$\frac{\partial(M_{rr}r)}{\partial r} + \frac{\partial(M_{\theta r})}{\partial \theta} - M_{\theta\theta} - Q_{rz}r = 0 \tag{A.25}$$

$$\frac{\partial(M_{r\theta}r)}{\partial r} + \frac{\partial(M_{\theta\theta})}{\partial \theta} + M_{\theta r} - Q_{\theta z}r = 0 \tag{A.26}$$

in which $u_z = u_z(r,\theta,t)$, $u_\theta = u_\theta(r,\theta,t)$ and $u_r = u_r(r,\theta,t)$. Equations (A.22) to (A.24) show that the degrees of freedom in radial and circumferential direction are uncoupled from the degree of freedom in the vertical direction.

$$N_{rr} = \frac{Eh}{1-\nu^2}\left[\frac{\partial u_r}{\partial r} + \nu\left(\frac{1}{r}\frac{\partial u_\theta}{\partial \theta} + \frac{u_r}{r}\right)\right] \tag{A.27}$$

$$N_{\theta\theta} = \frac{Eh}{1-\nu^2}\left[\nu\frac{\partial u_r}{\partial r} + \left(\frac{1}{r}\frac{\partial u_\theta}{\partial \theta} + \frac{u_r}{r}\right)\right] \tag{A.28}$$

$$N_{r\theta} = N_{\theta r} = \frac{Eh}{2(1+\nu)}\left[-\frac{1}{r}u_\theta + \frac{\partial u_\theta}{\partial r} + \frac{1}{r}\frac{\partial u_r}{\partial \theta}\right] \tag{A.29}$$

$$M_{rr} = \frac{Eh^3}{12(1-\nu^2)}\left[\frac{\partial \phi_r}{\partial r} + \nu\left(\frac{1}{r}\frac{\partial \phi_\theta}{\partial \theta} + \frac{\phi_r}{r}\right)\right] \tag{A.30}$$

$$M_{\theta\theta} = \frac{Eh^3}{12(1-\nu^2)}\left[\nu\frac{\partial \phi_r}{\partial r} + \left(\frac{1}{r}\frac{\partial \phi_\theta}{\partial \theta} + \frac{\phi_r}{r}\right)\right] \tag{A.31}$$

$$M_{r\theta} = M_{\theta r} = \frac{Eh^3}{24(1+\nu)}\left[r\frac{\partial}{\partial r}\left(\frac{\phi_\theta}{r}\right) + \frac{1}{r}\frac{\partial \phi_r}{\partial \theta}\right] \tag{A.32}$$

in which

$$\phi_r = -\frac{\partial u_z}{\partial r} \tag{A.33}$$

$$\phi_\theta = -\frac{1}{r}\frac{\partial u_z}{\partial \theta} \tag{A.34}$$

By substitution of equations (A.33) and (A.34), equations (A.30) to (A.32) can be further reduced to

$$M_{rr} = -\frac{Eh^3}{12(1-\nu^2)}\left[\frac{\partial^2 u_z}{\partial r^2} + \nu\left(\frac{1}{r^2}\frac{\partial^2 u_z}{\partial \theta^2} + \frac{1}{r}\frac{\partial u_z}{\partial r}\right)\right] \tag{A.35}$$

$$M_{\theta\theta} = -\frac{Eh^3}{12(1-\nu^2)}\left[\nu\frac{\partial^2 u_z}{\partial r^2} + \left(\frac{1}{r^2}\frac{\partial^2 u_z}{\partial \theta^2} + \frac{1}{r}\frac{\partial u_z}{\partial r}\right)\right] \tag{A.36}$$

$$M_{r\theta} = M_{\theta r} = -(1-\nu)\frac{Eh^3}{12(1-\nu^2)}\frac{\partial}{\partial r}\left(\frac{1}{r}\frac{\partial u_z}{\partial \theta}\right) \tag{A.37}$$

Expressions for the terms Q_{rz} and $Q_{\theta z}$ in the third equation of motion (equation (A.24)) can be found by rewriting equations (A.25) and (A.26):

$$Q_{rz} = \frac{1}{r}\left[\frac{\partial(M_{rr}r)}{\partial r} + \frac{\partial(M_{\theta r})}{\partial \theta} - M_{\theta\theta}\right] \tag{A.38}$$

$$Q_{\theta z} = \frac{1}{r}\left[\frac{\partial(M_{r\theta}r)}{\partial r} + \frac{\partial(M_{\theta\theta})}{\partial\theta} + M_{\theta r}\right] \tag{A.39}$$

Substitution of equations (A.35) to (A.37) into equations (A.38) and (A.39) gives

$$\begin{aligned} Q_{rz} = &-\frac{1}{r}\frac{Eh^3}{12(1-\nu^2)}\left[\frac{\partial^2 u_z}{\partial r^2} + r\frac{\partial^3 u_z}{\partial r^3} + \nu\left(-\frac{1}{r^2}\frac{\partial^2 u_z}{\partial\theta^2} + \frac{1}{r}\frac{\partial^3 u_z}{\partial r\partial\theta^2} + \frac{\partial^2 u_z}{\partial r^2}\right)\right] \\ &-(1-\nu)\frac{1}{r}\frac{Eh^3}{12(1-\nu^2)}\left(-\frac{1}{r^2}\frac{\partial^2 u_z}{\partial\theta^2} + \frac{1}{r}\frac{\partial^3 u_z}{\partial r\partial\theta^2}\right) + \frac{1}{r}\frac{Eh^3}{12(1-\nu^2)}\left[\nu\frac{\partial^2 u_z}{\partial r^2} + \frac{1}{r^2}\frac{\partial^2 u_z}{\partial\theta^2} + \frac{1}{r}\frac{\partial u_z}{\partial r}\right] \\ &= -\frac{1}{r}\frac{Eh^3}{12(1-\nu^2)}\left(\frac{\partial^2 u_z}{\partial r^2} + r\frac{\partial^3 u_z}{\partial r^3} - \frac{2}{r^2}\frac{\partial^2 u_z}{\partial\theta^2} + \frac{1}{r}\frac{\partial^3 u_z}{\partial r\partial\theta^2} - \frac{1}{r}\frac{\partial u_z}{\partial r}\right) \end{aligned} \tag{A.40}$$

$$\begin{aligned} Q_{\theta z} = &\frac{1}{r}\left[-(1-\nu)\frac{Eh^3}{12(1-\nu^2)}\left(\frac{1}{r^2}\frac{\partial u_z}{\partial\theta} - \frac{1}{r}\frac{\partial^2 u_z}{\partial r\partial\theta} + \frac{\partial^3 u_z}{\partial r^2\partial\theta}\right) - \right. \\ &\left.\frac{Eh^3}{12(1-\nu^2)}\left(\nu\frac{\partial^3 u_z}{\partial r^2\partial\theta} + \frac{1}{r^2}\frac{\partial^3 u_z}{\partial\theta^3} + \frac{1}{r}\frac{\partial^2 u_z}{\partial r\partial\theta}\right) + (1-\nu)\frac{Eh^3}{12(1-\nu^2)}\left(\frac{1}{r^2}\frac{\partial u_z}{\partial\theta} - \frac{1}{r}\frac{\partial^2 u_z}{\partial r\partial\theta}\right)\right] \\ &= -\frac{Eh^3}{12(1-\nu^2)}\left(\frac{1}{r^3}\frac{\partial^3 u_z}{\partial\theta^3} + \frac{1}{r^2}\frac{\partial^2 u_z}{\partial r\partial\theta} + \frac{1}{r}\frac{\partial^3 u_z}{\partial r^2\partial\theta}\right) \end{aligned} \tag{A.41}$$

To express the equations of motion in terms of displacements and their derivatives, and material and geometrical properties, the force expressions (equations (A.27) to (A.29), (A.35) to (A.37), (A.40) and (A.41)) are substituted in the equations of motion (equations (A.22) to (A.24)):

$$\begin{aligned} -\frac{Eh}{1-\nu^2}\frac{1}{r}\left(\frac{1-\nu}{2}\frac{\partial^2 u_r}{\partial\theta^2} + r\frac{1+\nu}{2}\frac{\partial^2 u_\theta}{\partial r\partial\theta} + r^2\frac{\partial^2 u_r}{\partial r^2} - \frac{1-\nu}{2}\frac{\partial u_\theta}{\partial\theta}\right. \\ \left. - \frac{\partial u_\theta}{\partial\theta} + r\frac{\partial u_r}{\partial r} - u_r\right) + r\rho h\ddot{u}_r = rq_r \end{aligned} \tag{A.42}$$

$$\begin{aligned} -\frac{Eh}{1-\nu^2}\frac{1}{r}\left(\frac{\partial^2 u_\theta}{\partial\theta^2} + r\frac{1+\nu}{2}\frac{\partial^2 u_r}{\partial r\partial\theta} + r^2\frac{1-\nu}{2}\frac{\partial^2 u_\theta}{\partial r^2} + \frac{1-\nu}{2}\frac{\partial u_r}{\partial\theta}\right. \\ \left. + \frac{\partial u_r}{\partial\theta} + r\frac{1-\nu}{2}\frac{\partial u_\theta}{\partial r} - \frac{1-\nu}{2}u_\theta\right) + r\rho h\ddot{u}_\theta = rq_\theta \end{aligned} \tag{A.43}$$

$$\begin{aligned} \frac{Eh^3}{12(1-\nu^2)}\left(2\frac{\partial^3 u_z}{\partial r^3} + r\frac{\partial^4 u_z}{\partial r^4} - \frac{2}{r^2}\frac{\partial^3 u_z}{\partial r\partial\theta^2} + \frac{4}{r^3}\frac{\partial^2 u_z}{\partial\theta^2} + \frac{2}{r}\frac{\partial^4 u_z}{\partial r^2\partial\theta^2}\right. \\ \left. - \frac{1}{r}\frac{\partial^2 u_z}{\partial r^2} + \frac{1}{r^2}\frac{\partial u_z}{\partial r} + \frac{1}{r^3}\frac{\partial^4 u_z}{\partial\theta^4}\right) + r\rho h\ddot{u}_z = rq_z \end{aligned} \tag{A.44}$$

Realizing that

$$\nabla^4 = \frac{\partial^4}{\partial r^4} + \frac{2}{r}\frac{\partial^3}{\partial r^3} - \frac{1}{r^2}\frac{\partial^2}{\partial r^2} + \frac{1}{r^3}\frac{\partial}{\partial r} + \frac{2}{r^2}\frac{\partial^4}{\partial r^2 \partial \theta^2} - \frac{2}{r^3}\frac{\partial^3}{\partial r \partial \theta^2} + \frac{4}{r^4}\frac{\partial^2}{\partial \theta^2} + \frac{1}{r^4}\frac{\partial^4}{\partial \theta^4} \tag{A.45}$$

equation (A.44) can be rewritten as

$$D\nabla^4 u_z + \rho h \ddot{u}_z = q_z \tag{A.46}$$

in which

$$D = \frac{Eh^3}{12(1-\nu^2)} \tag{A.47}$$

To find the eigenfrequencies and eigenwavenumbers of the plate, the free vibration (homogeneous equation) is analyzed. The two coupled equations of motion in radial and circumferential direction are studied separately from the one in vertical direction. For the latter, the method of separation of variables is applied. The function $u_z(r,\theta,t)$ is written as a multiplication of three functions dependent on just one variable each. For the function related to time, an exponential function is tried, implying that the plate is expected to vibrate harmonically in time.

$$u_z(r,\theta,t) = R(r)\Theta(\theta)\exp(\mathrm{i}\omega t) \tag{A.48}$$

Substitution of equation (A.48) into equation (A.46) and division by $\exp(\mathrm{i}\omega t)$ results in

$$\nabla^4 R(r)\Theta(\theta) - \lambda^4 R(r)\Theta(\theta) = 0 \tag{A.49}$$

in which

$$\lambda^4 = \frac{\omega^2 \rho h}{D} \tag{A.50}$$

Equation (A.49) can be rewritten as

$$(\nabla^2 + \lambda^2)(\nabla^2 - \lambda^2)R(r)\Theta(\theta) = 0 \tag{A.51}$$

which holds for every solution of

$$(\nabla^2 \pm \lambda^2)R(r)\Theta(\theta) = 0 \tag{A.52}$$

Substituting

$$\nabla^2 = \frac{\partial^2}{\partial r^2} + \frac{1}{r}\frac{\partial}{\partial r} + \frac{1}{r^2}\frac{\partial^2}{\partial \theta^2} \tag{A.53}$$

gives

$$\frac{\mathrm{d}^2 R(r)}{\mathrm{d}r^2}\Theta(\theta) + \frac{1}{r}\frac{\mathrm{d}R(r)}{\mathrm{d}r}\Theta(\theta) + \frac{R(r)}{r^2}\frac{\mathrm{d}^2\Theta(\theta)}{\mathrm{d}\theta^2} \pm \lambda^2 R(r)\Theta(\theta) = 0 \tag{A.54}$$

Division by $R(r)\Theta(\theta)$ and multiplication with r^2 finally separates the functions related to both coordinates:

$$r^2\left[\frac{1}{R(r)}\left(\frac{\mathrm{d}^2 R(r)}{\mathrm{d}r^2} + \frac{1}{r}\frac{\mathrm{d}R(r)}{\mathrm{d}r}\right) \pm \lambda^2\right] = -\frac{1}{\Theta(\theta)}\frac{\mathrm{d}^2\Theta(\theta)}{\mathrm{d}\theta^2} \tag{A.55}$$

This equation can only hold if both sides of the equation are equal to a constant, which is called k^2 here. Then

$$-\frac{1}{\Theta(\theta)}\frac{\mathrm{d}^2\Theta(\theta)}{\mathrm{d}\theta^2} = k^2 \tag{A.56}$$

and

$$r^2\left[\frac{1}{R(r)}\left(\frac{\mathrm{d}^2R(r)}{\mathrm{d}r^2}+\frac{1}{r}\frac{\mathrm{d}R(r)}{\mathrm{d}r}\right)\pm\lambda^2\right]=k^2 \tag{A.57}$$

which are both uncoupled ordinary differential equations. In a more common form, equation (A.56) is:

$$\frac{\mathrm{d}^2\Theta(\theta)}{\mathrm{d}\theta^2}+k^2\Theta(\theta)=0 \tag{A.58}$$

The general solution to this equation is

$$\Theta(\theta)=A\cos(k\theta)+B\sin(k\theta)=C\cos(k(\theta+\phi)) \tag{A.59}$$

Since the vertical displacement of the plate is continuous in the circumferential direction, it must hold that $\Theta(0)=\Theta(2\pi)$. From equation (A.59) it can then be seen that k must be an integer, denoted from now on as n $(=0,1,2,...,\infty)$. Noting also the role of this function in equation (A.48) as prescribing the variation of u_z in circumferential direction, it can be regarded as the circumferential vibration mode with wavenumber n.
The constant angle ϕ will be omitted from here onward, because it only indicates the orientation of the plate's displacement pattern with respect to the orientation of the selected coordinate system. It does not influence the physical behavior of the plate, nor its interaction with an external force, since the latter's direction is also an arbitrary choice with respect to ϕ.
Rewriting equation (A.57) to

$$r^2\frac{\mathrm{d}^2R(r)}{\mathrm{d}r^2}+r\frac{\mathrm{d}R(r)}{\mathrm{d}r}+(\pm\lambda^2r^2-k^2)R(r)=0 \tag{A.60}$$

more clearly shows that it is similar to Bessel's differential equation, except for the term λ^2r^2. In order to obtain Bessel's differential equation, the following substitution is made:

$$\xi=\sqrt{\pm\lambda^2r^2}=r\sqrt{\pm\lambda^2}\qquad\rightarrow\qquad\frac{\partial\xi}{\partial r}=\sqrt{\pm\lambda^2} \tag{A.61}$$

Through substitution of equation (A.61), equation (A.60) is

$$\begin{aligned}&\frac{\xi^2}{\pm\lambda^2}\frac{\mathrm{d}}{\mathrm{d}r}\left(\frac{\mathrm{d}R(\xi)}{\mathrm{d}\xi}\frac{\mathrm{d}\xi}{\mathrm{d}r}\right)+\frac{\xi}{\sqrt{\pm\lambda^2}}\frac{\mathrm{d}R(\xi)}{\mathrm{d}\xi}\frac{\mathrm{d}\xi}{\mathrm{d}r}+(\xi^2-k^2)R(\xi)\\ =&\sqrt{\pm\lambda^2}\frac{\xi^2}{\pm\lambda^2}\frac{\mathrm{d}}{\mathrm{d}\xi}\left(\frac{\mathrm{d}R(\xi)}{\mathrm{d}\xi}\frac{\mathrm{d}\xi}{\mathrm{d}r}\right)+\xi\frac{\mathrm{d}R(\xi)}{\mathrm{d}\xi}+(\xi^2-k^2)R(\xi)\\ =&\xi^2\frac{\mathrm{d}^2R(\xi)}{\mathrm{d}\xi^2}+\xi\frac{\mathrm{d}R(\xi)}{\mathrm{d}\xi}+(\xi^2-k^2)R(\xi)=0\end{aligned} \tag{A.62}$$

The solutions to Bessel's differential equation are Bessel functions, the definitions of which depend on the circumstances, but are in all cases an infinite series expansion. Since Bessel's differential equation is of the second order, the solution consists of two linearly independent functions.
For real values of ξ, the solution is a Bessel of the first kind and of the order k (in the above equation), denoted as $J_k(\lambda r)$. While in general $J_k(\lambda r)$ and $J_{-k}(\lambda r)$ are independent functions and therefore the two solutions to equation (A.62), the value of k was in this case

determined to be of integer value. $J_n(\lambda r)$ and $J_{-n}(\lambda r)$ (in which n is an integer) are not independent and the second solution is then the Bessel function of the second kind, $Y_n(\lambda r)$. For complex values of ξ, the solutions to Bessel's differential equation are the modified Bessel functions or the first and second kind, denoted by $I_n(\lambda r)$ and $K_n(\lambda r)$ respectively.
The entire solution to equation (A.62), for both complex and real values of ξ, is then

$$R(\lambda r) = DJ_n(\lambda r) + EY_n(\lambda r) + FI_n(\lambda r) + GK_n(\lambda r) \tag{A.63}$$

As we know that

$$\lim_{\lambda r \to 0} Y_n(\lambda r) = \lim_{\lambda r \to 0} K_n(\lambda r) = \infty \tag{A.64}$$

and that at $r = 0$, $u_z \neq \infty$, it can be concluded that $E = G = 0$.
Finally substituting equations (A.59) and (A.63) into equation (A.48) and writing the expression as an infinite sum of modes that are excited at the natural frequencies of the plate:

$$u_z(r,\theta,t) = \sum_{m=0}^{\infty}\sum_{n=0}^{\infty}\left[A_{nm}J_n(k_{mn}r) + B_{nm}I_n(k_{mn}r)\right]\cos(n\theta)\exp(\mathrm{i}\omega_{nm}t) \tag{A.65}$$

in which, in accordance with equation (A.50),

$$\lambda_{mn}^4 = \frac{\omega_{mn}^2 \rho h}{D} \tag{A.66}$$

Note that the natural frequencies in the case of the tank are not of the plate by itself, but the natural frequencies of the entire tank. These can be found by substituting the modal expressions of each part of the tank into boundary and interface conditions and solving that eigenvalue problem.

Considering the free vibrations of the plate in the in plane coordinates r and θ, the plate is assumed to vibrate harmonically, so that

$$u_r(r,\theta,t) = U_r(r,\theta)\exp(\mathrm{i}\omega t) \qquad \text{and} \qquad u_\theta(r,\theta,t) = U_\theta(r,\theta)\exp(\mathrm{i}\omega t) \tag{A.67}$$

Substitution of equation (A.67) into the equations of motion (equations (A.42) and (A.43)) and division by r gives

$$-K\frac{1}{r^2}\left(r\frac{1+\nu}{2}\frac{\partial^2 U_\theta}{\partial r\partial\theta} + r^2\frac{\partial^2 U_r}{\partial r^2} - \frac{\partial U_\theta}{\partial\theta} + r\frac{\partial U_r}{\partial r} - U_r\right) - G\frac{1}{r^2}\left(\frac{\partial^2 U_r}{\partial\theta^2} - \frac{\partial U_\theta}{\partial\theta}\right) - \omega^2\rho h U_r = 0 \tag{A.68}$$

$$-K\frac{1}{r^2}\left(\frac{\partial^2 U_\theta}{\partial\theta^2} + r\frac{1+\nu}{2}\frac{\partial^2 U_r}{\partial r\partial\theta} + \frac{\partial U_r}{\partial\theta}\right) - G\frac{1}{r^2}\left(r^2\frac{\partial^2 U_\theta}{\partial r^2} + \frac{\partial U_r}{\partial\theta} + r\frac{\partial U_\theta}{\partial r} - U_\theta\right) - \omega^2\rho h U_\theta = 0 \tag{A.69}$$

in which

$$K = \frac{Eh}{1-\nu^2} \qquad \text{and} \qquad G = \frac{Eh}{2(1+\nu)} \tag{A.70}$$

Introducing next the displacement potential functions (similar to Senjanović (2014))

$$\begin{aligned} U_r(r,\theta) &= \frac{\partial \Phi}{\partial r} + \frac{1}{r}\frac{\partial \Psi}{\partial \theta} \\ U_\theta(r,\theta) &= \frac{1}{r}\frac{\partial \Phi}{\partial \theta} - \frac{\partial \Psi}{\partial r} \end{aligned} \tag{A.71}$$

and substituting those into equations (A.68) and (A.69) results in

$$\begin{aligned} \frac{1}{r^2}\Bigg(&-\left(K\frac{\nu+1}{2}+G\right)\frac{\partial^3\Phi}{\partial r\partial\theta^2} + Kr\frac{\nu-1}{2}\frac{\partial^3\Psi}{\partial r^2\partial\theta} - G\frac{1}{r}\frac{\partial^3\Psi}{\partial\theta^3} - Kr^2\frac{\partial^3\Phi}{\partial r^3} \\ &+\frac{1}{r}\left(K\frac{\nu+3}{2}+G\right)\frac{\partial^2\Phi}{\partial\theta^2} - G\frac{\partial^2\Psi}{\partial r\partial\theta} - Kr\frac{\partial^2\Phi}{\partial r^2} - \left(r^2\omega^2\rho h - K\right)\frac{\partial\Phi}{\partial r} - \frac{\partial\Psi}{\partial\theta}r\omega^2\rho h\Bigg) \end{aligned} \tag{A.72}$$

$$\begin{aligned} \frac{1}{r^2}\Bigg(&-\left(K\frac{\nu+1}{2}+G\right)r\frac{\partial^3\Phi}{\partial r^2\partial\theta} - K\frac{\nu-1}{2}\frac{\partial^3\Psi}{\partial r\partial\theta^2} - K\frac{1}{r}\frac{\partial^3\Phi}{\partial\theta^3} + Gr^2\frac{\partial^3\Psi}{\partial r^3} \\ &+\frac{1}{r}\left(K\frac{\nu-1}{2}-G\right)\frac{\partial^2\Psi}{\partial\theta^2} - K\frac{\partial^2\Phi}{\partial r\partial\theta} + Gr\frac{\partial^2\Psi}{\partial r^2} - \left(r^2\omega^2\rho h + G\right)\frac{\partial\Psi}{\partial r} - \frac{\partial\Phi}{\partial\theta}r\omega^2\rho h\Bigg) \end{aligned} \tag{A.73}$$

Summing the derivative of equation (A.72) with respect to r and the derivative of equation (A.73) with respect to θ divided by r results in

$$\begin{aligned} \frac{Eh}{1-v^2}\Bigg(&-\frac{1}{r^4}\frac{\partial^4\Phi}{\partial\theta^4} - \frac{2}{r^2}\frac{\partial^4\Phi}{\partial r^2\partial\theta^2} - \frac{\partial^4\Phi}{\partial r^4} + \frac{2}{r^3}\frac{\partial^3\Phi}{\partial r\partial\theta^2} - \frac{2}{r}\frac{\partial^3\Phi}{\partial r^3} \\ &-\frac{4}{r^4}\frac{\partial^2\Phi}{\partial\theta^2} + \frac{1}{r^2}\frac{\partial^2\Phi}{\partial r^2} - \frac{1}{r^3}\frac{\partial\Phi}{\partial r}\Bigg) - \omega^2\rho h\left(\frac{1}{r^2}\frac{\partial^2\Phi}{\partial\theta^2} + \frac{\partial^2\Phi}{\partial r^2} + \frac{1}{r}\frac{\partial\Phi}{\partial r}\right) = 0 \end{aligned} \tag{A.74}$$

Recognizing the presence of the squared Laplace operator as given in equation (A.45), equation (A.74) can be written as

$$K\nabla^2\Phi + \omega^2\rho h\Phi = 0 \tag{A.75}$$

Subtracting the derivative of equation (A.73) with respect to r from the derivative of equation (A.72) divided by r results in

$$\begin{aligned} \frac{Eh}{2(1+v)}\Bigg(&-\frac{1}{r^4}\frac{\partial^4\Psi}{\partial\theta^4} - \frac{2}{r^2}\frac{\partial^4\Psi}{\partial r^2\partial\theta^2} - \frac{\partial^4\Psi}{\partial r^4} + \frac{2}{r^3}\frac{\partial^3\Psi}{\partial r\partial\theta^2} - \frac{2}{r}\frac{\partial^3\Psi}{\partial r^3} + \\ &-\frac{4}{r^4}\frac{\partial^2\Psi}{\partial\theta^2} + \frac{1}{r^2}\frac{\partial^2\Psi}{\partial r^2} - \frac{1}{r^3}\frac{\partial\Psi}{\partial r}\Bigg) - \omega^2\rho h\left(\frac{1}{r^2}\frac{\partial^2\Psi}{\partial\theta^2} + \frac{\partial^2\Psi}{\partial r^2} + \frac{1}{r}\frac{\partial\Psi}{\partial r}\right) = 0 \end{aligned} \tag{A.76}$$

Recognizing again the presence of the squared Laplace operator as given in equation (A.45), equation (A.76) can be written as

$$G\nabla^2\Psi + \omega^2\rho h\Psi = 0 \tag{A.77}$$

The equations are now uncoupled and can be solved separately. For both potential functions the separation of variables method is applied, as was done for the out of plane case, so that

$$\begin{aligned}\Phi(r,\theta) &= \Theta_\Phi(\theta)R_\Phi(r)\\ \Psi(r,\theta) &= \Theta_\Psi(\theta)R_\Psi(r)\end{aligned} \tag{A.78}$$

Substituting the written out Laplace operator (equation (A.53)) and equation (A.78) into the equations of motion (equations (A.75) and (A.77)) results in

$$\begin{aligned}\frac{\mathrm{d}^2R_\Phi}{\mathrm{d}r^2}\Theta_\Phi + \frac{1}{r}\frac{\mathrm{d}R_\Phi}{\mathrm{d}r}\Theta_\Phi + \frac{R_\Phi}{r^2}\frac{\mathrm{d}^2\Theta_\Phi}{\mathrm{d}\theta^2} + \lambda_\Phi^2 R_\Phi\Theta_\Phi = 0\\ \frac{\mathrm{d}^2R_\Psi}{\mathrm{d}r^2}\Theta_\Psi + \frac{1}{r}\frac{\mathrm{d}R_\Psi}{\mathrm{d}r}\Theta_\Psi + \frac{R_\Psi}{r^2}\frac{\mathrm{d}^2\Theta_\Psi}{\mathrm{d}\theta^2} + \lambda_\Psi^2 R_\Psi\Theta_\Psi = 0\end{aligned} \tag{A.79}$$

in which

$$\begin{aligned}\lambda_\Phi^2 &= \frac{\omega^2\rho h}{K}\\ \lambda_\Psi^2 &= \frac{\omega^2\rho h}{G}\end{aligned} \tag{A.80}$$

Division by $R_\Phi\Theta_\Phi$ and $R_\Psi\Theta_\Psi$ respectively and multiplication both equations with r^2, separates the functions related to both coordinates:

$$\begin{aligned}r^2\left[\frac{1}{R_\Phi}\left(\frac{\mathrm{d}^2R_\Phi}{\mathrm{d}r^2} + \frac{1}{r}\frac{\mathrm{d}R_\Phi}{\mathrm{d}r}\right) + \lambda_\Phi^2\right] &= -\frac{1}{\Theta_\Phi}\frac{\mathrm{d}^2\Theta_\Phi}{\mathrm{d}\theta^2}\\ r^2\left[\frac{1}{R_\Psi}\left(\frac{\mathrm{d}^2R_\Psi}{\mathrm{d}r^2} + \frac{1}{r}\frac{\mathrm{d}R_\Psi}{\mathrm{d}r}\right) + \lambda_\Psi^2\right] &= -\frac{1}{\Theta_\Psi}\frac{\mathrm{d}^2\Theta_\Psi}{\mathrm{d}\theta^2}\end{aligned} \tag{A.81}$$

Following the same reasoning as for the out of plane vibration, the phases of the general solutions (equation (A.59)) of the functions $\Theta_\Phi(\theta)$ and $\Theta_\Psi(\theta)$ can arbitrarily chosen, so that the final solutions are

$$\begin{aligned}\Theta_\Phi(\theta) &= A_\Phi\cos(n\theta)\\ \Theta_\Psi(\theta) &= A_\Psi\sin(n\theta)\end{aligned} \tag{A.82}$$

The left hand side of equation (A.81) can be written in an manner similar to equation (A.60):

$$\begin{aligned}r^2\tfrac{\mathrm{d}^2R_\Phi}{\mathrm{d}r^2} + r\tfrac{\mathrm{d}R_\Phi}{\mathrm{d}r} + \lambda_\Phi^2r^2 - k^2R_\Phi = 0\\ r^2\tfrac{\mathrm{d}^2R_\Psi}{\mathrm{d}r^2} + r\tfrac{\mathrm{d}R_\Psi}{\mathrm{d}r} + \lambda_\Psi^2r^2 - k^2R_\Psi = 0\end{aligned} \tag{A.83}$$

Following the same reasoning, the same solution is found (equations (A.63) and (A.64)), apart from the constants and wavenumbers. In addition, the modified Bessel functions are omitted, as $\lambda_\Phi r$ and $\lambda_\Psi r$ will be real-valued. The solutions for the potential functions in the radial coordinate are thus

$$\begin{aligned}R_\Phi(\lambda_\Phi r) &= B_\Phi J_n(\lambda_\Phi r)\\ R_\Psi(\lambda_\Psi r) &= B_\Psi J_n(\lambda_\Psi r)\end{aligned} \tag{A.84}$$

Substituting equations (A.82) and (A.84) into equation (A.80) and substituting the result into equation (A.71) gives

$$\begin{aligned} U_r(r,\theta) &= A_\Phi \cos(n\theta) B_\Phi \frac{\partial J_n(\lambda_\Phi r)}{\partial r} + \frac{n}{r} A_\Psi \cos(n\theta) B_\Psi J_n(\lambda_\Psi r) \\ U_\theta(r,\theta) &= -\frac{n}{r} A_\Phi \sin(n\theta) B_\Phi J_n(\lambda_\Phi r) - A_\Psi \sin(n\theta) B_\Psi \frac{\partial J_n(\lambda_\Psi r)}{\partial r} \end{aligned} \tag{A.85}$$

Since A_Φ, A_Ψ, B_Φ and B_Ψ are arbitrary constants, they can be replaced by others. Finally substituting equation (A.85) into equation (A.67) and writing the expression as an infinite sum of modes that are excited at the natural frequencies of the plate:

$$\begin{aligned} u_r(r,\theta,t) &= \sum_{m=0}^{\infty}\sum_{n=0}^{\infty} \left[C_{nm} \frac{\partial J_n(k_\Phi r)}{\partial r} + D_{nm} \frac{n}{r} J_n(k_\Psi r) \right] \cos(n\theta) \exp(\mathrm{i}\omega_{nm} t) \\ u_\theta(r,\theta,t) &= \sum_{m=0}^{\infty}\sum_{n=0}^{\infty} \left[-C_{nm} \frac{n}{r} J_n(k_\Phi r) - D_{nm} \frac{\partial J_n(k_\Psi r)}{\partial r} \right] \sin(n\theta) \exp(\mathrm{i}\omega_{nm} t) \end{aligned} \tag{A.86}$$

A.1.3 Cylindrical shell

For cylindrical shells it is convenient to adopt a cylindrical coordinate system with r for the radial, θ for the circumferential and z for the longitudinal coordinate, so that:

$$\alpha_1 = z \qquad \alpha_2 = \theta \tag{A.87}$$

Cylindrical shells are characterized by zero curvature along the z-coordinate and a radius of curvature along the circumferential coordinate equal to the radius R of the cylinder, so

$$1/R_1 = 0 \qquad 1/R_2 = 1/R \tag{A.88}$$

The position vector of the cylindrical shell, $\bar{r}$, is defined as

$$\bar{r} = z\bar{e}_1 + R\cos\theta\bar{e}_2 + R\sin\theta\bar{e}_3 \tag{A.89}$$

Substitution of equations (A.87) and (A.89) and into equation (A.6) results in

$$A_1 = 1 \qquad A_2 = R \tag{A.90}$$

Through substitution of equations (A.88) to (A.90) Love's equations (equations (A.1) to (A.5)) can be reduced to:

$$\frac{\partial N_{zz}}{\partial z} + \frac{1}{R}\frac{\partial N_{\theta z}}{\partial \theta} + q_z = \rho h \ddot{u}_z \tag{A.91}$$

$$\frac{\partial N_{z\theta}}{\partial z} + \frac{1}{R}\frac{\partial N_{\theta\theta}}{\partial \theta} + \frac{1}{R} Q_{\theta r} + q_\theta = \rho h \ddot{u}_\theta \tag{A.92}$$

$$\frac{\partial Q_{zr}}{\partial z} + \frac{1}{R}\frac{\partial Q_{\theta r}}{\partial \theta} - \frac{N_{\theta\theta}}{R} + q_r = \rho h \ddot{u}_r \tag{A.93}$$

$$\frac{\partial M_{zz}}{\partial z} + \frac{1}{R}\frac{\partial M_{\theta z}}{\partial \theta} = Q_{zr} \tag{A.94}$$

$$\frac{\partial M_{z\theta}}{\partial z} + \frac{1}{R}\frac{\partial M_{\theta\theta}}{\partial \theta} = Q_{\theta r} \tag{A.95}$$

in which $u_z = u_z(z,\theta,t)$, $u_\theta = u_\theta(z,\theta,t)$ and $u_r = u_r(z,\theta,t)$. Substitution of equations (A.87), (A.88) and (A.90) into equations (A.7) to (A.9), (A.13) and (A.14) gives

$$N_{zz} = \frac{Eh}{1-\nu^2}\left[\frac{\partial u_z}{\partial z} + \frac{\nu}{R}\left(\frac{\partial u_\theta}{\partial \theta} + u_r\right)\right] \tag{A.96}$$

$$N_{\theta\theta} = \frac{Eh}{1-\nu^2}\left[\nu\frac{\partial u_z}{\partial z} + \frac{1}{R}\left(\frac{\partial u_\theta}{\partial \theta} + u_r\right)\right] \tag{A.97}$$

$$N_{z\theta} = N_{\theta z} = \frac{Eh}{2(1+\nu)}\left[\frac{\partial u_\theta}{\partial z} + \frac{1}{R}\frac{\partial u_z}{\partial \theta}\right] \tag{A.98}$$

$$M_{zz} = \frac{Eh^3}{12(1-\nu^2)}\left[\frac{\partial \phi_z}{\partial z} + \frac{\nu}{R}\frac{\partial \phi_\theta}{\partial \theta}\right] \tag{A.99}$$

$$M_{\theta\theta} = \frac{Eh^3}{12(1-\nu^2)}\left[\nu\frac{\partial \phi_z}{\partial z} + \frac{1}{R}\frac{\partial \phi_\theta}{\partial \theta}\right] \tag{A.100}$$

$$M_{z\theta} = M_{\theta z} = \frac{Eh^3}{24(1+\nu)}\left[R\frac{\partial}{\partial z}\left(\frac{\phi_\theta}{R}\right) + \frac{1}{R}\frac{\partial \phi_z}{\partial \theta}\right] \tag{A.101}$$

in which

$$\phi_z = -\frac{\partial u_r}{\partial z} \tag{A.102}$$

$$\phi_\theta = \frac{u_\theta}{R} - \frac{1}{R}\frac{\partial u_r}{\partial \theta} \tag{A.103}$$

By substitution of equations (A.102) and (A.103), equations (A.99) to (A.101) can be further reduced to

$$M_{zz} = D\left[-\frac{\partial^2 u_r}{\partial z^2} + \frac{\nu}{R^2}\left(\frac{\partial u_\theta}{\partial \theta} - \frac{\partial^2 u_r}{\partial \theta^2}\right)\right] \tag{A.104}$$

$$M_{\theta\theta} = D\left[-\nu\frac{\partial^2 u_r}{\partial z^2} + \frac{1}{R^2}\left(\frac{\partial u_\theta}{\partial \theta} - \frac{\partial^2 u_r}{\partial \theta^2}\right)\right] \tag{A.105}$$

$$M_{z\theta} = M_{\theta z} = \frac{1-\nu}{2}D\left[\frac{1}{R}\left(\frac{\partial u_\theta}{\partial z} - 2\frac{\partial^2 u_r}{\partial \theta \partial z}\right)\right] \tag{A.106}$$

in which

$$D = \frac{Eh^3}{12(1-\nu^2)} \tag{A.107}$$

Equations (A.104) to (A.106) are now used to find expressions for Q_{zr} and $Q_{\theta r}$ by substitution into equations (A.94) and (A.95).

$$\begin{aligned} Q_{zr} &= \frac{\partial}{\partial z}\left(D\left[-\frac{\partial^2 u_r}{\partial z^2}+\frac{\nu}{R^2}\left(\frac{\partial u_\theta}{\partial \theta}-\frac{\partial^2 u_r}{\partial \theta^2}\right)\right]\right)+\frac{1}{R}\frac{\partial}{\partial \theta}\left(\frac{1-\nu}{2}D\left[\frac{1}{R}\left(\frac{\partial u_\theta}{\partial z}-2\frac{\partial^2 u_r}{\partial \theta \partial z}\right)\right]\right) \\ &= D\left[-\frac{\partial^3 u_r}{\partial z^3}+\frac{\nu}{R^2}\left(\frac{\partial^2 u_\theta}{\partial z \partial \theta}-\frac{\partial^3 u_r}{\partial z \partial \theta^2}\right)\right]+\frac{1-\nu}{2}D\left[\frac{1}{R^2}\left(\frac{\partial^2 u_\theta}{\partial \theta \partial z}-2\frac{\partial^3 u_r}{\partial \theta^2 \partial z}\right)\right] \end{aligned} \tag{A.108}$$

$$\begin{aligned} Q_{\theta r} &= \frac{\partial}{\partial z}\left(\frac{1-\nu}{2}D\left[\frac{1}{R}\left(\frac{\partial u_\theta}{\partial z}-2\frac{\partial^2 u_r}{\partial \theta \partial z}\right)\right]\right)+\frac{1}{R}\frac{\partial}{\partial \theta}\left(D\left[-\nu\frac{\partial^2 u_r}{\partial z^2}+\frac{1}{R^2}\left(\frac{\partial u_\theta}{\partial \theta}-\frac{\partial^2 u_r}{\partial \theta^2}\right)\right]\right) \\ &= \frac{1-\nu}{2}\frac{D}{R}\left(\frac{\partial^2 u_\theta}{\partial z^2}-2\frac{\partial^3 u_r}{\partial \theta \partial z^2}\right)+\frac{D}{R}\left[-\nu\frac{\partial^3 u_r}{\partial \theta \partial z^2}+\frac{1}{R^2}\left(\frac{\partial^2 u_\theta}{\partial \theta^2}-\frac{\partial^3 u_r}{\partial \theta^3}\right)\right] \end{aligned} \tag{A.109}$$

Substitution of equations (A.96) to (A.98), (A.108) and (A.109) into equations (A.91) to (A.93) gives the equations of motion for each considered degree of freedom in terms of just material and geometrical properties:

$$\frac{\partial}{\partial z}\left(\frac{Eh}{1-\nu^2}\left[\frac{\partial u_z}{\partial z}+\frac{\nu}{R}\left(\frac{\partial u_\theta}{\partial \theta}+u_r\right)\right]\right)+\frac{1}{R}\frac{\partial}{\partial \theta}\left(\frac{Eh}{2(1+\nu)}\left[\frac{\partial u_\theta}{\partial z}+\frac{1}{R}\frac{\partial u_z}{\partial \theta}\right]\right)+q_z=\rho h\ddot{u}_z \tag{A.110}$$

$$\begin{aligned} &\frac{\partial}{\partial z}\left(\frac{Eh}{2(1+\nu)}\left[\frac{\partial u_\theta}{\partial z}+\frac{1}{R}\frac{\partial u_z}{\partial \theta}\right]\right)+\frac{1}{R}\frac{\partial}{\partial \theta}\left(\frac{Eh}{1-\nu^2}\left[\nu\frac{\partial u_z}{\partial z}+\frac{1}{R}\left(\frac{\partial u_\theta}{\partial \theta}+u_r\right)\right]\right) \\ &+\frac{1}{R}\left(\frac{1-\nu}{2}\frac{D}{R}\left(\frac{\partial^2 u_\theta}{\partial z^2}-2\frac{\partial^3 u_r}{\partial \theta \partial z^2}\right)+\frac{D}{R}\left[-\nu\frac{\partial^3 u_r}{\partial \theta \partial z^2}+\frac{1}{R^2}\left(\frac{\partial^2 u_\theta}{\partial \theta^2}-\frac{\partial^3 u_r}{\partial \theta^3}\right)\right]\right) \\ &+q_\theta=\rho h\ddot{u}_\theta \end{aligned} \tag{A.111}$$

$$\begin{aligned} &\frac{\partial}{\partial z}\left(D\left[-\frac{\partial^3 u_r}{\partial z^3}+\frac{\nu}{R^2}\left(\frac{\partial^2 u_\theta}{\partial z \partial \theta}-\frac{\partial^3 u_r}{\partial z \partial \theta^2}\right)\right]+\frac{1-\nu}{2}D\left[\frac{1}{R^2}\left(\frac{\partial^2 u_\theta}{\partial \theta \partial z}-2\frac{\partial^3 u_r}{\partial \theta^2 \partial z}\right)\right]\right) \\ &+\frac{1}{R}\frac{\partial}{\partial \theta}\left(\frac{1-\nu}{2}\frac{D}{R}\left(\frac{\partial^2 u_\theta}{\partial z^2}-2\frac{\partial^3 u_r}{\partial \theta \partial z^2}\right)+\frac{D}{R}\left[-\nu\frac{\partial^3 u_r}{\partial \theta \partial z^2}+\frac{1}{R^2}\left(\frac{\partial^2 u_\theta}{\partial \theta^2}-\frac{\partial^3 u_r}{\partial \theta^3}\right)\right]\right) \\ &-\frac{1}{R}\left(\frac{Eh}{1-\nu^2}\left[\nu\frac{\partial u_z}{\partial z}+\frac{1}{R}\left(\frac{\partial u_\theta}{\partial \theta}+u_r\right)\right]\right)+q_r=\rho h\ddot{u}_r \end{aligned} \tag{A.112}$$

Through simplification and collection of terms related to the displacement and acceleration in each degree of freedom, equations (A.110) to (A.112) can be rewritten to the matrix equation

$$\mathbf{L}\mathbf{u}_w + \mathbf{I}\ddot{\mathbf{u}}_w = \mathbf{q}_w \tag{A.113}$$

in which $\mathbf{L}$ is the 3×3 stiffness matrix, $\mathbf{I}$ is the 3×3 inertia matrix, $\mathbf{u}_w = [u_z\ u_\theta\ u_r]^T$, $\ddot{\mathbf{u}}_w = [\ddot{u}_z\ \ddot{u}_\theta\ \ddot{u}_r]^T$ and $\mathbf{q}_w = [q_z\ q_\theta\ q_r]^T$. Please note that for the components of $\mathbf{L}$ below, equation (A.110) is multiplied by -1. The components of $\mathbf{L}$ are then

$$\begin{aligned}
L_{11} &= -\frac{Eh}{1-\nu^2}\frac{\partial^2}{\partial z^2} - \frac{1}{R^2}\frac{Eh}{2(1+\nu)}\frac{\partial^2}{\partial\theta^2} \\
L_{12} = L_{21} &= -\frac{Eh}{2R(1-\nu)}\frac{\partial^2}{\partial z\partial\theta} \\
L_{13} = L_{31} &= \frac{Eh}{1-\nu^2}\frac{\nu}{R}\frac{\partial}{\partial z} \\
L_{22} &= -\left(\frac{Eh}{2(1+\nu)} + \frac{D}{R^2}\frac{1-\nu}{2}\right)\frac{\partial^2}{\partial z^2} - \frac{1}{R^2}\left(\frac{Eh}{1-\nu^2} + \frac{D}{R^2}\right)\frac{\partial^2}{\partial\theta^2} \\
L_{23} = L_{32} &= \frac{1}{R^2}\frac{Eh}{1-\nu^2}\frac{\partial}{\partial\theta} - \frac{D}{R^2}\frac{\partial^3}{\partial\theta\partial z^2} - \frac{D}{R^4}\frac{\partial^3}{\partial\theta^3} \\
L_{33} &= D\frac{\partial^4}{\partial z^4} + 2\frac{D}{R^2}\frac{\partial^4}{\partial\theta^2\partial z^2} + \frac{D}{R^4}\frac{\partial^4}{\partial\theta^4} + \frac{1}{R^2}\frac{Eh}{1-\nu^2}
\end{aligned} \tag{A.114}$$

The matrix $\mathbf{I}$ is a diagonal matrix with entries $I_{ii} = \rho h$.
Since the mode-matching technique makes use of the modal expressions for each degree of freedom, the eigenfrequencies and eigenwavenumbers of the tank are sought. In order to find the eigenfrequencies and eigenwavenumbers of the cylindrical shell, the method of separation of variables is applied. For the circumferential mode shapes, a periodic function is assumed, so that continuity of the tank wall is ensured. The cosine and sine functions for this degree of freedom are based on Soedel (2005) and Tsouvalas (2006). For the vertical direction a mode shape is assumed as an exponential function. Through time, the tank is assumed to vibrate harmonically, so that the final applied solutions are

$$\begin{aligned}
u_z(z,\theta,t) &= \sum_{m=0}^{\infty}\sum_{l=1}^{8}\tilde{U}_z \exp(\lambda z)\cos(m\theta)\exp(\mathrm{i}\,\omega t) \\
u_\theta(z,\theta,t) &= \sum_{m=0}^{\infty}\sum_{l=1}^{8}\tilde{U}_\theta \exp(\lambda z)\sin(m\theta)\exp(\mathrm{i}\,\omega t) \\
u_r(z,\theta,t) &= \sum_{m=0}^{\infty}\sum_{l=1}^{8}\tilde{U}_r \exp(\lambda z)\cos(m\theta)\exp(\mathrm{i}\,\omega t)
\end{aligned} \tag{A.115}$$

Substitution of equation (A.115) into equation (A.113), division by $\exp(\mathrm{i}\,\omega t)$, division by $\exp(\lambda z)$, division by $\cos(m\theta)$ of the equations of motion for degrees of freedom z and r and division by $\sin(m\theta)$ and multiplication with -1 of the equation of motion for degree of

freedom θ changes the elements of matrix $\mathbf{L}$ to

$$\begin{aligned}
L_{11} &= -\frac{\lambda^2 Eh}{1-\nu^2} + \frac{m^2}{R^2}\frac{Eh}{2(1+\nu)} \\
L_{12} = L_{21} &= -\frac{m\lambda Eh}{2R(1-\nu)} \\
L_{13} = L_{31} &= \frac{\lambda Eh}{1-\nu^2}\frac{\nu}{R} \\
L_{22} &= \lambda^2\left(\frac{Eh}{2(1+\nu)} - \frac{D}{R^2}\frac{1-\nu}{2}\right) + \frac{m^2}{R^2}\left(\frac{Eh}{1-\nu^2} + \frac{D}{R^2}\right) \\
L_{23} = L_{32} &= -\frac{m}{R^2}\frac{Eh}{1-\nu^2} + \frac{m\lambda^2 D}{R^2} - \frac{m^3 D}{R^4} \\
L_{33} &= \lambda^4 D - 2\frac{m^2\lambda^2 D}{R^2} + \frac{m^4 D}{R^4} + \frac{1}{R^2}\frac{Eh}{1-\nu^2}
\end{aligned} \tag{A.116}$$

and the elements of matrix $\mathbf{I}$ to $[-\omega^2\rho h \quad \omega^2\rho h \quad \omega^2\rho h]^T$ Since both matrices are now multiplied with vector $\tilde{\mathbf{u}}_w = [\tilde{U}_z\, \tilde{U}_\theta\, \tilde{U}_r]^T$, which contains the complex amplitudes of the assumed mode shapes, equation (A.113) can be written as

$$(\mathbf{L} + \mathbf{I})\tilde{\mathbf{u}}_w = \mathbf{q}_w \tag{A.117}$$

For the circumferential modes, the wavenumbers can be seen to be $m = 0, 1, 2, ..., \infty$ to ensure continuity of the tank wall in the circumferential direction. To find the eigenwavenumbers in vertical direction, the eigenvalue problem needs to be solved, so in equation (A.117) $\mathbf{q} = \mathbf{0}$. The non-trivial solution is found by setting $\det(\mathbf{L} + \mathbf{I}) = 0$, resulting in an 8^{th} degree polynomial with respect to λ. For sake of brevity, this is not written out, but it can be seen from equation (A.116) that the highest power of λ after multiplying three elements of $(\mathbf{L} + \mathbf{I})$ is 8.
This equation needs to be solved numerically, as polynomials of degree 5 or higher have no analytical solution, according to the Abel-Ruffini theorem. Note that, as $\det(\mathbf{L} + \mathbf{I})$ is a function of wavenumbers λ and m, and frequency ω, the wavenumbers λ are a function of m and ω.
In order to obtain the eigenfrequencies and eigenwavenumbers of the tank, the expressions found for the wall's degrees of freedom must be substituted both in the interface conditions that link segments of wall and the wall to the bottom and roof of the tank, and in the boundary conditions. Solving the resulting eigenvalue problem will yield the eigenfrequencies and eigenwavenumbers of the tank, as well as the ratios of the modal amplitudes, so the mode shapes. The only remaining unkowns are then the values of the modal amplitudes, which can be solved by substitution of the modal expressions in the equations of motion, including external forcing.

A.2 Shell stresses

The general expression for the stresses in the shell elements are (Soedel (2005))

$$\begin{aligned}\sigma_{11} &= \frac{E}{1-\nu^2}\left[\varepsilon_{11}^0 + \nu\varepsilon_{22}^0 + \alpha_3(k_{11}+\nu k_{22})\right]\\ \sigma_{22} &= \frac{E}{1-\nu^2}\left[\varepsilon_{22}^0 + \nu\varepsilon_{11}^0 + \alpha_3(k_{22}+\nu k_{11})\right]\\ \sigma_{12} &= G\left(\varepsilon_{12}^0 + \alpha_3 k_{12}\right)\end{aligned} \tag{A.118}$$

with

$$\varepsilon_{11}^0 = \frac{1}{A_1}\frac{\partial u_1}{\partial \alpha_1} + \frac{u_2}{A_1A_2}\frac{\partial A_1}{\partial \alpha_2} \tag{A.119}$$

$$\varepsilon_{22}^0 = \frac{1}{A_2}\frac{\partial u_2}{\partial \alpha_2} + \frac{u_1}{A_1A_2}\frac{\partial A_2}{\partial \alpha_1} \tag{A.120}$$

$$\varepsilon_{12}^0 = \frac{A_2}{A_1}\frac{\partial}{\partial \alpha_1}\left(\frac{u_2}{A_2}\right) + \frac{A_1}{A_2}\frac{\partial}{\partial \alpha_2}\left(\frac{u_1}{A_1}\right) \tag{A.121}$$

$$k_{11} = -\frac{1}{A_1}\frac{\partial}{\partial \alpha_1}\left(\frac{1}{A_1}\frac{\partial u_3}{\partial \alpha_1}\right) - \frac{1}{A_1A_2^2}\frac{\partial u_3}{\partial \alpha_2}\frac{\partial A_1}{\partial \alpha_2} \tag{A.122}$$

$$k_{22} = -\frac{1}{A_2}\frac{\partial}{\partial \alpha_2}\left(\frac{1}{A_2}\frac{\partial u_3}{\partial \alpha_2}\right) - \frac{1}{A_2A_1^2}\frac{\partial u_3}{\partial \alpha_1}\frac{\partial A_2}{\partial \alpha_1} \tag{A.123}$$

$$k_{12} = -\frac{A_2}{A_1}\frac{\partial}{\partial \alpha_1}\left(\frac{1}{A_2^2}\frac{\partial u_3}{\partial \alpha_2}\right) - \frac{A_1}{A_2}\frac{\partial}{\partial \alpha_2}\left(\frac{1}{A_1^2}\frac{\partial u_3}{\partial \alpha_1}\right) \tag{A.124}$$

By substituting the coordinates and fundamental form parameters of the plate from equations (A.19) and (A.21) into these equations, the stresses in the wall can be calculated as

$$\begin{aligned}\sigma_{zz} &= \frac{E_w h_w}{1-\nu_w^2}\left(\frac{\partial u_z}{\partial z} + \frac{\nu_w}{R}\frac{\partial u_\theta}{\partial \theta} + \frac{\nu u_r}{R} \pm \frac{h_w}{2}\left(-\frac{\partial^2 u_r}{\partial z^2} + \frac{\nu_w}{R^2}\left[\frac{\partial u_\theta}{\partial \theta} - \frac{\partial^2 u_r}{\partial \theta^2}\right]\right)\right)\\ \sigma_{\theta\theta} &= \frac{E_w h_w}{1-\nu_w^2}\left(\nu_w\frac{\partial u_z}{\partial z} + \frac{1}{R}\frac{\partial u_\theta}{\partial \theta} + \frac{u_r}{R} \pm \frac{h_w}{2}\left(-\nu_w\frac{\partial^2 u_r}{\partial z^2} + \frac{1}{R^2}\left[\frac{\partial u_\theta}{\partial \theta} - \frac{\partial^2 u_r}{\partial \theta^2}\right]\right)\right)\\ \sigma_{z\theta} &= \frac{E_w h_w}{2(1+\nu_w)}\left(\frac{\partial u_\theta}{\partial z} + \frac{1}{R}\frac{\partial u_z}{\partial \theta} + \frac{h_w}{2R}\left[\frac{\partial u_\theta}{\partial z} - 2\frac{\partial^2 u_r}{\partial z \partial \theta}\right]\right)\end{aligned} \tag{A.125}$$

Similarly, substitution of equations (A.87) and (A.90) leads to expressions of the stresses in the plate as

$$\begin{aligned}
\sigma_{rr} &= \frac{E_p h_p}{1-\nu_p^2}\left(\frac{\partial u_r}{\partial r} + \nu_p\left(\frac{1}{r}\frac{\partial u_\theta}{\partial \theta} + \frac{u_r}{r}\right) \pm \frac{h_p}{2}\left[-\frac{\partial^2 u_z}{\partial r^2} + \nu_p\left(-\frac{1}{r^2}\frac{\partial^2 u_z}{\partial \theta^2} - \frac{1}{r}\frac{\partial u_z}{\partial r}\right)\right]\right) \\
\sigma_{\theta\theta} &= \frac{E_p h_p}{1-\nu_p^2}\left(\nu_p\frac{\partial u_r}{\partial r} + \frac{1}{r}\frac{\partial u_\theta}{\partial \theta} + \frac{u_r}{r} \pm \frac{h_p}{2}\left[-\nu_p\frac{\partial^2 u_z}{\partial r^2} - \frac{1}{r^2}\frac{\partial^2 u_z}{\partial \theta^2} - \frac{1}{r}\frac{\partial u_z}{\partial r}\right]\right) \\
\sigma_{r\theta} &= \frac{E_p h_p}{2(1+\nu_p)}\left(-\frac{1}{r}u_\theta + \frac{\partial u_\theta}{\partial r} + \frac{1}{r}\frac{\partial u_r}{\partial \theta} + \frac{h_p}{2}\left[\frac{2}{r^2}\frac{\partial u_z}{\partial \theta} - \frac{2}{r}\frac{\partial^2 u_z}{\partial r \partial \theta}\right]\right)
\end{aligned} \tag{A.126}$$

Appendix B Equations of motion

In this section, an alternative approach is shown to find the equations of motion of the tank's bottom plate including both dynamic and kinematic soil-structure interaction.
First, the expected wavefields are described, after which the equations of motion of the soil layer are formulated and the eigenfunctions are found. Next, boundary and interface conditions are formulated that relate the motions of the soil to the motions of the supported structure, in this case assumed to be a plate. Substitution of the found solutions into these conditions can yield expressions for the scattered and radiated wave fields, and the motions of the plate.

B.1 Scatter

Scattering and refraction of waves occur when a wave propagating through a medium reaches another medium with different elastodynamic properties. As de Hoop (2009) describes it, the second medium, or the scatterer, occupies a domain D_s that is surrounded by the domain of the first medium D. In the case of the liquid storage tank, a soil layer is considered that is unbounded in horizontal direction and lays on top of immovable bedrock. The soil column below the tank is here defined as the scatterer occupying domain D_s, while the soil surrounding it lies within D. In the examined case, the change in elastodynamic properties is caused by the presence of the tank. Its presence imposes restrictions on the displacements of the soil through stresses that are absent in the free field situation.
In linear theory, the total wave field is the superposition of an incident wave field and a scattered wave field (de Hoop (2008)). Although all waves are considered steady-state waves in both domains, the incident wave is regarded as the cause of the disturbance at the interface of the domains, and the scattered and refracted waves the consequence. As a result, the scattered and refracted wave must travel away from the interface (Achenbach (2003)).
The refracted wave in this case is again reflected at the center of D_s and subsequently refracted and reflected at the interface between D and D_s, a process that will continue indefinitely. Since only the combination of all wave fields in D_s is of interest, a distinction between all reflected and refracted wave fields is not necessary. It will be shown that these waves all have the same shape, so that their combined action in the steady state can be captured through the final factor with which the shape is amplified. In other words, these waves will be standing waves.
It is important to note that the total wave field is not just a superposition of the incident and the scattered wave fields. The waves that are refracted at the interface will set the tank in motion that in its turn will set the soil in motion through radiated waves. The total wave field in the embedding domain D will thus be the superposition of the incident, the scattered and the radiated wave field.

The scattering of the incident wave is caused by the stresses exerted by the tank on soil domain D_s. It is assumed, that if the tank bottom remains perfectly still, no energy from the incident wave is passed on to the tank and all of the energy is scattered away.
A radiated wave caused by the inertia of the tank is also generated through stresses on the interface between tank plate and D_s. It is speculated that different stress levels at the soil-structure interface (for example caused by the displacements of the structure) lead to different ratios of energy scattered away to energy in the incident wave field. Therefore, the

'level' of scattering is time or frequency dependent, as is the radiated wave field.

B.2 Derivation soil equation of motion

The equations governing the motion of the soil are derived, following Achenbach (2003), from the principle of balance of linear momentum, a kinematic condition, relating displacements to strains, and Hooke's law, relating strains to stresses.
Considering in a continuum, a body with volume V on which body forces $f_i(x_i, t)$ act and surface S on which surface tractions $t_i(x_i, t)$ act, and following the principle of balance of translational momentum, in linear theory the instantaneous rate of change of linear momentum of the body is equal to the external forces acting on it at an instance in time. In mathematical terms this is represented as

$$\int_V f_i(x_i, t) + \int_S t_i(x_i, t)\mathrm{d}S = \int_V \rho\ddot{u}_i(x_i, t)\mathrm{d}V \tag{B.1}$$

It can be shown (often for the case of a tetrahedron) that the evaluation of the volume integrals can be written as the evaluation of the surface integral (a factor multiplied by ΔS) multiplied with a factor representing the third dimension (i.e. h). Dividing all terms resulting from the evaluation of equation (B.1) by ΔS and taking the limit of h approaching 0, results in the Cauchy stress formula:

$$t_i = \tau_{ji} n_j \tag{B.2}$$

in which the component τ_{ji} gives the traction in direction x_i on a surface with the normal in direction x_j. Substitution of equation (B.2) into equation (B.1) and application of Gauss's theorem (equation (B.3))

$$\int_S \mathbf{f} \cdot \mathbf{n}\mathrm{d}S = \int_V \nabla \cdot \mathbf{f}\mathrm{d}V \tag{B.3}$$

results in

$$\int_V f_i(x_i, t) + \tau_{ji,j}(x_i, t) - \rho\ddot{u}_i(x_i, t)\mathrm{d}V = 0 \tag{B.4}$$

in which $\tau_{ji,j}$ is the divergence of τ_{ji}. Since equation (B.4) must hold piecewise,

$$f_i(x_i, t) + \tau_{ij,j}(x_i, t) - \rho\ddot{u}_i(x_i, t) = 0 \tag{B.5}$$

also holds, which is known as Cauchy's first law of momentum. Note that $\tau_{ji} = \tau_{ij}$, which can be shown from the balance of rotational momentum.
The kinematic condition that relates displacements to strains can in linear theory be represented by the tensor ε, defined as

$$\varepsilon_{ij} = \frac{1}{2}(u_{i,j} + u_{j,i}) \tag{B.6}$$

The constitutive relations that relate stresses to strains are given by Hooke's law, that is defined as

$$\tau_{ij} = C_{ijkl}\varepsilon_{kl} \tag{B.7}$$

For an elastic, isotropic material, the tensor C_{ijkl} can be expressed as

$$C_{ijkl} = \lambda\delta_{ij}\delta_{kl} + \mu(\delta_{ik}\delta_{jl} + \delta_{il}\delta_{jk}) \tag{B.8}$$

Substitution of equation (B.8) into equation (B.7) results in

$$\tau_{ij} = \lambda\delta_{ij}\varepsilon_{kk} + 2\mu\varepsilon_{ij} \tag{B.9}$$

To arrive at the differential equation governing the soil's displacements, equations (B.6) and (B.9) are substituted into equation (B.5) so that

$$\mu u_{i,jj} + (\lambda+\mu)u_{j,ji} + f_i = \rho\ddot{u}_i \tag{B.10}$$

or in vector notation:

$$\mu\nabla^2\mathbf{u} + (\lambda+\mu)\nabla\nabla\cdot\mathbf{u} + \mathbf{f} = \rho\ddot{\mathbf{u}} \tag{B.11}$$

For finding solutions to the equation of motion, it is beneficial to express the displacement vector in terms of displacement potentials. Aki and Richards (2009) show that writing the displacement vector in potentials as

$$\mathbf{u} = \nabla\phi + \nabla\times\nabla\times\boldsymbol{\psi} + \nabla\times\boldsymbol{\chi} \tag{B.12}$$

with $\boldsymbol{\psi} = [0,0,\psi]^T$ and $\boldsymbol{\chi} = [0,0,\chi]^T$, and substituting it in equation (B.11) effectively allows the equation of motion to be written as 3 uncoupled equations of motion. Each describes the motion of an unknown potential function, ϕ, ψ and χ, related to, respectively, the pressure wave, the vertical shear wave and the horizontal shear wave. After expressing the body forces in similar form as

$$\mathbf{f} = \nabla\Phi + \nabla\times\nabla\times\boldsymbol{\Psi} + \nabla\times\boldsymbol{X} \tag{B.13}$$

with $\boldsymbol{\Psi} = [0,0,\Psi]^T$ and $\boldsymbol{X} = [0,0,X]^T$, and substituting equation (B.13) in the equation of motion, equation (B.11) can be rewritten to

$$\nabla\left((\lambda+2\mu)\nabla^2\phi + \Phi - \rho\ddot{\phi}\right) + \nabla\times\nabla\times\left(\mu\nabla^2\boldsymbol{\psi} + \boldsymbol{\Psi} - \rho\ddot{\boldsymbol{\psi}}\right) + \nabla\times\left(\mu\nabla^2\boldsymbol{\chi} + \boldsymbol{X} - \rho\ddot{\boldsymbol{\chi}}\right) = 0 \tag{B.14}$$

which is satisfied if

$$\begin{aligned}(\lambda+2\mu)\nabla^2\phi + \Phi - \rho\ddot{\phi} &= 0\\ \mu\nabla^2\psi + \Psi - \rho\ddot{\psi} &= 0\\ \mu\nabla^2\chi + X - \rho\ddot{\chi} &= 0\end{aligned} \tag{B.15}$$

The relation

$$\nabla^2[0,0,f]^T = \nabla^2 f \tag{B.16}$$

is used to reduce the original unknown vector functions in equation (B.14) to the shown unknown scalar functions in equation (B.15).

B.2.1 Problem statement

The potentials in equation (B.15) describe the total displacement field (through equation (B.12)) of a considered domain. For domain D, denoted by superscript (I) the total wave field is considered as the superposition of an incident, a scattered and a radiated wave field, so that

$$\begin{aligned}\phi_{\text{tot}}^{(I)} &= \phi_i + \phi_s + \phi_r\\ \psi_{\text{tot}}^{(I)} &= \psi_i + \psi_s + \psi_r\\ \chi_{\text{tot}}^{(I)} &= \chi_i + \chi_s + \chi_r\end{aligned} \tag{B.17}$$

For domain D_s, denoted by superscript (II), the total wave field is considered as the superposition of a refracted and a radiated wave field, so that

$$\begin{aligned} \phi_{\text{tot}}^{(II)} &= \phi_{rad} + \phi_{ref} \\ \psi_{\text{tot}}^{(II)} &= \psi_{rad} + \psi_{ref} \\ \chi_{\text{tot}}^{(II)} &= \chi_{rad} + \chi_{ref} \end{aligned} \tag{B.18}$$

In equation (B.15), the force terms Φ, Ψ and X are disregarded. Energy is introduced into the system through a known incident wave field. No additional forcing is considered.
Applying the Fourier transform, equation (B.15) is transformed to the form of a Helmholtz equation as

$$\begin{aligned} \nabla^2\tilde{\phi} + k_p^2\tilde{\phi} &= 0 \\ \nabla^2\tilde{\psi} + k_s^2\tilde{\psi} &= 0 \\ \nabla^2\tilde{\chi} + k_s^2\tilde{\chi} &= 0 \end{aligned} \tag{B.19}$$

in which the tilde shows that the potentials are expressed in the frequency domain and in which

$$\begin{aligned} k_p^2 &= \frac{\omega^2\rho}{\lambda + 2\mu} \\ k_s^2 &= \frac{\omega^2\rho}{\mu} \end{aligned} \tag{B.20}$$

For domain D, it is assumed that the incident wave field is known. The scattered and radiated wave fields need to be solved, as well as the refracted and radiated wave fields in domain D_s.

B.2.2 Solution - separation of variables

Since the differential equations are all of the same form, the solution method (separation of variables) is shown once for a function $F(r, \theta, z)$, which is expressed as a multiplication of functions that are all dependent on just one of the coordinates r, θ and z:

$$F(r, \theta, z) = R(r)\Theta(\theta)Z(z) \tag{B.21}$$

Substitution into

$$\nabla^2 F + k^2 F = 0 \tag{B.22}$$

yields

$$\Theta Z \frac{\mathrm{d}^2 R}{\mathrm{d}r^2} + \Theta Z \frac{1}{r}\frac{\mathrm{d}R}{\mathrm{d}r} + ZR\frac{1}{r^2}\frac{\mathrm{d}^2\Theta}{\mathrm{d}\theta^2} + R\Theta\frac{\mathrm{d}^2 Z}{\mathrm{d}z^2} + k^2 R\Theta Z = 0 \tag{B.23}$$

Division by $R\Theta Z$, multiplication by r^2 and rearranging gives

$$\frac{1}{R}r^2\frac{\mathrm{d}^2 R}{\mathrm{d}r^2} + \frac{1}{R}r\frac{\mathrm{d}R}{\mathrm{d}r} + r^2\frac{1}{Z}\frac{\mathrm{d}^2 Z}{\mathrm{d}z^2} + k^2 r^2 = -\frac{1}{\Theta}\frac{\mathrm{d}^2\Theta}{\mathrm{d}\theta^2} \tag{B.24}$$

which can only hold if both sides are equal to a constant, chosen here as n^2. The right hand side can be rearranged as in equation (A.58), so that the solution can again be given as

$$\Theta(\theta) = A\cos(n(\theta + \phi_c)) \tag{B.25}$$

with a phase angle ϕ_c that can arbitrarily be chosen, due to the axisymmetry of the system at hand. It turns out that the values of $\phi_c = 0$ are convenient for the potentials ϕ and ψ, while a value of $\phi_c = \pi/2$ is convenient for χ, effectively making $\Theta(\theta)$ a sine function. The value n is an integer, due to the continuity of the displacement fields in circumferential direction.
The left hand side of equation (B.24) is then also equal to the same constant:

$$\frac{1}{R} r^2 \frac{\mathrm{d}^2 R}{\mathrm{d}r^2} + \frac{1}{R} r \frac{\mathrm{d}R}{\mathrm{d}r} + r^2 \frac{1}{Z} \frac{\mathrm{d}^2 Z}{\mathrm{d}z^2} + k^2 r^2 = n^2 \tag{B.26}$$

Division by r^2 and rearrangement gives

$$\frac{1}{R} \frac{\mathrm{d}^2 R}{\mathrm{d}r^2} + \frac{1}{R} \frac{1}{r} \frac{\mathrm{d}R}{\mathrm{d}r} + k^2 - \frac{n^2}{r^2} = -\frac{1}{Z} \frac{\mathrm{d}^2 Z}{\mathrm{d}z^2} \tag{B.27}$$

Again, this can only hold if both sides equal a constant, which is named k_z^2 here. Evaluating the right hand side of equation (B.27) gives

$$Z k_z^2 + \frac{\mathrm{d}^2 Z}{\mathrm{d}z^2} = 0 \tag{B.28}$$

The general solution to this ordinary differential equation is

$$B \exp(i k_z z) + C \exp(-i k_z z) \tag{B.29}$$

The left hand side of equation (B.27) is also equal to the constant k_z^2:

$$\frac{1}{R} \frac{\mathrm{d}^2 R}{\mathrm{d}r^2} + \frac{1}{R} \frac{1}{r} \frac{\mathrm{d}R}{\mathrm{d}r} + k^2 - \frac{n^2}{r^2} = k_z^2 \tag{B.30}$$

Multiplication with Rr^2 turns it into

$$r^2 \frac{\mathrm{d}^2 R}{\mathrm{d}r^2} + r \frac{1}{r} \frac{\mathrm{d}R}{\mathrm{d}r} + k_r^2 r^2 - n^2 = 0 \tag{B.31}$$

in which $k_r^2 = k^2 - k_z^2$. This is the same form as equation (A.60), and substituting

$$\xi = \sqrt{k_r^2 r^2} \tag{B.32}$$

leads to equation (A.62), to which the solution is then given as

$$R(k_r r) = D H_n^{(1)}(k_r r) + E H_n^{(2)}(k_r r) \tag{B.33}$$

The complete solution is thus given by

$$F(r, \theta, z) = \cos(n(\theta + \phi_c)) \left(B' \exp(i k_z z) + C' \exp(-i k_z z) \right) \left(D H_n^{(1)}(k_r r) + E H_n^{(2)}(k_r r) \right) \tag{B.34}$$

in which $B' = AB$ and $C' = AC$.

Domain D For the unknown wave fields in domain D, $\mathbf{u}_s^{(I)}$ and $\mathbf{u}_r^{(I)}$, use can be made of Sommerfeld's radiation condition

$$\begin{aligned}\lim_{r\to\infty} r\left(\frac{\partial \mathbf{u}_s^{(I)}}{\partial r} - ik\mathbf{u}_s^{(I)}\right) = 0\\ \lim_{r\to\infty} r\left(\frac{\partial \mathbf{u}_r^{(I)}}{\partial r} - ik\mathbf{u}_r^{(I)}\right) = 0\end{aligned} \tag{B.35}$$

to eliminate from equation (B.34) the term related to $H_n^{(1)}$. This term describes waves traveling towards $r = 0$, while the wave fields $\mathbf{u}_s^{(I)}$ and $\mathbf{u}_r^{(I)}$ describe waves traveling away from the tank.
The expressions of the unknown potential fields in domain D are thus

$$\begin{aligned}\phi_s &= \sum_{n=0}^{\infty}\left(A_{\phi_s}\exp(ik_{p;z}z) + B_{\phi_s}\exp(-ik_{p;z}z)\right)H_n^{(2)}(k_{p;r}r)\cos(n\theta)\\ \psi_s &= \sum_{n=0}^{\infty}\left(A_{\psi_s}\exp(ik_{s;z}z) + B_{\psi_s}\exp(-ik_{s;z}z)\right)H_n^{(2)}(k_{s;r}r)\cos(n\theta)\\ \chi_s &= \sum_{n=0}^{\infty}\left(A_{\chi_s}\exp(ik_{s;z}z) + B_{\chi_s}\exp(-ik_{s;z}z)\right)H_n^{(2)}(k_{s;r}r)\sin(n\theta)\\ \phi_r &= \sum_{n=0}^{\infty}\left(A_{\phi_r}\exp(ik_{p;z}z) + B_{\phi_r}\exp(-ik_{p;z}z)\right)H_n^{(2)}(k_{p;r}r)\cos(n\theta)\\ \psi_r &= \sum_{n=0}^{\infty}\left(A_{\psi_r}\exp(ik_{s;z}z) + B_{\psi_r}\exp(-ik_{s;z}z)\right)H_n^{(2)}(k_{s;r}r)\cos(n\theta)\\ \chi_r &= \sum_{n=0}^{\infty}\left(A_{\chi_r}\exp(ik_{s;z}z) + B_{\chi_r}\exp(-ik_{s;z}z)\right)H_n^{(2)}(k_{s;r}r)\sin(n\theta)\end{aligned} \tag{B.36}$$

Domain D_s For the unknown wave fields in domain D_s, $\mathbf{u}_{ref}^{(II)}$ and $\mathbf{u}_{rad}^{(II)}$, use is made of the condition of having finite displacements, so

$$\mathbf{u}_{tot}^{(II)}\Big|_{r=0} = \left(\mathbf{u}_{ref}^{(II)} + \mathbf{u}_{rad}^{(II)}\right)\Big|_{r=0} \neq \infty \tag{B.37}$$

The Hankel functions $H_n^{(1)}$ and $H_n^{(2)}$ are defined as

$$\begin{aligned}H_n^{(1)}(r) &= J_n(r) + \mathrm{i}Y_n(r)\\ H_n^{(2)}(r) &= J_n(r) - \mathrm{i}Y_n(r)\end{aligned} \tag{B.38}$$

The terms with $Y_n(r)$ are singular at $r = 0$, as are their derivatives that would be present in the final expressions of the displacements $\mathbf{u}_{tot}^{(II)}$. The expressions of the unknown potential

fields in domain D_s are thus

$$\begin{aligned}
\phi_{ref} &= \sum_{n=0}^{\infty} \left(A_{\phi_{ref}} \exp(ik_{p;z}z) + B_{\phi_{ref}} \exp(-ik_{p;z}z) \right) J_n(k_{p;r}r) \cos(n\theta) \\
\psi_{ref} &= \sum_{n=0}^{\infty} \left(A_{\psi_{ref}} \exp(ik_{s;z}z) + B_{\psi_{ref}} \exp(-ik_{s;z}z) \right) J_n(k_{s;r}r) \cos(n\theta) \\
\chi_{ref} &= \sum_{n=0}^{\infty} \left(A_{\chi_{ref}} \exp(ik_{s;z}z) + B_{\chi_{ref}} \exp(-ik_{s;z}z) \right) J_n(k_{s;r}r) \sin(n\theta) \\
\phi_{rad} &= \sum_{n=0}^{\infty} \left(A_{\phi_{rad}} \exp(ik_{p;z}z) + B_{\phi_{rad}} \exp(-ik_{p;z}z) \right) J_n(k_{p;r}r) \cos(n\theta) \\
\psi_{rad} &= \sum_{n=0}^{\infty} \left(A_{\psi_{rad}} \exp(ik_{s;z}z) + B_{\psi_{rad}} \exp(-ik_{s;z}z) \right) J_n(k_{s;r}r) \cos(n\theta) \\
\chi_{rad} &= \sum_{n=0}^{\infty} \left(A_{\chi_{rad}} \exp(ik_{s;z}z) + B_{\chi_{rad}} \exp(-ik_{s;z}z) \right) J_n(k_{s;r}r) \sin(n\theta)
\end{aligned} \tag{B.39}$$

The excitation term is the incident wave field, which can be written in a more convenient form for finding the final solution to the problem. It is assumed to consist of a plane wave traveling from $x = -\infty$ with wavenumber k. The vertical particle displacements caused by the incident wave are written as

$$\phi_i(r, \theta, z, \omega) = \Phi_i(z) \mathrm{e}^{\mathrm{i}kr\cos(\theta)} \tag{B.40}$$

or, using Euler's formula,

$$\phi_i(r, \theta, z, \omega) = \Phi_i(z) \left[\cos(kr\cos(\theta)) + \mathrm{i}\sin(kr\cos(\theta)) \right] \tag{B.41}$$

Substituting the following equations (9.1.44-45) from Abramowitz and Stegun (1972)

$$\begin{aligned}
\cos(kr\cos(\theta)) &= J_0(z) + 2\sum_{n=1}^{\infty} (-1)^n J_{2n}(kr) \cos(2n\theta) \\
\sin(kr\cos(\theta)) &= 2\sum_{n=0}^{\infty} (-1)^n J_{2n+1}(kr) \cos((2n+1)\theta)
\end{aligned} \tag{B.42}$$

results in

$$\begin{aligned}
\phi_i(r, \theta, z, \omega) = \Phi_i(z) \Bigg[& J_0(z) + 2\sum_{n=1}^{\infty} (-1)^n J_{2n}(kr) \cos(2n\theta) \\
& + 2\mathrm{i} \sum_{n=0}^{\infty} (-1)^n J_{2n+1}(kr) \cos((2n+1)\theta) \Bigg]
\end{aligned} \tag{B.43}$$

which can be rewritten in a more compact form as

$$\phi_i(r, \theta, z, \omega) = \Phi_i(z) \sum_{n=0}^{\infty} \mathrm{i}^n \epsilon_n J_n(kr) \cos(n\theta) \tag{B.44}$$

in which ϵ_n is Neumann's symbol, defined as

$$\epsilon_n = 2 - \delta_{n0} \tag{B.45}$$

The benefit of this notation is that the plane wave is now expressed in the harmonics in horizontal direction of the cylindrical coordinate system. Assuming the incident wave only displaces particles in vertical direction and the direction in which it travels, the same approach can be applied to the horizontal and vertical shear incident waves to give

$$\psi_i(r,\theta,z,\omega) = \Psi_i(z) \sum_{n=0}^{\infty} \mathrm{i}^n \epsilon_n J_n(kr)\cos(n\theta) \tag{B.46}$$

$$\chi_i(r,\theta,z,\omega) = X_i(z) \sum_{n=0}^{\infty} \mathrm{i}^n \epsilon_n J_n(kr)\cos(n\theta) \tag{B.47}$$

It is worth repeating that the material properties of domains D and D_s are the same, so that reflected and refracted waves at the interface do not change wavenumbers or frequencies. As such, the wavenumbers of the incident, the scattered and the refracted wave fields are the same, and the wavenumbers of both radiated wave fields will be the same.

B.2.3 Boundary and interface conditions

For domain D, the boundary conditions describe no displacements at the bottom of the layer, due to the presence of bedrock, as

$$\left(\mathbf{u}_i^{(I)} + \mathbf{u}_s^{(I)} + \mathbf{u}_r^{(I)}\right) \Big|_{z=h} = \mathbf{0} \tag{B.48}$$

and no stresses at the top of the layer, since the soil is free to displace, so that

$$\left(\boldsymbol{\sigma}_i^{(I)} + \boldsymbol{\sigma}_s^{(I)} + \boldsymbol{\sigma}_r^{(I)}\right) \Big|_{z=0} = \mathbf{0} \tag{B.49}$$

For all wave fields in domain D, the stress vector in equation (B.49) is defined as $\boldsymbol{\sigma} = [\sigma_{zr}, \sigma_{z\theta}, \sigma_{zz}]^T$.
For domain D_s, the boundary conditions describe no displacements at the bottom of the layer, due to the presence of bedrock, as

$$\left(\mathbf{u}_{ref}^{(II)} + \mathbf{u}_{rad}^{(II)}\right) \Big|_{z=h} = \mathbf{0} \tag{B.50}$$

For the plate, the boundary conditions describe no bending moments at the edge of the plate, as

$$\mathbf{f}_p \Big|_{r=R} = \mathbf{0} \tag{B.51}$$

in which the force vector is defined as $\mathbf{f}_p = [M_{rr}, V_r, N_{rr}, N_{r\theta}]^T$.

At the interfaces between domain D_s and the plate, displacement and stress continuity is assumed, so that

$$\mathbf{u}_{tot}^{(II)} \Big|_{z=0} = \left(\mathbf{u}_{ref}^{(II)} + \mathbf{u}_{rad}^{(II)}\right) \Big|_{z=0} = \mathbf{u}_p \tag{B.52}$$

in which all displacement vectors are defined as $\mathbf{u} = [u_r, u_\theta, u_z]^T$, and

$$\boldsymbol{\sigma}_{tot}^{(II)} \Big|_{z=0} = \left(\boldsymbol{\sigma}_{ref}^{(II)} + \boldsymbol{\sigma}_{rad}^{(II)}\right) \Big|_{z=0} = \boldsymbol{\sigma}_p \tag{B.53}$$

in which all stress vectors are defined as $\boldsymbol{\sigma} = [\sigma_{zr}, \sigma_{z\theta}, \sigma_{zz}]^T$.
At the interface between soil domains D and D_s, also displacement and stress continuities are assumed, so that

$$\left(\mathbf{u}_i^{(I)} + \mathbf{u}_s^{(I)} + \mathbf{u}_r^{(I)}\right) \Big|_{r=R} = \left(\mathbf{u}_{ref}^{(II)} + \mathbf{u}_{rad}^{(II)}\right) \Big|_{r=R} \tag{B.54}$$

and

$$\left(\boldsymbol{\sigma}_i^{(I)} + \boldsymbol{\sigma}_s^{(I)} + \boldsymbol{\sigma}_r^{(I)}\right) \Big|_{r=R} = \left(\boldsymbol{\sigma}_{ref}^{(II)} + \boldsymbol{\sigma}_{rad}^{(II)}\right) \Big|_{r=R} \tag{B.55}$$

Finally, the three rigid body motions of the plate are considered, which provide the final equations of the system. The rigid body rotation of the plate around the z-axis is taken into account as

$$\int_0^R \int_0^{2\pi} r^2 \sigma_{z\theta} \mathrm{d}\theta \mathrm{d}r = -\omega^2 \frac{u_{p;rb;\theta}(r,\theta,\omega)}{r} \int_0^R \int_0^{2\pi} \rho_p h_p r^3 \mathrm{d}\theta \mathrm{d}r \tag{B.56}$$

The horizontal rigid body translation of the plate is considered with

$$F_H = -\omega^2 \left(u_{p;rb;r}[\cos(\theta) + \sin(\theta)] + u_{p;rb;\theta}[\cos(\theta) - \sin(\theta)]\right) \int_0^R \int_0^{2\pi} \rho_p h_p r \mathrm{d}\theta \mathrm{d}r \tag{B.57}$$

with

$$\begin{aligned} F_H = F_x + F_y = &\int_0^R \int_0^{2\pi} \left(\cos(\theta)\sigma_{zr} - \sin(\theta)\sigma_{z\theta}\right) \mathrm{d}\theta \mathrm{d}r \\ &+ \int_0^R \int_0^{2\pi} \left(\sin(\theta)\sigma_{zr} + \cos(\theta)\sigma_{z\theta}\right) \mathrm{d}\theta \mathrm{d}r \end{aligned} \tag{B.58}$$

and the vertical rigid body motion with

$$\int_0^R \int_0^{2\pi} \sigma_{zz} r \mathrm{d}\theta \mathrm{d}r = -\omega^2 u_{p;z;rb} \int_0^R \int_0^{2\pi} \rho_p h_p r \mathrm{d}\theta \mathrm{d}r \tag{B.59}$$

The number of boundary and interface conditions now is 28, which is equal to the number of unknowns in the solutions to each displacement field.

Appendix C Dynamic and kinematic conditions

This appendix is concentrated on the detailed application of the orthogonality properties in the equations of motion of the tank and the interface conditions between the tank and the fluid.

C.1 Equations of motion - Plate

This section treats the evaluation of equation (2.87) expanded into three separate equations for each unknown degree of freedom.
The summation over wavenumber n is removed by making use of the orthogonality property of the trigonometric functions. For clarity regarding the matrix multiplication with $\mathbf{K}_s$, the equations are written out. Multiplying the equations related to $u_{p;z}$ and $u_{p;r}$ with $\cos(q\theta)$ and the equation related to $u_{p;\theta}$ with $\sin(q\theta)$ and integrating from 0 to 2π gives (adjust layout)

$$\int_{\theta=0}^{2\pi} \Bigg\{ \sum_{n=0}^{\infty}\sum_{m=0}^{\infty} (\omega_{nm}^2 - \omega^2)\rho_p h_p \tilde{X}_{nm}(\omega)\tilde{U}_{p;znm}(r)\cos(n\theta) + K_{zz}(\omega)\sum_{n=0}^{\infty}\sum_{m=0}^{\infty}\tilde{X}_{nm}(\omega)\tilde{U}_{p;znm}(r)\cos(n\theta)$$
$$+K_{z\theta}(\omega)\sum_{n=0}^{\infty}\sum_{m=0}^{\infty}\tilde{X}_{nm}(\omega)\tilde{U}_{p;\theta nm}(r)\sin(n\theta) + K_{zr}(\omega)\sum_{n=0}^{\infty}\sum_{m=0}^{\infty}\tilde{X}_{nm}(\omega)\tilde{U}_{p;rnm}(r)\cos(n\theta)\Bigg\}\cos(q\theta)\mathrm{d}\theta =$$
$$\int_{\theta=0}^{2\pi}\left\{K_{zz}(\omega)\tilde{u}_{i;z}(r,\theta,\omega) + K_{z\theta}(\omega)\tilde{u}_{i;\theta}(r,\theta,\omega) + K_{zr}(\omega)\tilde{u}_{i;r}(r,\theta,\omega)\right\}\cos(q\theta)\mathrm{d}\theta$$
$$-\int_{\theta=0}^{2\pi}\mathrm{i}\omega\rho_{fl}\sum_{n=0}^{\infty}\left\{\sum_{a=1}^{\infty}P_{na}(\omega)I_n\left(\frac{\pi(2a-1)r}{2H_l}\right) + \sum_{b=1}^{\infty}Q_{nb}(\omega)J_n(\varepsilon_{nb}r/R) + \sum_{c=1}^{\infty}S_{nc}(\omega)J_n(\varepsilon_{nc}r/R)\right\}\cos(n\theta)\cos(q\theta)\mathrm{d}\theta \tag{C.1}$$

$$\int_{\theta=0}^{2\pi} \Bigg\{ \sum_{n=0}^{\infty}\sum_{m=0}^{\infty} (\omega_{nm}^2 - \omega^2)\rho_p h_p \tilde{X}_{nm}(\omega)\tilde{U}_{p;\theta nm}(r)\sin(n\theta) + K_{\theta z}(\omega)\sum_{n=0}^{\infty}\sum_{m=0}^{\infty}\tilde{X}_{nm}(\omega)\tilde{U}_{p;znm}(r)\cos(n\theta)$$
$$+K_{\theta\theta}(\omega)\sum_{n=0}^{\infty}\sum_{m=0}^{\infty}\tilde{X}_{nm}(\omega)\tilde{U}_{p;\theta nm}(r)\sin(n\theta) + K_{\theta r}(\omega)\sum_{n=0}^{\infty}\sum_{m=0}^{\infty}\tilde{X}_{nm}(\omega)\tilde{U}_{p;rnm}(r)\cos(n\theta)\Bigg\}\sin(q\theta)\mathrm{d}\theta =$$
$$\int_{\theta=0}^{2\pi}\left\{K_{\theta z}(\omega)\tilde{u}_{i;z}(r,\theta,\omega) + K_{\theta\theta}(\omega)\tilde{u}_{i;\theta}(r,\theta,\omega) + K_{\theta r}(\omega)\tilde{u}_{i;r}(r,\theta,\omega)\right\}\sin(q\theta)\mathrm{d}\theta \tag{C.2}$$

$$\int_{\theta=0}^{2\pi} \Bigg\{ \sum_{n=0}^{\infty}\sum_{m=0}^{\infty} (\omega_{nm}^2 - \omega^2)\rho_p h_p \tilde{X}_{nm}(\omega)\tilde{U}_{p;rnm}(r)\cos(n\theta) + K_{rz}(\omega)\sum_{n=0}^{\infty}\sum_{m=0}^{\infty}\tilde{X}_{nm}(\omega)\tilde{U}_{p;znm}(r)\cos(n\theta)$$
$$+K_{r\theta}(\omega)\sum_{n=0}^{\infty}\sum_{m=0}^{\infty}\tilde{X}_{nm}(\omega)\tilde{U}_{p;\theta nm}(r)\sin(n\theta) + K_{rr}(\omega)\sum_{n=0}^{\infty}\sum_{m=0}^{\infty}\tilde{X}_{nm}(\omega)\tilde{U}_{p;rnm}(r)\cos(n\theta)\Bigg\}\cos(q\theta)\mathrm{d}\theta =$$
$$\int_{\theta=0}^{2\pi}\left\{K_{rz}(\omega)\tilde{u}_{i;z}(r,\theta,\omega) + K_{r\theta}(\omega)\tilde{u}_{i;\theta}(r,\theta,\omega) + K_{rr}(\omega)\tilde{u}_{i;r}(r,\theta,\omega)\right\}\cos(q\theta)\mathrm{d}\theta \tag{C.3}$$

Making use of the orthogonality of the trigonometric functions reduces equations (C.1) to (C.3) to

$$\sum_{m=0}^{\infty}(\omega_{nm}^2-\omega^2)\rho_p h_p \tilde{X}_{nm}\tilde{U}_{p;znm}(r)+\int_{\theta=0}^{2\pi}K_{zz}\mathrm{d}\theta\ \sum_{m=0}^{\infty}\tilde{X}_{nm}\tilde{U}_{p;znm}(r)+\int_{\theta=0}^{2\pi}K_{zr}\mathrm{d}\theta\ \sum_{m=0}^{\infty}\tilde{X}_{nm}\tilde{U}_{p;rnm}(r)=$$
$$\frac{1}{\pi(1+\delta_{n0})}\int_{\theta=0}^{2\pi}\left(K_{zz}\tilde{u}_{i;z}(r,\theta)+K_{z\theta}\tilde{u}_{i;\theta}(r,\theta)+K_{zr}\tilde{u}_{i;r}(r,\theta)\right)\cos(n\theta)\mathrm{d}\theta$$
$$-\mathrm{i}\omega\rho_{fl}\left\{\sum_{a=1}^{\infty}P_{na}I_n\left(\frac{\pi(2a-1)r}{2H_l}\right)+\sum_{b=1}^{\infty}Q_{nb}J_n(\varepsilon_{nb}r/R)+\sum_{c=1}^{\infty}S_{nc}J_n(\varepsilon_{nc}r/R)\right\} \tag{C.4}$$

$$\sum_{m=0}^{\infty}(\omega_{nm}^2-\omega^2)\rho_p h_p \tilde{X}_{nm}\tilde{U}_{p;\theta nm}(r)+\int_{\theta=0}^{2\pi}K_{\theta\theta}\mathrm{d}\theta\ \sum_{m=0}^{\infty}\tilde{X}_{nm}\tilde{U}_{p;\theta nm}(r)=$$
$$\frac{1}{\pi(1+\delta_{n0})}\int_{\theta=0}^{2\pi}\left(K_{\theta z}\tilde{u}_{i;z}(r,\theta)+K_{\theta\theta}\tilde{u}_{i;\theta}(r,\theta)+K_{\theta r}\tilde{u}_{i;r}(r,\theta)\right)\sin(n\theta)\mathrm{d}\theta \tag{C.5}$$

$$\sum_{m=0}^{\infty}(\omega_{nm}^2-\omega^2)\rho_p h_p \tilde{X}_{nm}\tilde{U}_{p;rnm}(r)+\int_{\theta=0}^{2\pi}K_{rz}\mathrm{d}\theta\ \sum_{m=0}^{\infty}\tilde{X}_{nm}\tilde{U}_{p;znm}(r)+\int_{\theta=0}^{2\pi}K_{rr}\mathrm{d}\theta\ \sum_{m=0}^{\infty}\tilde{X}_{nm}\tilde{U}_{p;rnm}(r)=$$
$$\frac{1}{\pi(1+\delta_{n0})}\int_{\theta=0}^{2\pi}\left(K_{rz}\tilde{u}_{i;z}(r,\theta)+K_{r\theta}\tilde{u}_{i;\theta}(r,\theta)+K_{rr}\tilde{u}_{i;r}(r,\theta)\right)\cos(n\theta)\mathrm{d}\theta \tag{C.6}$$

Note the division of the equations by $\pi(1+\delta_{n0})$ to account for the evaluation of the integration. Also note that taking entries K_{ij} out of the integrals over θ and evaluating their integration separately is only possible for certain discretizations.
In order to apply the orthogonality conditions of the entire tank and thereby reduce the number of equations to be solved, the plate's equations of motion for each degree of freedom are multiplied by their respective mode shape and integrated over the radius. The terms independent of the radius are taken out of the integral.

$$\sum_{m=0}^{\infty}(\omega_{nm}^2-\omega^2)\rho_p h_p \tilde{X}_{nm}\int_{r=0}^{R}\tilde{U}_{p;znm}(r)\tilde{U}_{p;znl}(r)\mathrm{d}r+\int_{r=0}^{R}\int_{\theta=0}^{2\pi}K_{zz}\mathrm{d}\theta\ \sum_{m=0}^{\infty}\tilde{X}_{nm}\tilde{U}_{p;znm}(r)\tilde{U}_{p;znl}(r)\mathrm{d}r$$
$$+\int_{r=0}^{R}\int_{\theta=0}^{2\pi}K_{zr}\mathrm{d}\theta\mathrm{d}r\ \sum_{m=0}^{\infty}\tilde{X}_{nm}\int_{r=0}^{R}\tilde{U}_{p;rnm}(r)\tilde{U}_{p;znl}(r)\mathrm{d}r$$
$$=\frac{1}{\pi(1+\delta_{n0})}\int_{r=0}^{R}\int_{\theta=0}^{2\pi}\left\{K_{zz}\tilde{u}_{i;z}(r,\theta)+K_{z\theta}\tilde{u}_{i;\theta}(r,\theta)+K_{zr}\tilde{u}_{i;r}(r,\theta)\right\}\cos(n\theta)\tilde{U}_{p;znl}(r)\mathrm{d}\theta\mathrm{d}r$$
$$-\mathrm{i}\omega\rho_{fl}\int_{r=0}^{R}\left\{\sum_{a=1}^{\infty}P_{na}I_n\left(\frac{\pi(2a-1)r}{2H_l}\right)+\sum_{b=1}^{\infty}Q_{nb}J_n(\varepsilon_{nb}r/R)+\sum_{c=1}^{\infty}S_{nc}J_n(\varepsilon_{nc}r/R)\right\}\tilde{U}_{p;znl}(r)\mathrm{d}r \tag{C.7}$$

$$\sum_{m=0}^{\infty}(\omega_{nm}^2-\omega^2)\rho_p h_p\tilde{X}_{nm}\int_{r=0}^{R}\tilde{U}_{p;\theta nm}(r)\tilde{U}_{p;\theta nl}(r)\mathrm{d}r+\int_{r=0}^{R}\int_{\theta=0}^{2\pi}K_{\theta\theta}\mathrm{d}\theta\ \sum_{m=0}^{\infty}\tilde{X}_{nm}\tilde{U}_{p;\theta nm}(r)\tilde{U}_{p;\theta nl}(r)\mathrm{d}r$$
$$=\frac{1}{\pi(1+\delta_{n0})}\int_{r=0}^{R}\int_{\theta=0}^{2\pi}\left\{K_{\theta z}\tilde{u}_{i;z}(r,\theta)+K_{\theta\theta}\tilde{u}_{i;\theta}(r,\theta)+K_{\theta r}\tilde{u}_{i;r}(r,\theta)\right\}\sin(n\theta)\tilde{U}_{p;\theta nl}(r)\mathrm{d}\theta\mathrm{d}r \tag{C.8}$$

$$\sum_{m=0}^{\infty}(\omega_{nm}^2-\omega^2)\rho_p h_p\tilde{X}_{nm}\int_{r=0}^{R}\tilde{U}_{p;rnm}(r)\tilde{U}_{p;rnl}(r)\mathrm{d}r+\int_{r=0}^{R}\int_{\theta=0}^{2\pi}K_{rz}\mathrm{d}\theta\ \sum_{m=0}^{\infty}\tilde{X}_{nm}\tilde{U}_{p;znm}(r)\tilde{U}_{p;rnl}(r)\mathrm{d}r$$
$$+\int_{r=0}^{R}\int_{\theta=0}^{2\pi}K_{rr}\mathrm{d}\theta\mathrm{d}r\ \sum_{m=0}^{\infty}\tilde{X}_{nm}\int_{r=0}^{R}\tilde{U}_{p;rnm}(r)\tilde{U}_{p;rnl}(r)\mathrm{d}r$$
$$=\frac{1}{\pi(1+\delta_{n0})}\int_{r=0}^{R}\int_{\theta=0}^{2\pi}\left\{K_{rz}\tilde{u}_{i;z}(r,\theta)+K_{r\theta}\tilde{u}_{i;\theta}(r,\theta)+K_{rr}\tilde{u}_{i;r}(r,\theta)\right\}\cos(n\theta)\tilde{U}_{p;rnl}(r)\mathrm{d}\theta\mathrm{d}r \tag{C.9}$$

C.2 Equations of motion - Wall

This section treats the evaluation of equation (2.91) expanded into three separate equations for each unknown degree of freedom:

$$\sum_{n=0}^{\infty}\sum_{m=0}^{\infty}(\omega_{nm}^2-\omega^2)\rho_w h_w\tilde{X}_{nm}(\omega)\tilde{U}_{w;znm}(z)\cos(n\theta)=0 \tag{C.10}$$

$$\sum_{n=0}^{\infty}\sum_{m=0}^{\infty}(\omega_{nm}^2-\omega^2)\rho_w h_w\tilde{X}_{nm}(\omega)\tilde{U}_{w;\theta nm}(z)\sin(n\theta)=0 \tag{C.11}$$

$$\sum_{n=0}^{\infty}\sum_{m=0}^{\infty}(\omega_{nm}^2-\omega^2)\rho_w h_w\tilde{X}_{nm}(\omega)\tilde{U}_{w;rnm}(z)\cos(n\theta)=$$
$$-\mathrm{i}\omega\rho_{fl}\sum_{n=0}^{\infty}\left\{\sum_{a=0}^{\infty}\tilde{P}_{na}(\omega)I_n\left(\frac{\pi(2a-1)R}{2H_l}\right)\cos\left(\frac{\pi(2a-1)z}{2H_l}\right)+\right.$$
$$\sum_{b=0}^{\infty}\tilde{Q}_{nb}(\omega)\left(\cosh(\varepsilon_{nb}z/R)-\frac{\sinh(\varepsilon_{nb}z/R)}{\tanh(\varepsilon_{nb}H_l/R)}\right)J_n(\varepsilon_{nb})+$$
$$\left.\sum_{c=0}^{\infty}\tilde{S}_{nc}(\omega)(\cosh(\varepsilon_{nc}z/R))J_n(\varepsilon_{nc})\right\}\cos(n\theta) \tag{C.12}$$

Making use of the orthogonality of the trigonometric functions reduces equations (C.1) to (C.3) to

$$\sum_{m=0}^{\infty}(\omega_{nm}^2-\omega^2)\rho_w h_w\tilde{X}_{nm}\tilde{U}_{w;znm}(z)=0 \tag{C.13}$$

$$\sum_{m=0}^{\infty}(\omega_{nm}^2-\omega^2)\rho_w h_w\tilde{X}_{nm}\tilde{U}_{w;\theta nm}(z)=0 \tag{C.14}$$

$$\sum_{m=0}^{\infty}(\omega_{nm}^2-\omega^2)\rho_w h_w \tilde{X}_{nm}\tilde{U}_{w;rnm}(z) = -\mathrm{i}\omega\rho_{fl}\left\{\sum_{a=0}^{\infty}\tilde{P}_{na}I_n\left(\frac{\pi(2a-1)R}{2H_l}\right)\cos\left(\frac{\pi(2a-1)z}{2H_l}\right)+ \sum_{b=0}^{\infty}\tilde{Q}_{nb}\left(\cosh(\varepsilon_{nb}z/R)-\frac{\sinh(\varepsilon_{nb}z/R)}{\tanh(\varepsilon_{nb}H_l/R)}\right)J_n(\varepsilon_{nb})+\sum_{c=0}^{\infty}\tilde{S}_{nc}(\cosh(\varepsilon_{nc}z/R))J_n(\varepsilon_{nc})\right\} \tag{C.15}$$

In order to apply the orthogonality conditions of the entire tank and thereby reduce the number of equations to be solved, the wall's equations of motion for each degree of freedom are multiplied by their respective mode shape and integrated over the height. The terms independent of the vertical direction are taken out of the integral.

$$\sum_{m=0}^{\infty}(\omega_{nm}^2-\omega^2)\rho_w h_w \tilde{X}_{nm}\int_{z=0}^{H}\tilde{U}_{w;znm}(z)\tilde{U}_{w;znl}(z)\mathrm{d}z = 0 \tag{C.16}$$

$$\sum_{m=0}^{\infty}(\omega_{nm}^2-\omega^2)\rho_w h_w \tilde{X}_{nm}\int_{z=0}^{H}\tilde{U}_{w;\theta nm}(z)\tilde{U}_{w;\theta nl}(z)\mathrm{d}z = 0 \tag{C.17}$$

$$\sum_{m=0}^{\infty}(\omega_{nm}^2-\omega^2)\rho_w h_w \tilde{X}_{nm}\int_{z=0}^{H}\tilde{U}_{w;rnm}(z)\tilde{U}_{w;rnl}(z)\mathrm{d}z = -\mathrm{i}\omega\rho_{fl}\int_{z=0}^{H_{fl}}\left\{\sum_{a=0}^{\infty}\tilde{P}_{na}I_n\left(\frac{\pi(2a-1)R}{2H_l}\right)\cos\left(\frac{\pi(2a-1)z}{2H_l}\right)+ \sum_{b=0}^{\infty}\tilde{Q}_{nb}\left(\cosh(\varepsilon_{nb}z/R)-\frac{\sinh(\varepsilon_{nb}z/R)}{\tanh(\varepsilon_{nb}H_l/R)}\right)J_n(\varepsilon_{nb})+\sum_{c=0}^{\infty}\tilde{S}_{nc}(\cosh(\varepsilon_{nc}z/R))J_n(\varepsilon_{nc})\right\}\tilde{U}_{w;rnl}(z)\mathrm{d}z \tag{C.18}$$

Note that the second term on the right hand side of equation (C.18) is integrated only up to H_{fl} to take into account that the water pressure is only present up to the water level.

C.3 Kinematic conditions - Wall

After substitution of the modal expression of the tank wall displacement and of the fluid potential (equations (2.23) and (2.32)) into equation (2.93), the equation is multiplied by $\cos(q\theta)$ and integrated from 0 to 2π, resulting in

$$\int_{\theta=0}^{2\pi}\left\{\frac{\partial}{\partial r}\left(\sum_{n=0}^{\infty}\sum_{a=1}^{\infty}P_{na}I_n\left(\frac{\pi(2a-1)r}{2H_l}\right)\cos\left(\frac{\pi(2a-1)z}{2H_l}\right)\cos(n\theta)\right)\Bigg|_{r=R}\right\}\cos(q\theta)\mathrm{d}\theta = \int_{\theta=0}^{2\pi}\mathrm{i}\omega\sum_{n=0}^{\infty}\sum_{m=1}^{\infty}\tilde{X}_{nm}\tilde{U}_{w;rnm}(z)\cos(n\theta)\cos(q\theta)\mathrm{d}\theta \tag{C.19}$$

Evaluation of the differentiation and integration operations, gives

$$\sum_{a=1}^{\infty} P_{na}\left[\frac{n}{R}I_n\left(\frac{\pi(2a-1)R}{2H_l}\right)+\frac{\pi(2a-1)}{2H_{fl}}I_{n+1}\left(\frac{\pi(2a-1)R}{2H_l}\right)\right]\cos\left(\frac{\pi(2a-1)z}{2H_l}\right)= \mathrm{i}\omega\sum_{m=0}^{\infty}\tilde{X}_{nm}\tilde{U}_{w;rnm}(z) \tag{C.20}$$

Note the division by $\pi(1+\delta_{n0})$ to account for the evaluation of the integral. Then, the equation is multiplied by the function in the mode shape that is related to the z-coordinate, and integrated of the height of the tank that is in contact with the fluid, so that

$$\int_{z=0}^{H_{fl}}\sum_{a=1}^{\infty} P_{na}\left[\frac{n}{R}I_n\left(\frac{\pi(2a-1)R}{2H_l}\right)+\frac{\pi(2a-1)}{2H_{fl}}I_{n+1}\left(\frac{\pi(2a-1)R}{2H_l}\right)\right]\cos\left(\frac{\pi(2a-1)z}{2H_l}\right)\cos\left(\frac{\pi(2d-1)z}{2H_l}\right)\mathrm{d}z = \mathrm{i}\omega\int_{z=0}^{H_{fl}}\sum_{m=1}^{\infty}\tilde{X}_{nm}\tilde{U}_{w;rnm}(z)\cos\left(\frac{\pi(2d-1)z}{2H_l}\right)\mathrm{d}z \tag{C.21}$$

Evaluation of the integration operation reduces the equation to

$$P_{na}\left[\frac{n}{R}I_n\left(\frac{\pi(2a-1)R}{2H_l}\right)+\frac{\pi(2a-1)}{2H_{fl}}I_{n+1}\left(\frac{\pi(2a-1)R}{2H_l}\right)\right]\frac{H_l}{2}\delta_{ad} = \mathrm{i}\omega\int_{z=0}^{H_{fl}}\sum_{m=1}^{\infty}\tilde{X}_{nm}\tilde{U}_{w;rnm}(z)\cos\left(\frac{\pi(2a-1)z}{2H_l}\right)\mathrm{d}z \tag{C.22}$$

C.4 Kinematic condtions - Plate

For the second interface condition, concerning the velocity continuity at the plate, the modal expressions of the tank bottom displacement in z-direction and of the fluid potential (equations (2.21) and (2.32)) are substituted into equation (2.94), yielding equation (2.98). Multiplication with $\cos(q\theta)$ and integration from 0 to 2π gives

$$\int_{\theta=0}^{2\pi}\left\{\frac{\partial}{\partial z}\left(\sum_{n=0}^{\infty}\sum_{b=1}^{\infty}\left[Q_{nb}\left(\cosh(\varepsilon_{nb}z/R)-\frac{\sinh(\varepsilon_{nb}z/R)}{\tanh(\varepsilon_{nb}H_l/R)}\right)J_n(\varepsilon_{nb}r/R)\right]\cos(n\theta)\right)\Big|_{z=0}\right\}\cos(q\theta)\mathrm{d}\theta = \int_{\theta=0}^{2\pi}-\mathrm{i}\omega\sum_{n=0}^{\infty}\sum_{m=1}^{\infty}\tilde{X}_{nm}\tilde{U}_{p;znm}(r)\cos(n\theta)\cos(q\theta)\mathrm{d}\theta \tag{C.23}$$

Evaluation of the differentiation and integration operations eliminates the summation over wavenumber n, so that

$$\sum_{b=0}^{\infty}Q_{nb}\frac{\varepsilon_{nb}J_n(\varepsilon_{nb}r/R)}{R\tanh(\varepsilon_{nb}H_l/R)} = -\mathrm{i}\omega\sum_{m=0}^{\infty}\tilde{X}_{nm}\tilde{U}_{p;znm}(r) \tag{C.24}$$

in which the division by $\pi(1+\delta_{n0})$ accounts for the evaluation of the integral. Next, equation (C.24) is multiplied with r and with the function in the fluid vibration modes related to the r-coordinate, and integrated over the radius of the bottom plate:

$$\int_{r=0}^{R}\sum_{b=0}^{\infty}Q_{nb}\frac{\varepsilon_{nb}J_n(\varepsilon_{nb}r/R)}{\tanh(\varepsilon_{nb}H_l/R)}\frac{r}{R}J_n(\varepsilon_{ne}r/R)\mathrm{d}r=-\mathrm{i}\omega\int_{r=0}^{R}\sum_{m=0}^{\infty}\tilde{X}_{nm}\tilde{U}_{p;znm}(r)rJ_n(\varepsilon_{ne}r/R)\mathrm{d}r \tag{C.25}$$

Using the orthogonality property of the Bessel functions

$$\int_{r=0}^{R}\frac{r}{R}J_n\left(\frac{r}{R}\varepsilon_{nb}\right)J_n\left(\frac{r}{R}\varepsilon_{ne}\right)\mathrm{d}r=\frac{\delta_{be}}{2}\left[J_{n+1}(\varepsilon_{nb})\right]^2 \tag{C.26}$$

equation (C.25) can be reduced to

$$Q_{nb}\frac{\varepsilon_{nb}J_n(\varepsilon_{nb}r/R)}{2\tanh(\varepsilon_{nb}H_l/R)}\left[J_{n+1}(\varepsilon_{nb})\right]^2=-\mathrm{i}\omega\int_{r=0}^{R}\sum_{m=0}^{\infty}\tilde{X}_{nm}\tilde{U}_{p;znm}(r)rJ_n(\varepsilon_{ne}r/R)\mathrm{d}r \tag{C.27}$$

which shows that the orthogonality of the Bessel function, has eliminated the summation over wavenumber b.

C.5 Free fluid surface condition

Finally, substitution of the modal expression of the fluid potential (equation (2.32)) into the free surface condition, equation (2.95), yielded equation (2.100). It is then multiplied by $\cos(q\theta)$ and integrated from 0 to 2π to give

$$\begin{aligned}&\int_{\theta=0}^{2\pi}\left\{\frac{\omega^2}{g}\sum_{n=0}^{\infty}\sum_{c=0}^{\infty}S_{nc}\cosh(\varepsilon_{nc}z/R)J_n(\varepsilon_{nc}r/R)\cos(n\theta)\right\}\cos(q\theta)\mathrm{d}\theta=\\&\int_{\theta=0}^{2\pi}\left\{\frac{\partial}{\partial z}\left(\sum_{n=0}^{\infty}\sum_{a=0}^{\infty}P_{na}I_n\left(\frac{\pi(2a-1)r}{2H_l}\right)\cos\left(\frac{\pi(2a-1)z}{2H_l}\right)\cos(n\theta)+\right.\right.\\&\sum_{n=0}^{\infty}\sum_{b=0}^{\infty}\left[Q_{nb}\left(\cosh(\varepsilon_{nb}z/R)-\frac{\sinh(\varepsilon_{nb}z/R)}{\tanh(\varepsilon_{nb}H_l/R)}\right)J_n(\varepsilon_{nb}r/R)\right]\cos(n\theta)+\\&\left.\left.\sum_{n=0}^{\infty}\sum_{c=0}^{\infty}S_{nc}\cosh(\varepsilon_{nc}z/R)J_n(\varepsilon_{nc}r/R)\cos(n\theta)\right)\right|_{z=H_{fl}}\Bigg\}\cos(q\theta)\mathrm{d}\theta\end{aligned} \tag{C.28}$$

The differentiation and integration operations are evaluated to eliminate the summation over wavenumber n:

$$\begin{aligned}&\frac{\omega^2}{g}\sum_{c=0}^{\infty}S_{nc}\cosh(\varepsilon_{nc}H_{fl}/R)J_n(\varepsilon_{nc}r/R)=\sum_{a=0}^{\infty}P_{na}I_n\left(\frac{\pi(2a-1)r}{2H_l}\right)\left(\frac{\cos(\pi a)\pi(2a-1)}{2H_l}\right)+\\&\sum_{b=0}^{\infty}Q_{nb}\frac{\varepsilon_{nb}}{R}\left(\sinh(\varepsilon_{nb}H_{fl}/R)-\frac{\cosh(\varepsilon_{nb}H_{fl}/R)}{\tanh(\varepsilon_{nb}H_{fl}/R)}\right)J_n(\varepsilon_{nb}r/R)+\sum_{c=0}^{\infty}S_{nc}\frac{\varepsilon_{nc}}{R}\sinh(\varepsilon_{nc}H_{fl}/R)J_n(\varepsilon_{nc}r/R)\end{aligned} \tag{C.29}$$

Then, equation (C.29) is multiplied by r/R and by the function of the fluid's modal expression for the free surface in radial direction and integrated over the radius to arrive at

$$\begin{aligned}\int_{r=0}^{R} \frac{\omega^2}{g} \sum_{c=0}^{\infty} S_{nc} \cosh(\varepsilon_{nc} H_{fl}/R) \frac{r}{R} J_n(\varepsilon_{nc} r/R) J_n(\varepsilon_{nf} r/R) \mathrm{d}r = \\ \int_{r=0}^{R} \sum_{a=0}^{\infty} P_{na} I_n \left(\frac{\pi(2a-1)r}{2H_l} \right) \left(\frac{\cos(\pi a)\pi(2a-1)}{2H_l} \right) \frac{r}{R} J_n(\varepsilon_{nf} r/R) \mathrm{d}r + \\ \int_{r=0}^{R} \sum_{b=0}^{\infty} Q_{nb} \frac{\varepsilon_{nb}}{R} \left(\sinh(\varepsilon_{nb} H_{fl}/R) - \frac{\cosh(\varepsilon_{nb} H_{fl}/R)}{\tanh(\varepsilon_{nb} H_{fl}/R)} \right) \frac{r}{R} J_n(\varepsilon_{nb} r/R) J_n(\varepsilon_{nf} r/R) \mathrm{d}r \\ + \int_{r=0}^{R} \sum_{c=0}^{\infty} S_{nc} \frac{\varepsilon_{nc}}{R} \sinh(\varepsilon_{nc} H_{fl}/R) \frac{r}{R} J_n(\varepsilon_{nc} r/R) J_n(\varepsilon_{nf} r/R) \mathrm{d}r\end{aligned} \tag{C.30}$$

Making use again of the orthogonality of the Bessel function (equation (C.26)), equation (C.30) can be rewritten as

$$\begin{aligned}\frac{\omega^2}{2g} S_{nc} \cosh\left(\varepsilon_{nc} \frac{H_{fl}}{R} \right) \left[J_{n+1}(\varepsilon_{nc}) \right]^2 = \int_{r=0}^{R} \sum_{a=0}^{\infty} P_{na} I_n \left(\frac{\pi(2a-1)r}{2H_l} \right) \left(\frac{\cos(\pi a)\pi(2a-1)}{2H_l} \right) r J_n(\varepsilon_{nf} r/R) \mathrm{d}r \\ + Q_{nb} \frac{\varepsilon_{nb}}{2R} \left(\sinh(\varepsilon_{nb} H_{fl}/R) - \frac{\cosh(\varepsilon_{nb} H_{fl}/R)}{\tanh(\varepsilon_{nb} H_{fl}/R)} \right) \left[J_{n+1}(\varepsilon_{nb}) \right]^2 + S_{nc} \frac{\varepsilon_{nc}}{2R} \sinh(\varepsilon_{nc} H_{fl}/R) \left[J_{n+1}(\varepsilon_{nc}) \right]^2\end{aligned} \tag{C.31}$$

It is shown that, due to the orthogonality of the Bessel function of the first kind, the summations over wavenumbers b and c are eliminated from the equations.

References

Abramowitz, M., & Stegun, I. A. (1972). *Handbook of Mathematical Functions with Formulas, Graphs and Mathematical Tables*. New York: Dover Publications, Inc.

Achenbach, J. D. (2003). *Reciprocity in Elastodynamics*. Cambridge: Cambridge University Press.

Aki, K., & Richards, P. G. (2009). *Quantitative Seismology*. Sausalito: University Science Books.

Amabili, M., Païdoussis, M. P., & Lakis, A. A. (1998). Vibrations of Partially Filled Cylindrical Tanks With Ring-Stiffeners and Flexible Bottom. *Journal of Sound and Vibration*, *213*(2), 259–299.

Bauer, H. F., & Siekmann, J. (1971). Dynamic Interaction of a Liquid with the Elastic Structure of a Circular Cylindrical Container. *Ingenieur-Archiv*, *40*(4), 266–280.

Bhakade, S. P., Kumbhar, S. G., Mohite, Y. B., & Kengar, P. V. (2016). A Review on Fluid Structure Interaction Analysis Methodology. *International Journal of Trend in Research and Development*, *3*(3), 617–619.

Bolt, B. A. (1999). *Earthquakes*. New York: W. H. Freeman & Company.

Bolton Seed, H., Wong, R. T., Idriss, I. M., & Tokimatsu, K. (1986). Moduli and Damping Factors for Dynamic Analyses of Cohesionless Soils. *Journal of Geotechnical Engineering*, *112*(11), 1016–1032.

Bungartz, H.-J., Mehl, M., & Schäfer, M. (2010). *Fluid Structure Interaction II - Modelling, Simulation, Optimization*. Heidelberg: Springer-Verlag.

Canny, K. A. (2018). *Seismic Response of Liquid Storage Tank in a Semi Analytical Method* (Unpublished doctoral dissertation). Delft University of Technology.

Chaithra, M., Krishnamoorthy, A., & Naurin Nafisa, P. (2017). Analysis of Soil-Structure Interaction on Response of Tanks Filled with Fluid. *International Journal of Civil Engineering and Technology*, *8*(7), 813–819.

de Hoop, A. T. (2008). *Handbook of Radiation and Scattering of Waves: Acoustic Waves in Fluids, Elastic Waves in Solids, Electromagnetic Waves*. Delft: Academic Press.

Deltares. (2015). *Memo - Aardbevingssignalen Groningen voor berekening* (Tech. Rep.).

Edwards, N. W. (1969). *A Procedure for Dynamic Analysis of Thin Walled Cylindrical Liquid Storage Tanks Subjected to Lateral Ground Motions* (Unpublished doctoral dissertation). University of Michigan.

Elnashai, A. S., & Di Sarno, L. (2015). *Fundamentals of Earthquake Engineering - From Source to Fragility*. Chichester: John Wiley & Sons, Ltd.

EN 14015. (2004). Specification for the design and manufacture of site built, vertical, cylindrical, flat-bottomed, above ground, welded, steel tanks for the storage of liquids at ambient temperature and above.

EN 1998-1. (2005). Design of structures for earthquake resistance - Part 1: General rules, seismic actions and rules for buildings.

EN 1998-4. (2007). Design of structures for earthquake resistance - Part 4: Silos, tanks and pipelines.

Fredlund, D. G., Rahardjo, H., & Fredlund, M. D. (2012). *Unsaturated Soil Mechanics in Engineering Practice*. New York: John Wiley & Sons, Ltd.

Gazetas, G. (1983). Analysis of machine foundation vibrations: State of the art. *International Journal of Soil Dynamics and Earthquake Engineering*, *2*(1), 2–42.

Gibson, R., Mistry, A., Go, J. E. U., & Lubkowski, Z. (2015). Fluid Structure Interaction Vs. Lumped Mass Analogue for Storage Tank Seismic Assessment. In *Earthquake risk*

and engineering towards a resilient world.

Haroun, M. A. (1980). *Dynamic Analyses of Liquid Storage Tanks* (Unpublished doctoral dissertation). California Institute of Technology, Pasadena, California.

Haroun, M. A., & Abdel-Hafiz, E. A. (1986). A Simplified Seismic Analysis of Rigid Base Liquid Storage Tanks under Vertical Excitation with Soil-Structure Interaction. *Soil Dynamics and Earthquake Engineering*, *5*(4), 217–225.

Haroun, M. A., & Housner, G. W. (1981). Seismic Design of Liquid-Storage Tanks. *Journal of Technical Councils*, *107*(1), 191–207.

Horvath, J. S. (2002). *Soil-Structure Interaction Research Project - Basic SSI Concepts and Applications Overview* (Tech. Rep.). New York: Manhattan College.

Housner, G. W. (1963). The Dynamic Behavior of Water Tanks. *Bulletin of the Seismological Society of America*, *53*(2), 381–387.

Housner George W. (1957). Dynamic Pressures on Accelerated Fluid Containers. *Bulletin of the Seismological Society of America*, *47*(1), 15–35.

Jo, J. C. (2008). Fluid-Structure Interactions. *UNESCO Encyclopedia of Life Support Systems*.

Kausel, E. A. M. (1974). *Forced Vibrations of Circular Foundations on Layered Media* (Unpublished doctoral dissertation). Massachusetts Institute of Technology.

Kausel, E. A. M. (2010). Early history of soil-structure interaction. *Soil Dynamics and Earthquake Engineering*, *30*(9), 822–832.

Kramer, S. L. (1996). *Geotechnical Earthquake Engineering*. Upper Saddle River: Prentice Hall.

Larkin, T. (2008). Seismic Response of Liquid Storage Tanks Incorporating Soil Structure Interaction. *Journal of Geotechnical and Geoenvironmental Engineering*, *134*(12), 1804–1814.

Lin, M.-L., Ni, S.-H., Wright, S. G., & Stokoe, K. H. (1988). Characterization of Material Damping in Soil. In *Ninth world conference on earthquake engineering.*

Linton, C. M., & McIver, P. (2001). *Handbook of Mathematical Techniques for Wave/Structure Interactions*. New York: Chapman & Hall.

Lu, Y. (2016). *Seismic Soil-Structure Interaction In Performance-Based Design* (Unpublished doctoral dissertation). University of Nottingham.

Maekawa, A. (2012). Recent Advances in Seismic Response Analysis of Cylindrical Liquid Storage Tanks. In *Earthquake-resistant structures - design, assessment and rehabilitation.* New York: Intech.

Malhotra, P. K. (1997). Seismic Response of Soil-Supported Unanchored Liquid-Storage Tanks. *Journal of Structural Engineering*, *123*(4), 440–450.

Menglin, L., Huaifeng, W., Xi, C., & Yongmei, Z. (2011). Structure-soil-structure interaction: Literature review. *Soil Dynamics and Earthquake Engineering*, *31*(12), 1724–1731.

Molenkamp, T. (2018). *Soil structure interaction for shallow foundations in 2D and 3D - A semi-analytic linear approach* (Unpublished doctoral dissertation). Delft University of Technology.

Nicolici, S., & Bilegan, R. M. (2013). Fluid structure interaction modeling of liquid sloshing phenomena in flexible tanks. *Nuclear Engineering and Design*, *258*, 51–56.

Novotny, O. (1999). *Seismic surface waves - Lecture Notes.* Universidade Federal da Bahia.

Phan, H. N., & Paolacci, F. (2018). Fluid-Structure Interaction Problems: an Application To Anchored and Unanchored Steel Storage Tanks Subjected To Seismic Loadings. In *European conference on earthquake engineering* (pp. 1–10).

Shahverdiani, K., Rhai, A. R., & Khoshnoudian, F. (2008). Fluid-Structure Interaction in Concrete Cylindrical Tanks under Harmonic Excitations. *International Journal of Civil Engineering*, *6*(2), 132–141.

Soedel, W. (2005). *Vibrations of Shells and Plates.* New York: Marcel Dekker, Inc.

Stewart, J. P., Comartin, C., & Moehle, J. P. (2004). Implementation of Soil-Structure Interaction Models in Performance Based Design Procedures. In *13th world conference on earthquake engineering.*

Tang, Y. (1986). *Studies of Dynamic Response of Liquid Storage Tanks* (Unpublished doctoral dissertation). Rice University, Houston.

Tang, Y., & Veletsos, A. (1990). Soil-structure Interaction Effects for Laterally Excited Liquid-Tank System. *Earthquake Engineering & Structural Dynamics*, *19*(4), 473–796.

Tsouvalas, A. (2006). *Semi-Analytical Modeling of the Earthquake Response of an LNG Tank using the Dynamic Sub-Structuring Technique* (Unpublished doctoral dissertation). Delft University of Technology.

Tsouvalas, A. (2015). *Offshore noise generated by pile driving* (Unpublished doctoral dissertation). Delft University of Technology.

Tsouvalas, A. (2017). *Structural Response to Earthquakes Seismic - Analysis of Complex Structures - Lecture Notes.* Delft: Delft University of Technology.

Tsouvalas, A., Canny, K. A., Versluis, M., Peng, Y., & Metrikine, A. V. (2018). Seismic Response of Liquid Storage Tanks Using a Semi-Analytical Dynamic Substructuring Technique. *Unpublished*.

U.S. Department of Transportation. (2006). Soils and Foundations - Reference Manual - Volume 1.

Veletsos, A. (1984). Seismic Response and Design of Liquid Storage Tanks. *Guidelines for the Seismic Design of Oil and Gas Pipeline Systems, ASCE*, 255 – 370.

Vucetic, M., & Dobry, R. (1991). Effect of Soil Plasticity on Cyclic Response. *Journal of Geotechnical Engineering*, *117*(1), 89–107.

Wolf, J. P. (1985). *Dynamic Soil-Structure Interaction.* Englewood Cliffs: Prentice Hall.

Zawawi, M. H., Hassan, N. H., Ramli, M. Z., Zahari, N. M., Radzi, M. R., Saleha, A., ... Kamaruddin, M. A. (2018). Fluid-Structure Interactions Study on Hydraulic Structures: A Review. In *Aip conference proceedings.*